PAIRING SYMMETRY, COMPETING ORDERS, AND QUANTUM CRITICALITY IN IRON BASED SUPERCONDUCTORS VIA LONDON PENETRATION DEPTH MEASUREMENTS

BY

NICHOLAI WILLIAM SALOVICH

DISSERTATION

Submitted in partial fulfillment of the requirements
for the degree of Doctor of Philosophy in Physics
in the Graduate College of the
University of Illinois at Urbana-Champaign, 2013

Urbana, Illinois

Doctoral Committee:

Professor Tai-Chang Chiang, Chair
Professor Russell Gianneta, Director of Research
Professor John Stack
Professor Brian DeMarco

Abstract

The temperature dependence of the magnetic penetration depth (λ) has been measured in single crystals of $BaFe_2As_2$ that have been driven into superconductivity by several different kinds of dopants, specifically potassium, cobalt, and phosphorous.

In $(Ba_{0.6}K_{0.4})Fe_2As_2$ the low temperature behavior of unirradiated samples was consistent with a fully gapped superconducting state with a minimum energy gap $\Delta_{min}/k_BT_C \approx 1$. At very high levels of heavy ion irradiation (a column-column separation of 10 nm) a T^2 power law was observed below $T_C/3$, most likely due to elevated scattering. Neither the location nor the sharpness of the superconducting transition was affected by irradiation. This is evidence for an s_+ pairing state.

In $Ba(Fe_{1-x}Co_x)_2As_2$ an aluminum coating procedure was employed to extract the zero-temperature value of the in-plane penetration depth $\lambda_{ab}(0)$ as a function of the cobalt concentration x, as it was varied through both the underdoped and overdoped regions of the phase diagram. A pronounced increase in $\lambda_{ab}(0)$ was found as the doping value was decreased below the optimal level. This is evidence for direct competition between the itinerant antiferromagnetic phase and superconductivity that region of the phase diagram.

In $BaFe_2(As_{1-x}P_x)_2$ the same aluminum coating procedure was employed to measure $\lambda_{ab}(0)$ as a function of phosphorous doping. A sharp peak in the penetration depth was found at optimal doping, where the superconducting transition temperature reaches a maximum. This may arise from quantum fluctuations associated with a quantum critical point buried beneath the superconducting dome.

Table of Contents

List of Figures

Chapter 1

Superconductivity in Iron Based Compounds:

1.1 Overview:

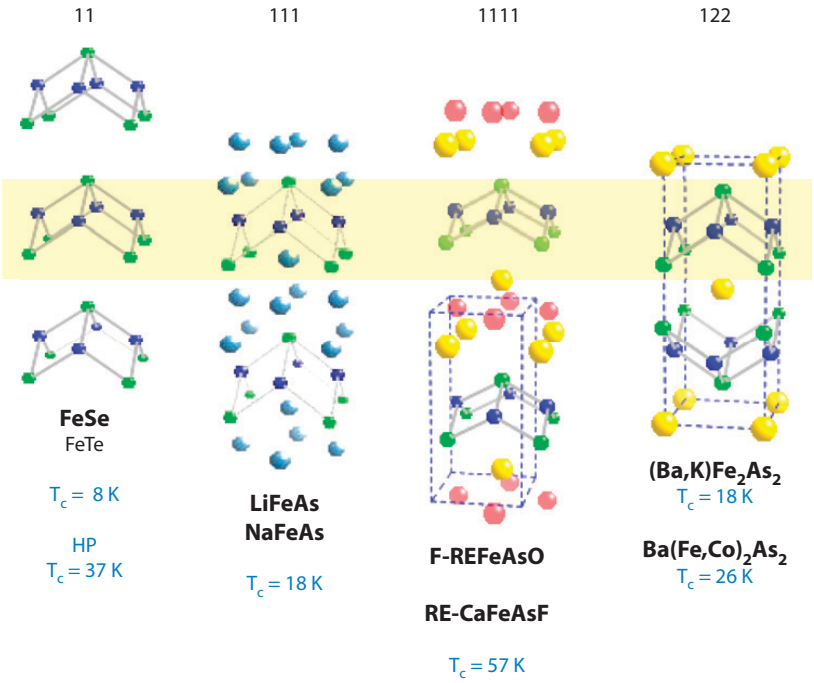

Figure 1.1: Several different structures of Fe-As based superconductors with the Fe-As planes highlighted in yellow. RE stands for rare earth [1].

The discovery of superconductivity in LaFeAsO at 26K [18] catalyzed a global effort that has subsequently charted many more superconducting chemical cousins to those first materials [19]. The common feature amongst all of the highest transition temperature materials is the presence of 2D sheets of FeX_4 tetrahedrally coordinated where X is commonly either arsenic or selenium (figure 1.1. The similarities between the two dimensional properties

of these iron compounds and those of the copper oxide materials has sparked tremendous excitement [4]. This thesis will focus on a particular subset of the iron-based materials commonly known as the "122" family because they are all derived from the parent compound $BaFe_2As_2$.

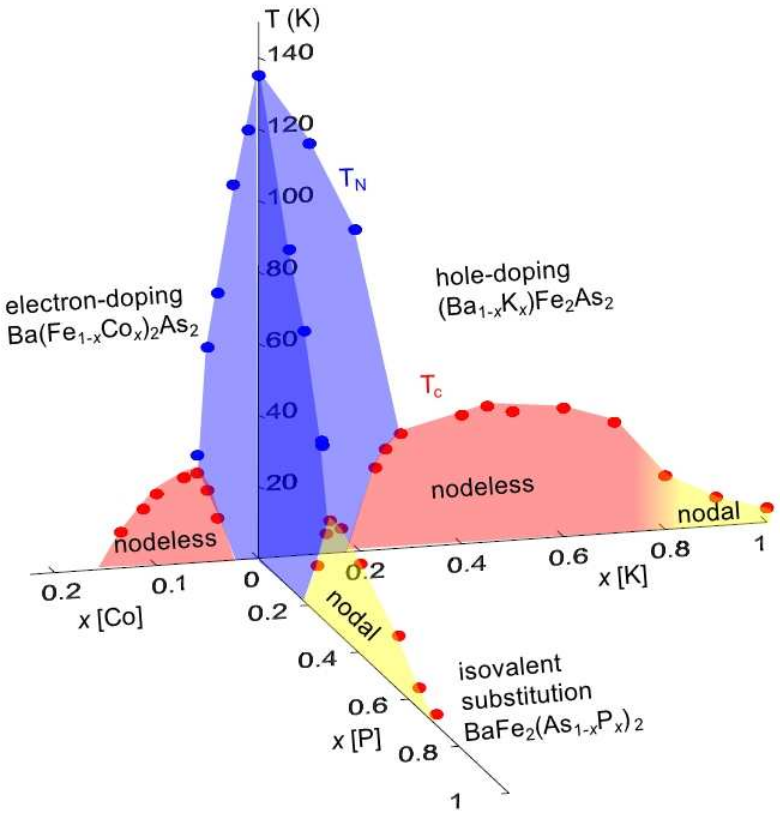

Figure 1.2: Doping diagram for $BaFe_2As_2$. AFM ordering may be suppressed by electron doping (left), hole doping (right) or isovalent substitution (bottom). [2].

Three of the dopants that will induce superconductivity in the parent compound are cobalt, potassium, and phosphorous. Replacing some of the barium with potassium has been shown to add holes to the system and produce T_C;s up to 38K [20]. Substitution of iron with transition metals such a cobalt has been shown to generate T_C's as high as 26K [21]. Finally application of pressure to the parent compound through either mechanical or chemical means has been shown to induce superconductivity with T_C's up to 28K under optimal conditions [22]. This thesis will discuss experiments utilizing each one of these

dopants. Phosphorous doping has been shown to produce some of the cleanest compounds available, as the isovalent nature of the dopant adds no charge disorder to the system [14,23]. As shown in figure 1.2 each of the dopants acts to suppress magnetic ordering in the parent compound which allows superconductivity to emerge [4].

1.2 Generalized Band Structure Properties and Expectations for the Pairing Mechanism:

Comprehensive band structure calculations were completed very quickly after the initial discovery of iron based superconductivity (FBS) [8]. These studies have suggested that quasi-two dimensionality and multi-band physics govern all of the materials so far discovered[Hirschfeld].

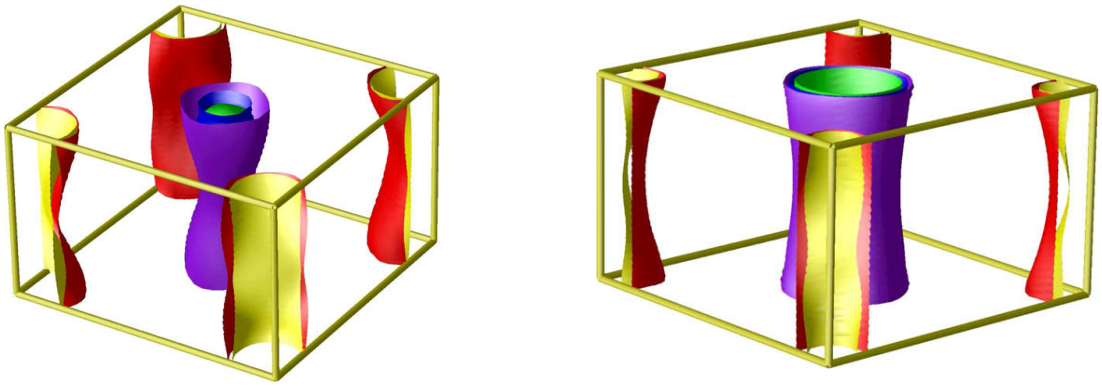

(a) Electron Doping

(b) Hole Doping

Figure 1.3: Fermi surface structures for Iron based superconductors [3]. Low levels of electron doping cause the Fermi suraces to become quasi-2D warped cylinders centered about the (0,0) and (π, π) points. Weak hole doping causes Fermi surfaces to become more isotropic and more two-dimensional.

The prototypical Fermi surface in iron based superconductors consists of five quasi-cylindrical pockets generated from the Fe 3D orbitals with details that highly dependent on the effective doping level (figure 1.3 a and 1.3 b). Three of the pockets are hole pockets located at the center of Brillouin zone. The other two are electron pockets located at the

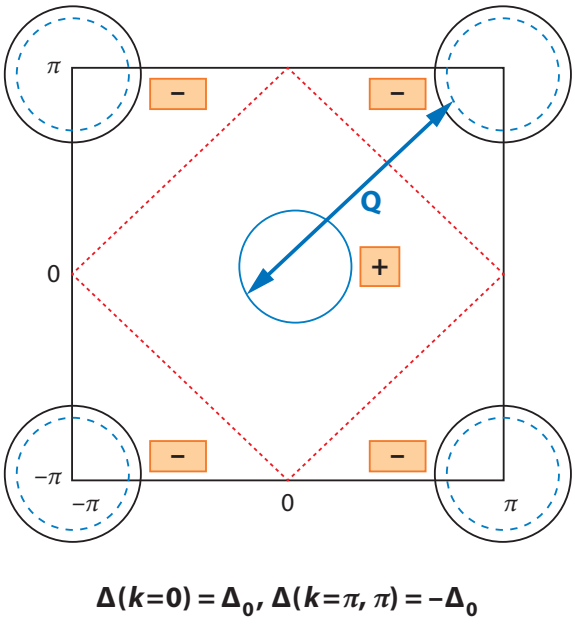

Figure 1.4: Idealized Fermi surfaces for an FBS demonstrating the ease with which a vector Q can match a hole surface (center) with an electron surface (corner) [3].

corners. The degree of circular symmetry of these pockets has been shown to be highly dependent on the nature of the dopants in question [24]. The good match between the cylindrical hole Fermi surfaces and the cylindrical electron Fermi surfaces when either is translated by a vector Q (figure 1.4) inspired many models where electrons were bound into Cooper pairs using the strong spin fluctuations that should develop at that wavevector [4].

It was shown that the naturally repulsive antiferromagnetic interaction between different sheets could be changed into an attractive one capable of producing Cooper pairs if the order parameters on different sheets had opposite signs [25]. The order parameters on different sheets would still maintain their own individual circular symmetry however (figure 1.5 d).This sort of pairing has been called the s_{+-} scenario [26]. This same kind of conversion of a repulsive interaction into an attractive one seems to occur in the cuprates but there generates a d-wave order parameter since the Q vector connects different quadrants of the same Fermi surface sheet [3] (figure 1.5 b). Multi-sheet superconductivity should not be taken as implicit proof that a system must be s_{+-} in nature, given that MgB_2 has a multi-

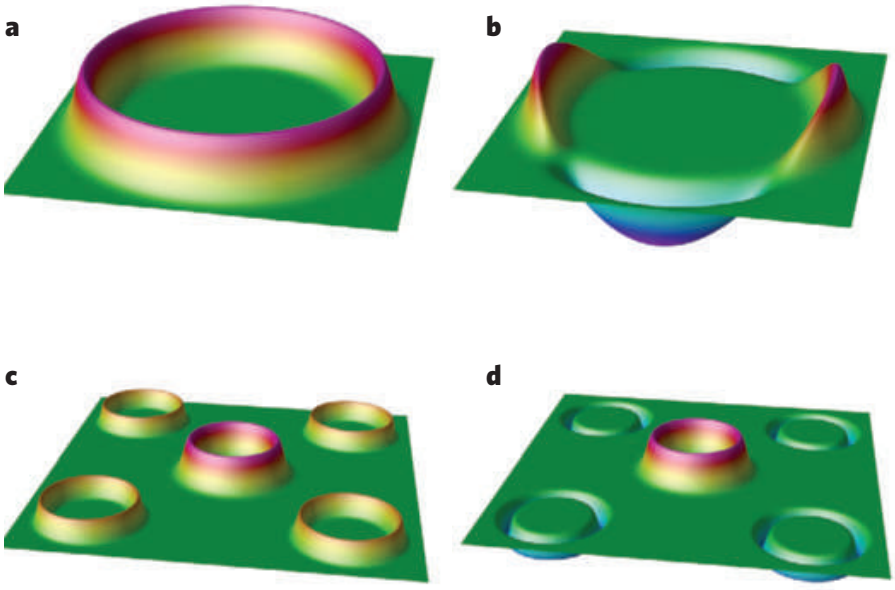

Figure 1.5: Possible forms of the superconducting gap in iron based superconductors: a) conventional s-wave superconductivity b) a d-wave gap, where the sign change is represented by the shift from positive phase (red) to negative phase (blue) c) multi-band s_{++} d) sign changing s_{+-} [4].

sheet fermi surface but has a fully attractive phonon-mediated interaction.

Though the nesting/SDW fluctuation pairing scenario is considered a very good hypothesis at the moment, it should not be considered sacrosanct. Charge fluctuations have also been put forth as a possible cause of conventional multiband s_{++} pairing (figure 1.5 c) with no sign difference between different Fermi surfaces [27, 28]. But given the importance of understanding the pairing interaction to understanding the nature of superconductivity, it is critical that this question be answered.

1.3 Generic Iron-Based Superconductor Phase Diagram and Competing Orders:

The phase diagram for a typical iron-based superconductor is very complex (figure 1.2). The parent materials for most FBS compounds exhibit both antiferromagnetic SDW transitions

and overall structural transitions as they are cooled. The temperatures for both sorts of transitions are suppressed by doping or pressure before reaching some critical level that allows superconductivity to emerge. In some case SDW ordering and supeconductivity remain intimately mixed, while in others they undergo phase separation [29].

Subsequent chapters will describe how measurements of the London penetration depth can utilize the complicated phase diagram of iron based superconductors to answer some of the questions that are at the heart of the study of highly correlated systems.

Chapter 2

Theoretical Background to Superconductivity:

2.1 London Theory:

The usual hallmark of superconductivity is the sudden onset of zero electrical resistance. But it was the discovery of the Meissner effect, that $B = 0$ within a superconductor, that first proved that superconductivity was a true thermodynamic phase completely distinct from the normal state. The Meissner effect also represents the first definitive proof that superconductivity is fact quantum mechanical in nature, because Bohr showed that purely classical charged particles in a magnetic field cannot produce the non-zero static current needed to expel a static magnetic field from the interior of a superconductor [30].

The Meissner effect inspired H. and F. London to develop a theory of the electromagnetic behavior of superconductors. London theory postulates that a superconductor would exhibit loss-less current flow. Charge carriers will accelerate when subjected to a constant driving force according to:

$$m_s \frac{dv_s}{dt} = e_s E \tag{2.1}$$

The total current produced by a density of n_s of charge carriers, then obeys the first London equation:

$$\frac{dJ_s}{dt} = \frac{n_s e_s^2}{m_s} E \tag{2.2}$$

Taking the curl of Ampere's law and substituting our result for dJ_s/dt:

$$\nabla \times B \;\; = \;\; \mu_o J_s$$

$$\begin{aligned}
\nabla \times (\nabla \times B) = -\nabla^2 B &= (\mu_o \nabla \times (J_s)) \\
-\nabla^2(\frac{dB}{dt}) &= \mu_o \nabla \times (\frac{dJ_s}{dt}) \\
-\nabla^2(\frac{dB}{dt}) &= \mu_o \nabla \times (\frac{n_s e_s^2}{m_s} E) \\
-\nabla^2(\frac{dB}{dt}) &= \mu_o \frac{n_s e_s^2}{m_s} (\nabla \times E)
\end{aligned}$$

Further substitution of Faraday's law allow the entire expression to be refactored:

$$\begin{aligned}
-\nabla^2(\frac{dB}{dt}) &= \mu_o \frac{n_s e_s^2}{m_s}(-\frac{dB}{dt}) \\
(\nabla^2 - \mu_o \frac{n_s e_s^2}{m_s})(\frac{dB}{dt}) &= 0 \\
(\nabla^2 - \frac{1}{\lambda_L^2})(\frac{dB}{dt}) &= 0
\end{aligned} \tag{2.3}$$

Equation 2.3 could be answered either by making $\frac{dB}{dt} = 0$, but this would mean that an external field B applied before the sample entered into the superconducting state could never be reduced to 0, in violation of the Meissner effect. Equation 2.3 must instead be rewritten as equation 2.4:

$$\frac{d}{dt}(\nabla^2 B - \frac{1}{\lambda_L^2} B) = 0 \tag{2.4}$$

This results in an equation for field penetration into the bulk of the superconductor with a characteristic length scale set by λ_L:

$$\nabla^2 B - \frac{1}{\lambda_L^2} B = 0 \tag{2.5}$$

The london penetration depth is then:

$$\lambda_L = \sqrt{\frac{m_s}{\mu_o n_s e_s^2}} \tag{2.6}$$

2.2 A Superconducting slab in a Magnetic Field:

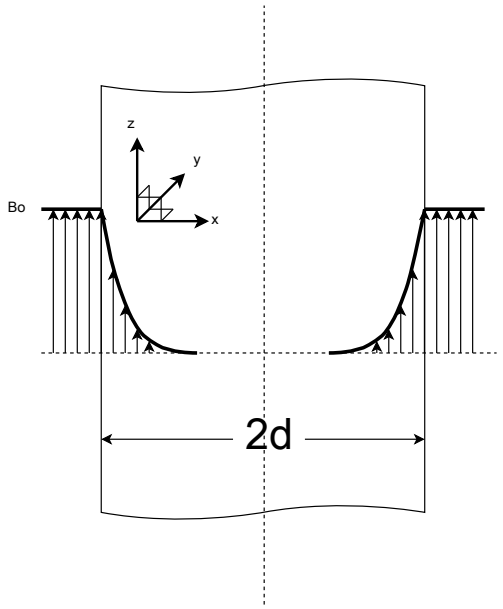

Figure 2.1: An external field B_o penetrates a limited distance into a semi-infinite slab of thickness 2d.

Applying a magnetic field B_o parallel to the surfaces of a slab of superconducting material that is 2d thickness the x direction and infinite in the y and z directions (figure 2.1) yields a simple boundary value problem. The solution of equation 2.5 for the slab shown in figure 2.1 is:

$$B(x) = B_0 \frac{\cosh(\frac{x}{\lambda})}{\cosh(\frac{d}{\lambda})} \tag{2.7}$$

The magnetic susceptibility of the slab is defined as:

$$\chi = \frac{M}{H_0} \tag{2.8}$$

Substituting the solution for field penetration into Shoenberg's formula [31] for its magnetization gives us:

$$M = \frac{1}{2d} \int_{-d}^{d} (\frac{B}{\mu_o} - H_0) dx \tag{2.9}$$

Performing the integral then leaves:

$$\chi = -1 + \frac{\lambda}{d}\tanh(\frac{d}{\lambda}) \tag{2.10}$$

In the limit where $\lambda \Rightarrow 0$, $B_{in.} \Rightarrow 0$ which reproduces the macroscopic Meissner effect.

2.3 Relevant Aspects of B.C.S. Theory

The microscopic model arrived at by Bardeen, Cooper, and Schieffer that allowed a superconducting state to condense out of a conventional fermi liquid requires that solution exist to its self-consistency equation [32]. The BCS gap equation relates the interactions between all possible pairs of fermions at different momentum vectors k and k' through a (potentially anistropic) interaction term $V_{kk\prime}$ and a (potentially anistropic) energy gap $\Delta_{k'}$. Here $\epsilon_{k'}$ are the single electron energies and T is the temperature:

$$\Delta_k = -\frac{1}{2}\sum_{k'} V_{kk\prime}\frac{\Delta_{k'}}{\sqrt{|\epsilon_{k'}|^2 + |\Delta_{k'}|^2}}\tanh\left(\frac{\sqrt{|\epsilon_{k'}|^2 + |\Delta_{k'}|^2}}{2T}\right) \tag{2.11}$$

This nonlinear integral equation defining an entirely unknown function is the keystone to BCS theory. Self-consistent solutions require an attractive interaction ($-V_{kk\prime}$) and set both the transition temperature and the zero temperature gap value. This makes understanding the nature of the interaction and the gap structure in a new materials essential.

A purely repulsive interaction between fermions ($+V_{kk\prime}$), if multiplied by a gap that changes signs somewhere on the Fermi surface, can also generate self-consistent solutions by making both sides of the equation positive [33]. Given the multisheet Fermi surface generic to iron based superconductors, it is natural to suggest that a gap which changes signs between the electron and hole pockets could produce an attractive interaction from nominally repulsive AFM interactions [26]. Such an s_{+-} gap would maintin s-wave symmetry within each respective hole or electron pocket.

2.4 B.C.S. Theory and the London Penetration Depth:

In the clean, semi-classical limit of BCS theory, the temperature dependent penetration depth is related to the gap through:

$$\frac{\lambda^2(0)}{\lambda^2(T)} = \rho_s(T) = 1 - 2\int_{\Delta(\kappa)}^{\infty}\left(-\frac{\partial f}{\partial E}\right)\left(\int \frac{E}{\sqrt{E^2-\Delta^2(\kappa)}}\frac{d\Omega}{4\pi}\right)dE \tag{2.12}$$

The combined integrals average the potentially anisotropic superconducting gap and the potentially anisotropic Fermi surface to track the temperature dependent generation of quasi-particle excitations that progressively destroy superconductivity. The gap only manifests itself through the temperature dependence of the penetration depth. In the zero temperature limit the penetration depth λ_0 is purely a function of band structure of the material, which is consistent with the London result (equation 2.6).

It is worthwhile to calculate the superfluid density and temperature dependent penetration depth for a few different possible gap and Fermi surface configurations. For conventional isotropic swave pairing the unknown gap function becomes a simple k-independent constant. Consequently, the superfluid density becomes:

$$\rho_s = 1 - \sqrt{\frac{2\pi\Delta(0)}{k_B T}}e^{-\frac{\Delta(0)}{k_B T}} \tag{2.13}$$

Substituting $\rho = (\lambda(0)/((0) + \Delta\lambda(T)))^2$ and isolating $\Delta\lambda(T)$, we find that (below $0.25\%T_C$ where the gap can be considered constant) the temperature dependence of the penetration depth is:

$$\Delta\lambda(T) = 1 + \sqrt{\frac{2\pi\Delta(0)}{k_B T}}e^{-\frac{\Delta(0)}{k_B T}} + h.o.t. \tag{2.14}$$

Extracting the properties of unconventional d-wave superconductivity requires a starting model for the anistropic d-wave gap. Under the so-called $d_{x^2-y^2}$ gap framework, the

quasiparticle density of state takes on angular dependence to become:

$$\rho_{d_{x^2-y^2}}(E) = \frac{\rho(\mu)|E|}{4\pi} \int_0^{2\pi} d\phi \int_0^{\pi} d\theta \frac{\sin(\theta)}{\sqrt{E^2 - |\Delta_0|^2 \sin^4(\theta)\cos^2(2\phi)}} \tag{2.15}$$

Along the two lines of longtiude where $\cos(2\phi) = 0$ the order paramter vanishes and the density of states becomes proportional to $E \ln E$ as $E/\Delta_0 \to 0$. Feeding this density of states forward into the general formula for the superfluid density, and assuming a 2D cylindrical Fermi surface (a generic assumption for the copper oxide family of materials), one gets:

$$\rho = 1 - \frac{1}{2\pi T} \int_0^{2\pi} \cos^2(\phi) \int_0^{\infty} \cosh\left(\frac{\sqrt{\epsilon^2 + \Delta^2(T,\phi)}}{2T}\right) d\epsilon d\phi \tag{2.16}$$

In the low temperature limit, to lowest order, this evaluates to a residual linear term, whose discovery in $YBa_2Cu_3O_{6.95}$ [34] was very important evidence for d-wave symmetry:

$$\rho = 1 - 2\frac{\ln 2}{\Delta(0)} T \tag{2.17}$$

In terms of the penetration depth, this results in:

$$\frac{\Delta\lambda(T)}{\lambda(0)} = \frac{2\ln 2}{\alpha\Delta(0)} T \tag{2.18}$$

This is not special to the $d_{x^2-y^2}$ gap assumed earlier, as the linear T dependence arises primarily from the nodal region where $N(E) \propto E$. Except under very special circumstances [35], measurements of the temperature dependent penetration depth do not directly access the phase of the order parameter, but do test for the presence of nodes in the order parameter. Measurements of the zero temperature limit of the penetration depth on the other hand, are in principal a direct function of the Fermi surface.

Chapter 3

Experimental Methods:

3.1 Inductive Measurements of the Magnetic Susceptibility:

One way of the determining λ_L is to measure the magnetic susceptibility of a sample in the superconducting state. Recalling the previous chapter, χ for a superconducting slab is:

$$\chi = -1 + \frac{\lambda}{d}\tanh(\frac{d}{\lambda}) \tag{3.1}$$

This susceptibility could be determined by measuring the change in the inductance of a coil from its original value L_o when the superconducting sample is inserted. The inductance of the coil would then become:

$$L = L_0(1 + \eta\chi) \tag{3.2}$$

where η is a dimensionless filling factor equal to the volume of the sample divided by the volume of the coil. In most circumstances it is preferable to perform measurements in a configuration where the magnetic field is perpendicular to the a-b face of the slab. This requires that the solution for the semi-infinite slab in parallel field described in the previous chapter be generalized to a more complicated geometry. A semi-empirical solution to this problem was shown by Prozorov et al [36] to adequately model the complex spatial behavior

of the screening fields in this configuration. The slab susceptibility then becomes:

$$\chi = \left(\frac{1}{1-N}\right)\left(-1 + \frac{\lambda}{\tilde{R}}\tanh\left(\frac{\tilde{R}}{\lambda}\right)\right) \tag{3.3}$$

Here N is an effective demagnetization factor that depends on the exact sample geometry and $\tilde{R}$ is a characteristic size that incorporates both the sample thickness and width into one combined quantity via the relationship:

$$\tilde{R} \approx \frac{w_{eff}}{2\{1 + \{1 + (\frac{2d}{w_{eff}})^2\}\arctan(\frac{w_{eff}}{2s}) - \frac{2d}{w_{eff}}\}} \tag{3.4}$$

The width w_{eff} is simply the radius for a cylindrical sample. For a rectangular sample it is a function of the sample dimensions in the plane perpendicular to the field:

$$w_{eff} = \frac{ab}{a+b} \tag{3.5}$$

The demagnetization factor can only be calculated analytically for elliptical geometries. For a sphere, the demagnetization factor is $N_{Sph.} = 1/3$.and the effective sample size is simply the radius.

3.2 Resonant Circuit Based Inductance Determination:

Under most circumstances the London Penetration Depth is much smaller than the characteristic size of the sample in which its determination is desired. This means that the overall susceptibility of the sample when it is in the superconducting state is very close to that of a perfect diamagnet, $\chi = -1$. Most techniques for conventional inductance measurement lack the necessary precision to resolve this slight difference and therefore cannot perform London penetration depth measurements. One method by which measurements of the penetration

depth may be made is to make the inductor, into which the sample can be inserted, part of an L-C circuit. The change in the resonance frequency of the combined LC circuit in response to a change in inductance ∂L can then be easily calculated:

$$\begin{aligned} f &= \frac{1}{2\pi\sqrt{LC}} \\ \partial f &= -\left(\frac{1}{2}\right)\left(\frac{1}{2\pi\sqrt{LC}}\right)\left(\frac{\partial L}{L}\right) \\ \frac{\partial f}{f} &= -\left(\frac{1}{2}\right)\left(\frac{\partial L}{L}\right) \\ \frac{\partial f}{f} &= -\left(\frac{1}{2}\right)\left(\frac{L_o \eta \chi}{L_o}\right) \\ \frac{\partial f}{f} &= -\left(\frac{1}{2}\right)\eta\chi \end{aligned}$$

Here we have made the change in inductance upon insertion of the sample ∂L equal to $L_o \eta \chi$. Substituting the semi-analytic expression for the susceptibility established by Prozorov [36] and the respective volumes that define the fill factor η, we are left with:

$$\frac{\partial f}{f} = -\left(\frac{1}{2}\right)\left(\frac{V_{sample}}{V_{coil}}\right)\left(\frac{1}{1-N}\right)\left(-1 + \frac{\lambda}{\tilde{R}}\tanh\left(\frac{\tilde{R}}{\lambda}\right)\right) \tag{3.6}$$

Presented in the form of equation 3.6, the frequency shift of an L-C oscillator upon the insertion of a superconducting sample does not yet allow us to extract the London penetration depth λ_L. This is partially because the pre-factors for the sample dimensions including the effects demagnetization and effective magnetic volume of the coil will not be known to the same precision with which frequency shifts can be resolved. Fortunately the combined effect of those unknown pre-factors can isolated and accounted for by measuring the shift in frequency when the sample is inserted into the coil at base temperature. To a reasonable

degree of accuracy, when $\lambda << \tilde{R}$:

$$\frac{\Delta f_{pullout}}{f_o} \approx -\left(\frac{1}{2}\right)\left(\frac{V_{sample}}{V_{coil}}\right)\left(\frac{1}{1-N}\right) \tag{3.7}$$

This is an approximation, but practice has shown that the real world variance between measured pullout frequency shifts is usually much larger than the error caused by neglecting $\lambda/\tilde{R}$ anyway. With this reduction, equation 3.6 can be restated as:

$$\frac{\partial f}{f_o} = -\frac{\Delta f_{pullout}}{f_o}\left(-1 + \frac{\lambda}{\tilde{R}}\tanh\left(\frac{\tilde{R}}{\lambda}\right)\right) \tag{3.8}$$

If as a next step, the difference is taken between the frequency offset when the sample is at a temperature T_1 and the the frequency offset of the oscillator when the sample is at a temperature T_2, then overall diamagnetic factor "(-1)" can be eliminated as well (for convenience the prefactor will be briefly replaced by α:

$$\frac{\Delta f(T_2) - \Delta f(T_1)}{f_0} = \frac{(f(T_2) - f_0) - (f(T_1) - f_0)}{f_0} = \frac{f(T_2) - f(T_1)}{f_0} \tag{3.9}$$

$$= \alpha\left(\left(1 - \frac{\lambda(T_2)}{\tilde{R}}\tanh\left(\frac{\tilde{R}}{\lambda(T_2)}\right)\right)\right) - \left(1 - \frac{\lambda(T_1)}{\tilde{R}}\tanh\left(\frac{\tilde{R}}{\lambda(T_1)}\right)\right) \tag{3.10}$$

In the limit where $\lambda(T) << \tilde{R}$, the hyperbolic tangent can set equal to unity, which allows for further simplification:

$$\frac{f(T_2) - f(T_1)}{f_0} = -\alpha\left(\frac{\lambda(T_2)}{\tilde{R}} - \frac{\lambda(T_1)}{\tilde{R}}\right) = -\frac{\alpha}{\tilde{R}}\left(\Delta\lambda(T_2 - T_1)\right) \tag{3.11}$$

The frequency shift of the oscillator as the temperature is swept from T_1 to T_2 is then directly proportional to the change in penetration depth between those two temperatures. T_1 is usually set to be the base temperature that can be obtained in a particular measurement,

which can usually be approximated as $T \Rightarrow$0K, leaving:

$$\Delta f(T) = -\frac{\Delta f_{pullout}}{\tilde{R}} \left(\Delta\lambda(T)\right) \tag{3.12}$$

Or:

$$\Delta\lambda(T) = -\frac{\tilde{R}}{\Delta f_{pullout}} \Delta f(T) \tag{3.13}$$

It should be noted that the absolute value of the penetration depth was been lost during this process when the difference in penetration depth between two different temperatures was taken in order to cancel the diamagnetic background term. This is not such a terrible setback when one is simply trying to test for the existence of thermal quasiparticles to differentiate between nodal and non-nodal pairing. But the loss of $\lambda_L(0)$ is catastrophic when one is trying to calculate the superfluid density or establish the superconducting carrier density. A method to recover this information involving a thin film coating will be detailed in a later section of this chapter.

3.3 Estimating the Minimum Required Resolution:

Many novel effects have been predicted to manifest as changes to the penetration depth at the angstrom level [37]. It is a worthwhile excersize to consider how much resolution would be needed to prove or disprove such effects. equation 3.13 can be used to answer this question:

$$\frac{\Delta f(T)}{f_o} = \frac{1}{2V_{coil}} \left(\frac{1}{1-N}\right) \left(\frac{V_{sample}}{\tilde{R}}\right) \Delta\lambda(T) \tag{3.14}$$

$$\frac{\Delta f(T)}{f_o} = \frac{1}{2V_{coil}} \left(A_{ab}\right) \Delta\lambda(T) \tag{3.15}$$

If we target a sensitivity that can resolve changes in the penetration depth of $\Delta\lambda = 1$ Angstrom, and assume that sample is thin platelet with a cross-sectional area of $1mm^2$, that the demagnetization factor N is negligible with the thin slab like sample oriented parallel to

the field, and that the effective coil volume is that of a cylinder $2mm$ in diameter by $10mm$ long:

$$\frac{\Delta f(T)}{f_o} = \frac{1}{\pi \times 10mm^3}(1mm^2)(10^{-7}mm) = 3.2 \times 10^{-9} \tag{3.16}$$

Such resolution thus requires a sensitivity to changes in the frequency of approximately $1ppb$. In practice most samples are substantially smaller than the $1mm^2$ platelet used in that calculation, so resolution of changes in the penetration depth of 1 angstrom or smaller become much more difficult. A smaller coil could in principle boost the resolution, but that would negatively affect both field homogeneity around the sample and increase the risk of thermal contact between the sample and coil.

The required frequency resolution to extract penetration depth changes of 1 Angstrom also sets the minimum empty coil frequency, albeit indirectly. A 1 ppb frequency shift in a radio frequency signal ($f_o \approx 10^7 hz$) is 10 mhz. Shifting the oscillating frequency down to lower frequencies would also make the frequency shift to be much smaller, and therefore much harder to measure. Such low oscillation frequencies would also make component selection much more challenging.

3.4 Tunnel Diode Oscillators for Precision Susceptibility Measurements:

The tunnel diode oscillator [38] is a system that is capable of providing the kind of resolution necessary to discern such small changes in the susceptibility of a sample. Over the last fifteen years, the technique has been used to measure the penetration depth in many unconventional superconductors with extreme sensitivity [39].

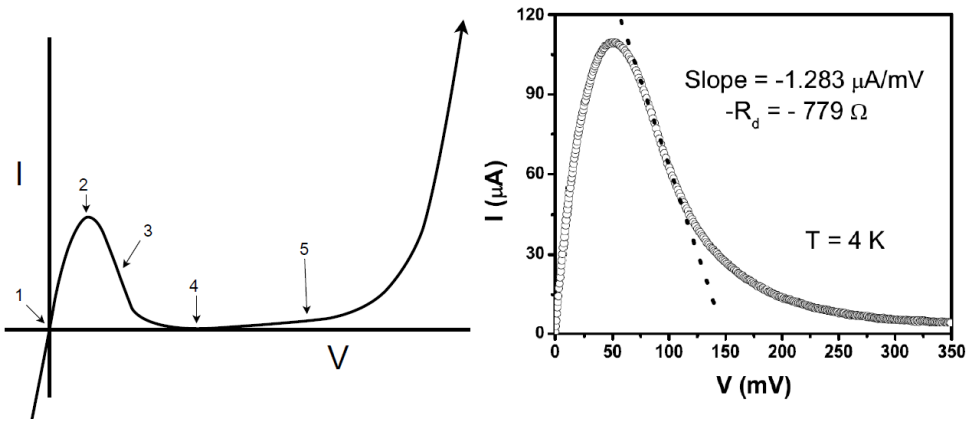

Figure 3.1: Left: A generic I-V curve for a Tunnel Diode. Right: I-V data for the actual tunnel diode used in these measurements.

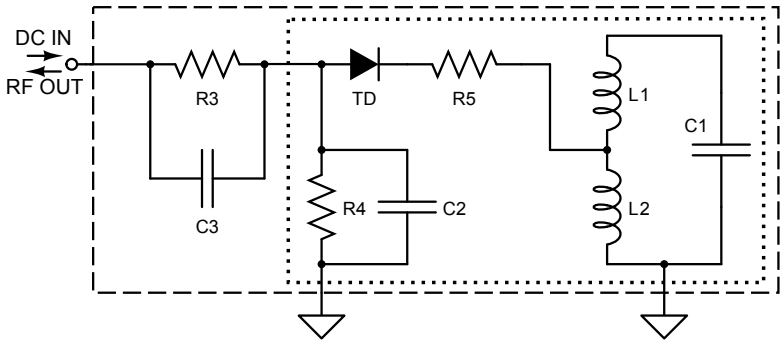

Figure 3.2: A tunnel diode oscillator package. Everything within the long dashes is at a very low temperature within the cryostat. The circuitry within the the short dashes is where the oscillations are principally located, with the exception of the small amount that is diverted through C3 to the RF OUT path for frequency measurement by external instruments.

3.4.1 Tunnel Diode Oscillator Circuitry:

In contrast with a conventional resonator scheme, a tunnel diode oscillator is an active device. DC power must be supplied to the tunnel diode through the resistive voltage divider formed by R3 and R4 to propely bias the tunnel diode into the negative differential resistance region of its I-V curve (3 in figure 3.1, left). The circuit will be unstable and spontaneously oscillate if the $|R_d| \approx |R_{eff}|$. The negative resistance supplied by the tunnel diode must be comparable to the net effective positive resistance connected in parallel with the diode, R_{eff}. This is equivalent to the gain condition for a conventional feedback oscillator.

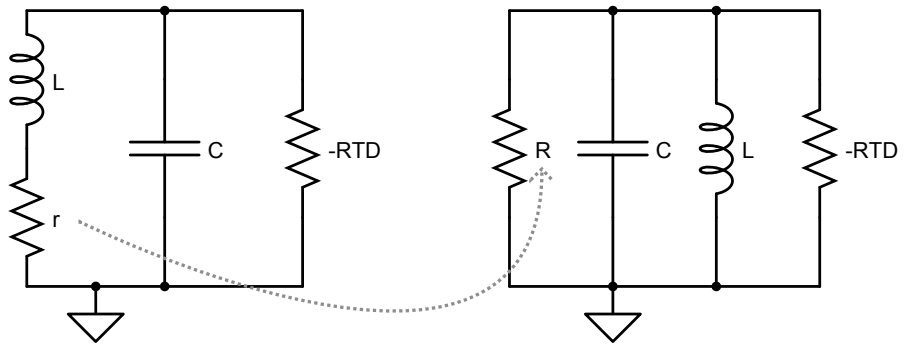

Figure 3.3: At resonance the circuit can be approximated as a tunnel diode supplying negative resistance to an LC circuit with a small resisdual resistance r in series with the inductor. That small series resistance can be transformed into a large parallel resistance R (dashed grey line).

The oscillatory behavior of the circuit can be approximated by the narrowband equivalent circuit shown in figure 3.3. This is because in the frequency range of interest the capacitor C2 in figure 3.2 effectively shorts out the resistor R4, which was only there to set the DC operating point of the tunnel diode. RTD in this model will actually be the remaining differential negative resistance when the tunnel diode negative resistance is add to R5. R5 is needed to suppress higher harmonics of the principal frequency and will be discussed later. The inductance L in narrowband equivalent (figure 3.3) is actually the sum of the inductances L1 (which contains the sample) and L2 in figure 3.2. The second inductor L2 is needed to tune the impedance matching condition between the tunnel diode and the resonant circuit.

If the equivalent series resistance contributed by the inductor L is r, its parallel equivalent R is larger by a factor Q^2. Given that Q for such circuits is typically on the order of 100, this can be a very large equivalent impedance indeed, which pushes the tunnel diode to into its more nonlinear operation regions 2 and 4 (figure 3.1) in order to satisfy the gain condition. Operation in the nonlinear region produces more harmonics and consequently increases the noise of the system.

This can be solved by switching to a tapped inductor configuration (figure 3.4). Under such circumstances the apparent resistance seen looking into the tapped inductors and tunnel

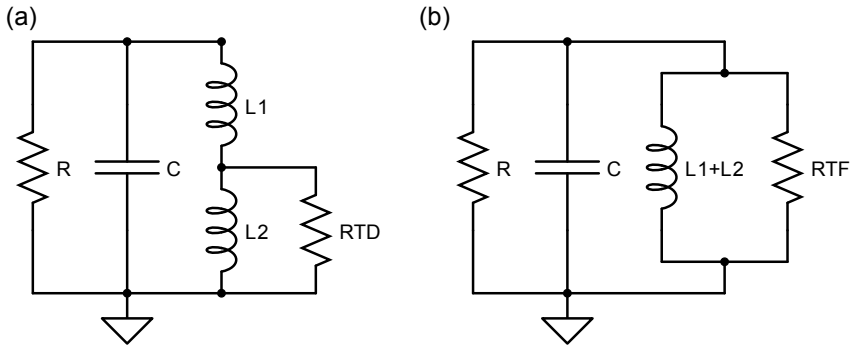

Figure 3.4: The impedance transformation properties of a tapped inductor setup. The effect is to lower the equivalent impedance of the resonant circuit as perceived by the tunnel diode without actually degrading the qualitfy factor of the oscillator. (a) Circuit as built. (b) Circuit after impedance transformation.

diode from the tank circuit parallel resistance R will be:

$$Z_{in} = \frac{i\omega R + i\omega L_2 R - \omega^2 L_1 L_2}{R + i\omega L_2} \tag{3.17}$$

Transforming this to an equivalent admittance:

$$Y_{in} = \frac{i\omega R^2(L_1 + L_2) - \omega^2 L_2^2 R + i\omega^3 L_1 L_2^2}{-\omega^2 R^2(L_1 + L_2)^2 - \omega^4 L_1^2 L_2^2} \tag{3.18}$$

Taking the real part of that admittance and inverting it, one finds that the equivalent resistance of the tapped inductor and tunnel diode combination becomes:

$$R_{eq} = \frac{-R^2(L_1 + L_2)^2 - \omega^2 L_1^2 L_2^2}{-RL_2^2} \tag{3.19}$$

Defining $Q = \frac{R}{\omega_0 L}$, this simplifies to:

$$R = \frac{(L_1 + L_2)^2 + \frac{L_1^2}{Q^2}}{L_2^2} \tag{3.20}$$

Assuming Q to be large this becomes:

$$R_{eq} \approx R\left(\frac{L_1 + L_2}{L_2}\right)^2 = n^2 R \tag{3.21}$$

The result of this transformation then is to boost the effective impedance looking into the tapped inductor and tunnel diode by n^2. This shifts the turn on point of equivalent resistance between the tank circuit and the tunnel diode back toward the middle of the tunnel diodes negative differential resistance range (point 3 in figure 3.1).

One can also calculate the imaginary part of the impedance of the tapped inductor tunnel diode network by following the same procedure. Again assuming that Q is large, one finds that equivalent inductance of the network can be described by :

$$L_{eq} = \frac{(L_1 + L_2)^2 - \frac{L_1^2}{Q_2^2}}{L_1 + L_2 + \frac{L_1}{Q_2^2}} \approx \frac{(L_1 + L_2)^2}{L_1 + L_2} \tag{3.22}$$

This is just the usual series sum of the two inductances. The resonant frequency of the whole system then becomes the usual function of the capacitance and total inductance :

$$f_0 = \frac{1}{2\pi\sqrt{(L_1 + L_2)C}} \tag{3.23}$$

Unfortunately the tapping coil has the side effect of increasing the total inductance while not being affected by the sample. This reduces the fill factor and consequently the signal to noise. Tuning the tapping fraction is also semi-empirical art. The usual procedure is to

wind a tapping coil that has too many turns, test the harmonic content of the oscillator, unwind a turn, and test again, until a satisfactory level of harmonic suppression is reached because matching is occuring at a more linear region of the tunnel diode I-V.

Harmonics may be further suppressed by adding a positive resistorR_p in series with the tunnel diode. Such a resistor of course has the effect of reducing the available power that the diode can supply to the resonator, but that is not typically an issue for measurements made with an intentionally low ac field. Recalling the earlier discussion it is apparent that higher harmonics cannot appear across the LC circuit. So if they are generated, they must appear as voltages only across the tunnel diode, which also means that they are part of the voltage sent to the room temperature measurement circuitry. But the addition of an extra resistor in series with the tunnel diode will cause the harmonic voltage to be expressed predominately across the resistor, and not across the full section of the circuit with a path to the measurement instrumentation.

3.4.2 Tunnel Diode Oscillator Component Selection:

In his original paper [38], van de Grift provided algorithms for selecting the components for a precision tunnel diode oscillator. He found that the harmonic suppression resistor $R5$ should be $\approx |R_d|/4$. As an optimal value for R4, he found that it should be equal to $3/4_d$. The other resistor in the voltage divider, R3, can be much larger than $R2$, which helps to isolate the oscillator from interference sources at room temperature. The impedance of the capacitor $C2$ at the oscillation frequency of the system needs to be much lower than the DC biasing resistor it is in parallel with, in order to form an AC short. A large $C2$ also has the beneficial effect of further reducing the degree to which room temperature inteference can couple into the oscillator circuit. Finally setting $C3 = C2|R_d/100,000R_L$ allows a few microvolts of signal to leak out of the oscillator and be measured at room temperature.

There is substantially more freedom for the actual oscillator portion of the circuit. Typical sample coils are 2 millimeters in diameter and consist of 40-50 turns of 44 gauge copper

wire, wound with a spacing between turns equal to the diameter of wire. This reduces the stray capacitance of the coil substantially. The ideal tapping fraction was found to be roughly 40% of the inductance of the primary coil, which meant the coil wound up having approximately 20 turns on a silica mandrel. The capacitor C1 was chosen to be $\approx 100pF$ to set the oscillation frequency to approximately 14 Mhz.

3.4.3 Frequency Measurement and Oscillator Performance:

The raw signal emerging from the tunnel diode oscillator is a low-amplitude AC signal in the range of 13-14 megahertz with a non-trivial amount of environmental noise superimposed on it. This is not convenient to directly digitize and store. It is much better to first amplify the oscillator signal then hetrodyne it against a stable reference oscillator, such as a Marconi frequency synthesizer, set to be just a few kilohertz higher than the tunnel diode signal. The difference frequency will then be an audio range signal that can be amplified and bandpass filtered again with tremenduous ease before finally being counted on an HP Universal counter and digitally stored via custom Labview code. Usually the narrowest possible bandpass settings available on an audio frequency preamp should be used, although for particularly large samples the pass-band may have to be enlarged simply to fit the full range of beat frequency variation.

Typical TDO data acquired in just such a fashion is plotted in figure 3.5. The r.m.s. variation the data over a few seconds of averaging is typically less than 20 mhz out of a principal frequency of approximately 13.7Mhz. This corresponds to a $\partial f/f_o$ resolution of 1ppb in a second or two of frequency counting. Inset into that figure are schematics that illustrate the difference between the TDO signal and the local oscillator reference signal, $F_{L.O.}$ both during a temperature sweep and during a pullout test at base temperature. The local oscillator frequency is traditionally set to a frequency higher than the actual tunnel diode frequency, although this is not strictly necessary. As the sample temperature cools down through T_C the sample becomes more diamagnetic and excludes flux from its volume,

reducing the inductance of the sample coil and raising the frequency.

Also illustrated in the pullout schematic is the correction for the sapphire sample holder that must be applied to the average level of the oscillator frequency to correctly estime $F_{Pullout}$. Because the sapphire is paramagnetic, it lowers the oscillation frequency. This lowering must be removed to extract the actual difference in oscillation frequency between when the sample is in the coil and when it is out of the coil.

3.5 Low T_C Film Coating Process for $\lambda_L(0)$ Determination:

A critical weakness of the conventional tunnel diode oscillator technique is its inability to determine the low temperature limit of the penetration depth, $\lambda_L(0)$. This information was lost when the subtraction in equation 3.10 was performed, although in principle other uncertainties in effective sample dimension and pullout frequency shift would be have swamped the effect of $\lambda_L(0)$ on the oscillator frequency output at this point anyway.

One way to recover this data is to coat the sample in a thin film of a low T_C superconductor such as aluminum. Temperature sweeps from the base temperature of the cryostat to temperatures above T_{C-Al} will produce a shift in the london penetration depth like that pictured in figure 3.6. The size of the shift $\Delta\lambda_{meas}$ will be related to the $\lambda_{Al}(0)$, $\lambda_{Sample}(0)$, and film thickness τ. This can be explained by noting that the oscillator frequency shift is directly proportional to the change in the penetration depth. As is protrayed in figure 3.7, the change in penetration depth from when the aluminum provides most of the screening to when the aluminum is normal is:

$$\Delta\lambda_{meas} = \lambda_{T>TC-Al} - \lambda_{T<TC-AL} = \lambda_{Sample}(0) + \tau - \lambda_{Al}(0) \tag{3.24}$$

Solving equation 3.24 for $\lambda_{Sample}(0)$ we find that:

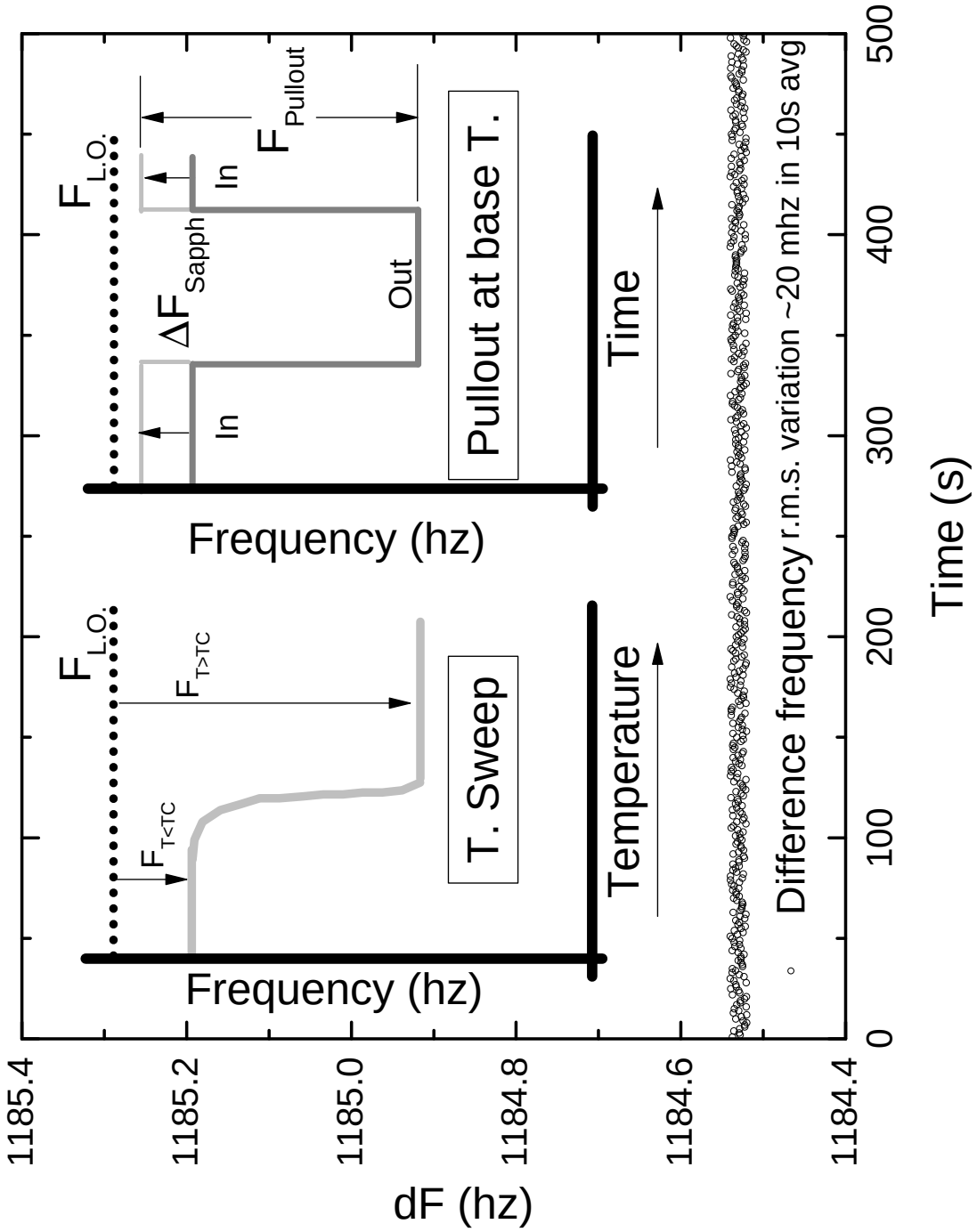

Figure 3.5: Typical oscillator data measured by hetrodyning the TDO signal against a stable reference signal. The difference frequency versus time is plotted in the main figure, which demonstrates its stability and very low short term noise (20 mhz out of 13 Mhz). Inset left: Schematic of how absolute oscillator frequency changes with temperature. Inset right: Schematic showing how the oscillator signal changes when the sample (and sapphire holder) is withdrawn from the sample coil at base temperature.

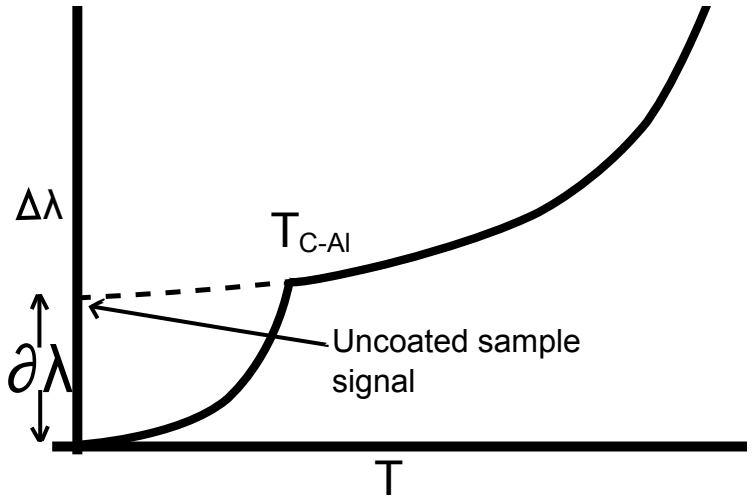

Figure 3.6: The change in penetration vs temperature for an aluminum coated sample. The extra shift in penetration depth $\Delta\lambda$ is a function of the film thickness and the zero temperature penetration depths in both the sample and the aluminum itself.

$$\lambda_{Sample}(0) = \Delta\lambda_{meas} - \tau + \lambda_{Al}(0) \tag{3.25}$$

The aluminum coating provides a sort of in-situ length scale that allows the absolute penetration depth of the sample to be recovered from the $\Delta\lambda(T)$ data the system is very well suited to measuring. The reasoning that inspired equation 3.25 is not quite correct, one must actually solve the full boundary value problem for a superconducting film with its penetration depth on top of a semi-infinite superconducting half space with a different penetration depth. The solution to that boundary value problem is:

$$\lambda_{sample}(0) \approx \frac{1}{2}\left(F + \sqrt{F^2 + 4(\lambda_{Al}(0))^2 + \frac{4\lambda_{Al}(0)F}{tanh(\tau/\lambda_{Al}(0)}}\right) \tag{3.26}$$

where:

$$F = \Delta\lambda_{meas} - \tau \tag{3.27}$$

For typical measurement circumstances $\tau \approx 100nm$, $\lambda_{AL}(0) \approx 50nm$, and $\lambda_{sample}(0) \approx 200nm$. The solution to the boundary value problem under those conditions is neglibly different from the crude model solved in equation 3.25

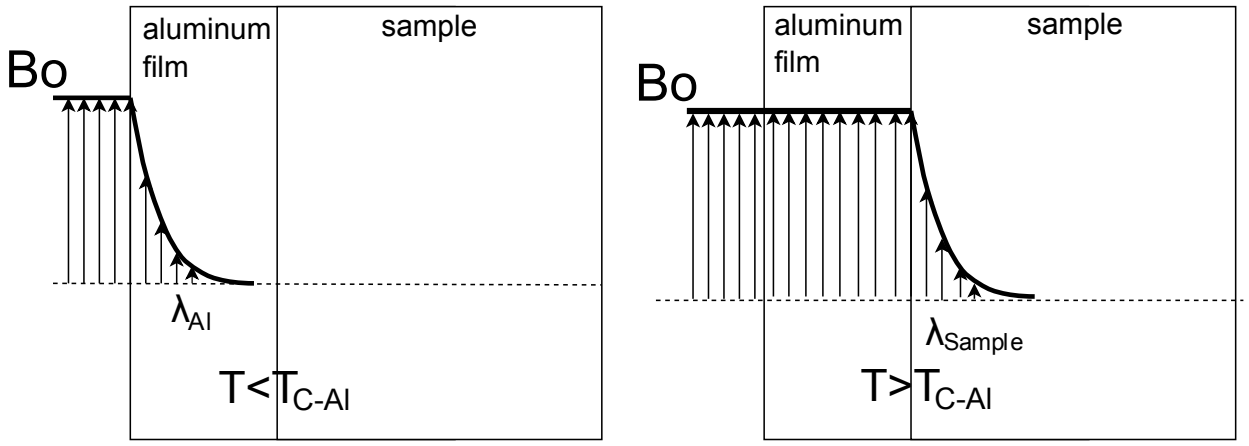

Figure 3.7: At base temperature, the aluminum film provides most of the field screening, provided that the thickness is greater than the $\lambda_{Al}(0)$. Above the transition temperature of the aluminum it is essentially invisible and the AC magnetic field from oscillator penetrates through it completely.

3.6 Cryogenics:

All penetration depth measurements at Urbana were performed in a Helium-3 cryostat capable of reaching base temperature of 400mK. It is a two stage refrigeration system pictured in figure 3.8. In the first stage liquid helium from the bath surrounding the outer vacuum can is drawn into the 1K through a small straw (light gray in figure 3.8). A fine capillary impedance (not pictured) reduces the flow rate of the liquid helium into the bath to the proper level. The liquid helium that collects in the 1K is forcibly evaporated by a vacuum pump connected to the chamber through a large diameter pumping line. The evaporation of the liquid helium drops the temperature of the 1K pot down to about 1.5K, which is sufficiently cold to liquiefy the helium-3 contained within a second loop (lower chamber in figure 3.8).

The liquified helium-3 (dark gray) is then forcibly evaporated by a second pumping system connected to the helium-3 pot by a large diameter pumping line. All of the gas lines for the helium-3 system are isolated from the first stage 1K pot, though returning helium-3 gas collected from the output of the vacuum pump is cycled through a portion of the lines that are in very good thermal contact with the 1K stage to re-liquify it. The

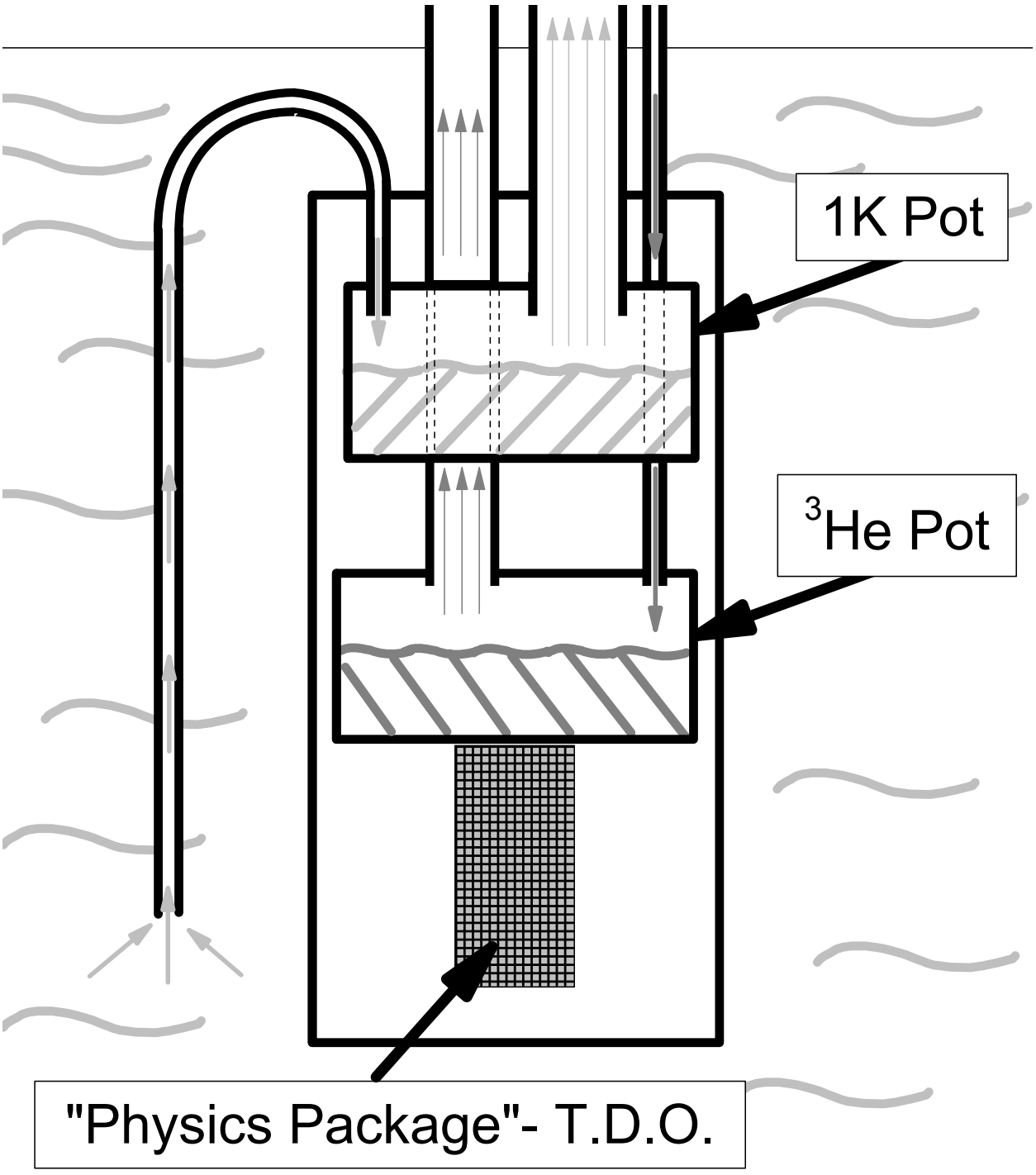

Figure 3.8: Recirculating Helium-3 Cryostat.

evaporation of helium-3 by the action of a mechanical pump is sufficient to cool the stage down to approximately 600 mK. If a booster pump is used in series ahead of the mechanical pump the extra pumping speed it adds is sufficient to cause the helium-3 pot temperature to drop to approximately 400 mK.

All of the tunnel diode oscillator circuitry is contained within a small unit mounted onto the helium-3 pot, including the sample stage and sapphire rod onto which the sample will be mounted (the physics package in figure 3.8). The actual oscillator unit and coil are thermally isolated from the helium-3 pot by a length of Vespel tubing and thermally coupled to the 1K instead via a length of OFHC copper rod. This allows the temperature of the oscillator circuitry to be actively stabilized which has been shown to drammatically decrease drift in the oscillator frequency.

Chapter 4

Effect of Heavy-Ion Irradiation on $Ba_{0.6}K_{0.4}Fe_2As_2$

4.1 Introduction:

As discussed previously, the s_{+-} phase, a multi-gap order parameter with a sign difference between different energy gaps on different Fermi sheets is the leading candidate for describing the pairing state in iron based superconductors [25, 40]. But the question of the pairing symmetry cannot trusted to theory alone, as later works have shown that that gap structures appear to vary substantially with doping and pressure, even within particular familes of materials [41]. Although the existence of multiple gaps has been definitivity established [42],it has proven very difficult to find experimental evidence for an s_{+-} order parameter [43]. Partially, this is because the temperature dependent properties associated with such a gap structure would be the same for both s_{+-} and s_{++} order parameters in the clean limit. Direct measurements of the phase difference between different gaps have had minimal success because of issues with severe surface degradation during Josephson junction fabrication [44].

Fortunately, the prediction by several different groups of impurity concentration dependent changes to thermal properties that would be unique to s_{+-} ordering has opened up another avenue of exploration [45, 46]. In particular, increasing the impurity concentration is expected to drive the London penetration depth from exponential temperature activation just like in a conventional BCS material to T^2 behavior. This stands in stark contrast with nodal d-wave systems where the effective power-law governing the temperature dependence was shown to evolve from linear T dependence to T^2 with increasing impurity concentration [47].

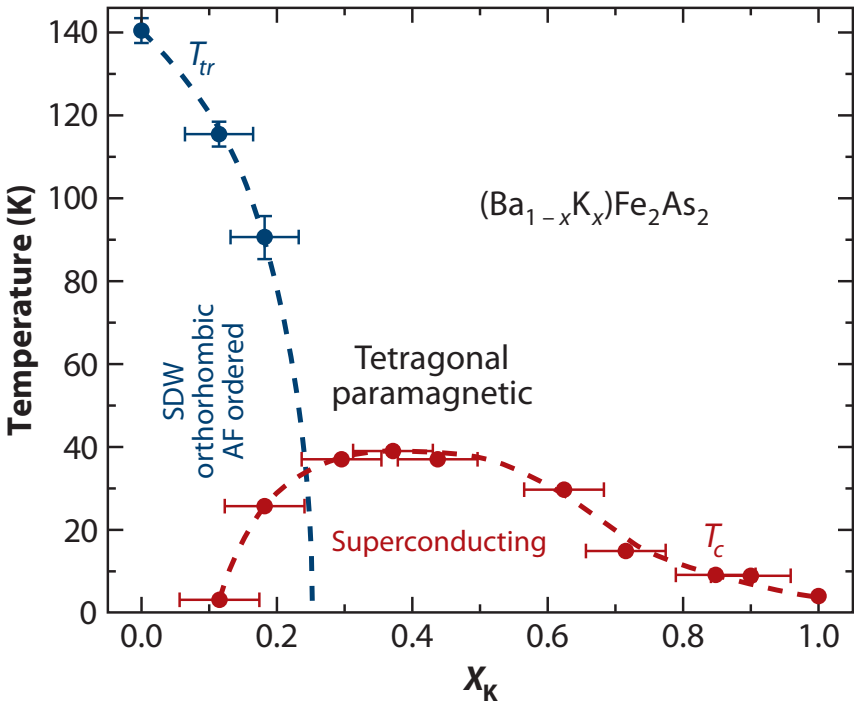

Figure 4.1: Typical phase diagram for $Ba_{0.6}K_{0.4}Fe_2As_2$ [1].. Error bars represent uncertainties related to inhomogenieties in the local doping level that were especially prevelent in early samples. It is not yet established if superconductivity actually occurs as a single phase within the range of $0.5 < x < 1.0$. There is some evidence that the order parameter becomes nodal for $x = 1.0$ and over a small range $0.2 < x < 0.3$ [5].

Some of those predictions also hold that impurities will have strong effects on the transition temperature but the issue is somewhat contentious [6,48,49]. In early models interband scattering between gaps with different signs was expected to rapidly suppress T_C just like magnetic impurities do in a conventional material [48]. Later work has shown that the picture might be much more complicated because scattering can occur through both interband and intraband channels [6, 49]. The net effect of impurities on T_C will then be a complex function of the relative rates of those different forms of scattering. Depending on the final result of that function the transition temperature can be reduced or remain entirely unaffected. Furthermore, other works have shown that competing phases which can simultaneously coexist with superconductivity can be preferentially suppressed by impurities leading to the indirect strengthening of superconducting order and the Fconsequent enhance-

ment of T_C, simultaneously with any of the previously discussed changes to the transition temperature [50].

What complicates any attempts to test for relative sign differences through the addition of chemical impurities to the system is the possibility that such added impurities will alter the carrier concentration. Early measurements may have inadvertently tested the sensitivity of the powerlaw to impurities left over from less refined crystal growth techniques but their measurements could not distinguish either disorder and unintentional carrier changes as the true cause of the changes in T_C that they found. Given that recent thermal conductivity studies have shown that $Ba_{0.6}K_{0.4}Fe_2As_2$ will change from a nodeless state ($\Delta\lambda \propto \sqrt{\Delta/T}\exp^{-\Delta/T}$) to a nodal order parameter($\Delta\lambda \propto T$) as the potassium doping is increased, this is of particular concern [51–53].

Another option is to use heavy ion irradiation to produce amorphous columnar tracks throughout the sample. Such tracks will neither change the carrier concentration nor introduce additional magnetic scattering centers. The concentration of such defects can be easily and continuously tuned by controlling the dosage during the irradiation process. Their columnar geometry is also particularly relevant to studies aimed at enhancing the critical current capacity of technologically relevant superconductors [7, 54].

Properly testing the effect of the introduction of columnar defects on the material properties requires that comparisons be made between different doses applied to the same crystal. Otherwise the problem of unknown intrinsic differences between different crystals that plagued earlier work will remain unaccounted for. This is because two crystals, even if grown simultaneously, will not necessarily have the same properties. This can be avoided by either measuring the same crystal before and after irradiation, or by cleaving the starting crystal into sections, so that some parts may altered while one part is left as an unaltered reference.

The influence of impurity scattering on the power-law dependence of the penetration depth has been previously tested in the electron doped $Ba(Fe_{1-x}Co_x)_2As_2$ using this method [55]. They found that the samples followed a powerlaw of approximately $T^{2.5}$ before irra-

diation. After irradiation this power-law dropped to T^2. The transition temperature also dropped systematically as radiation dosages were increased for both materials. While these results are roughly consistent with an s_{+-} picture, they do not qualify as a smoking gun because the behavior of their unaltered before irradiation ($\Delta\lambda(T) \propto T^{2.5}$) did not confrom to the BCS-like form $\Delta\lambda \propto \sqrt{\Delta/T}\exp^{-\Delta/T}$. This is thought to be because the electron dopant atoms needed to induce superconductivity add disorder into the crucial Fe-As planes and are thus thought to leave the materials inherently very dirty even before radiation adds additional disorder [55]. Hole doping is preferable in that it adds disorder only to charge reservoir layers in between the planes where it seems to be well isolated from the superconductivity [56]. Naturally then the next step is to test the effect of irradiation on high quality optimally doped K-122 crystals [57]. This became possible only recently because sufficiently clean and homogenously doped crystals were very difficult to grow, despite the fact that potassium doped materials were the first family member of the 122's to be discovered [55].

4.2 Experimental Work:

Measurements were performed on five samples cleaved from two original crystals. One fragment from each starting crystal was left unaltered while the others were irradiated by W. Kwok and collaborators at Argonne National Lab with different doses of 1.4 GeV ^{208}Pb atoms at the Argonne Tandem Linear Accelerator. Dispersion of the beam by a gold foil by Rutherford scattering ensured uniform beam intensity of tracks generated parallel to the c axis of the irradiated sample. Keeping the beam current below 500 pA avoided sample heating. The average stopping distance of the heavy ions within the samples was 60-70 μm, which was much larger than the approximately 15 μm c axis thickness of the samples. The dosage is expressed as a fluence and a matching field where $B_\phi = \phi_0/r^2$ with r being the mean column to column separation and ϕ_0 being the flux quantum.

From the crystal measured at Ames ($T_C = 39$K) that was cleaved into three sections, one

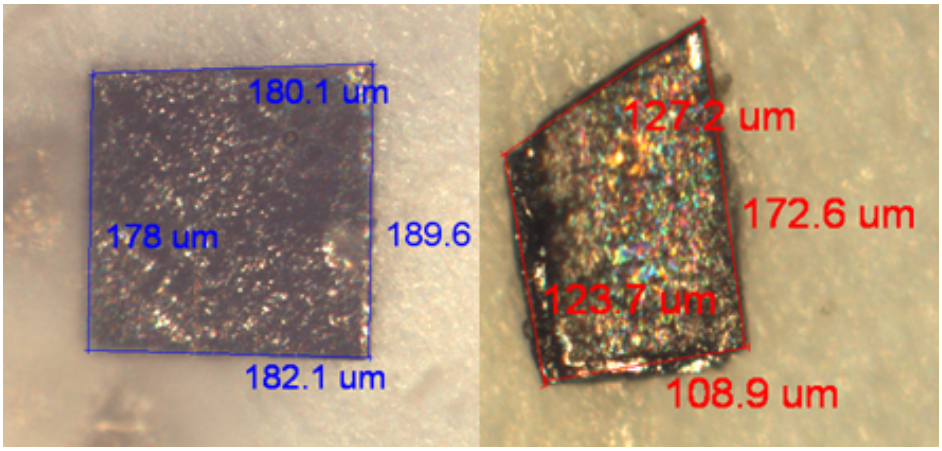

Figure 4.2: Top down views of the crystals cleaved from one starting crystal. The crystal on the left was not irradiated. The crystal on the right was dosed to a 21T matching field.

was left unaltered while the other two fragments were irradiated to two different irradiation levels, $B_\phi = 2$T (fluence $= 9.6x10^{10} ions/cm^2 s$) and $B_\phi = 4$T (fluence $= 1.9x10^{11} ions/cm^2 s$). From the crystal measured at UIUC ($T_C = 36.8$K) that was split into two fragments (figure 4.2), one fragment was left unaltered while the other was irradiated to a relatively high level of 21T (fluence $= 10^{12} ions/cm^2 s$). The average spacing between the radiation produced columns was 32 nm for the 2T sample, 22 nm for the 4T sample and 10 nm for the 21T sample, respectively. It should be noted that the second group of two crystals was very small and represents a substantial signal to noise challenge for volumetric measurements.

The temperature dependence of the penetration depth was measured using two different tunnel diode oscillators functioning in the manner previously discussed in earlier sections of this thesis. The raws data from the measurements of the second crystal is shown in figure 4.3. The substantial upturn in the low temperature regime is residual paramagnetism from the sapphire holder on which the sample is mounted. Prior measurements of the sapphire background were not of sufficient accuracy to allow for reliable subtraction from the data in figure 4.3, so more precise measurements were made. Those measurements were repeated over the course of several days as the magnetic background and thermal history of the system was varied in order to establish the long term reproducibility of the data. The static

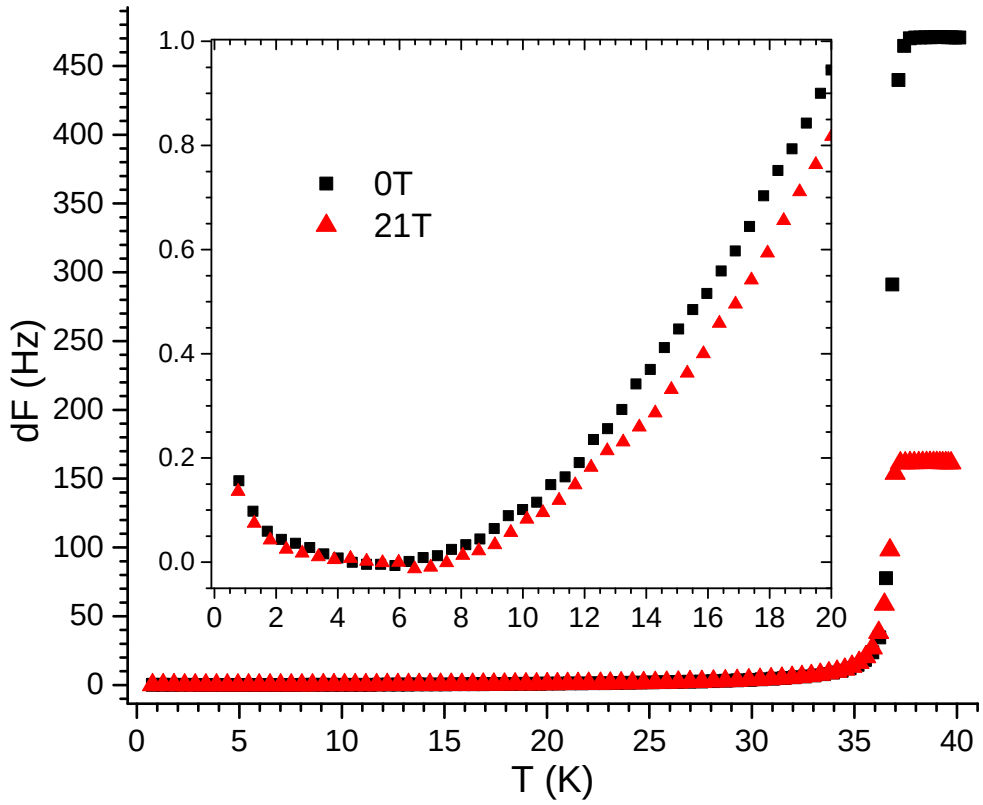

Figure 4.3: Raw data for both the unirradiated and irradiated crystals. The overall shifts are comparable to what is expected from the sample size and estimated demagnetization. Inset: Data below $0.1T_C$ is dominated by a paramagnetic upturn from the sapphire sample mount.

frequency shift caused by the insertion of the sapphire also had to be accounted for during calculation of the effective sample pullout frequency shift. This process is illustrated in figure 4.4.

Several typical sweeps measuring the response of just the sapphire sample holder and their average are plotted in figure 4.6. Subtraction of this average background term from the raw data followed by conversion to $\delta\lambda(T)$ using the methods specified in Chapter 2 results in the data set plotted in figure 4.6. The error bars in figure 4.6 represent the estimated effect of the uncertainty in the subtracted sapphire background visible in figure 4.5 ($\approx$ 30

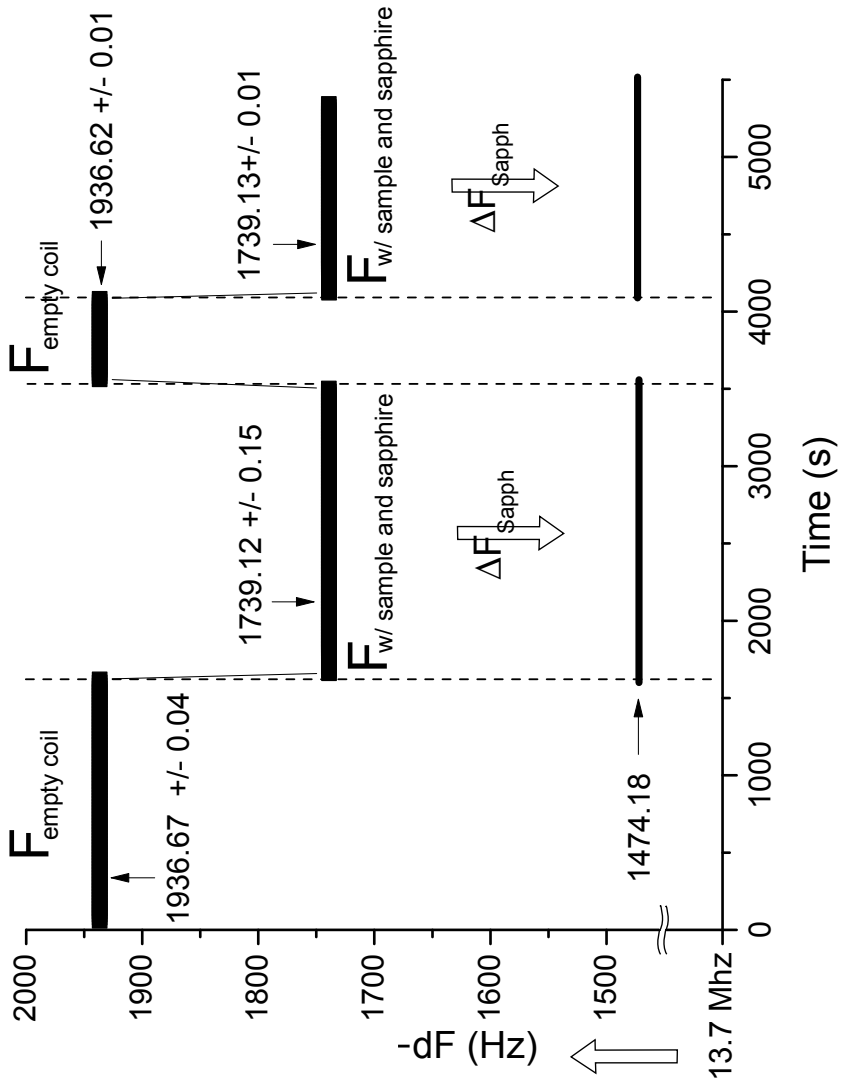

Figure 4.4: Oscillator frequency shift upon insertion of the sample at its base temperature ($T \approx 0.450$ mK). Note that a larger frequency shift corresponds to a lower actual oscillator frequency, as the shift is measured relative to a precision local oscillator that is generally kept at a higher frequency than that of the TDO. In this case the local oscillator was at 13.7 Mhz. The paramagnetism of the sapphire sample holder lowers the actual oscillator frequency and must be removed from the calculated $F_{Pullout}$.

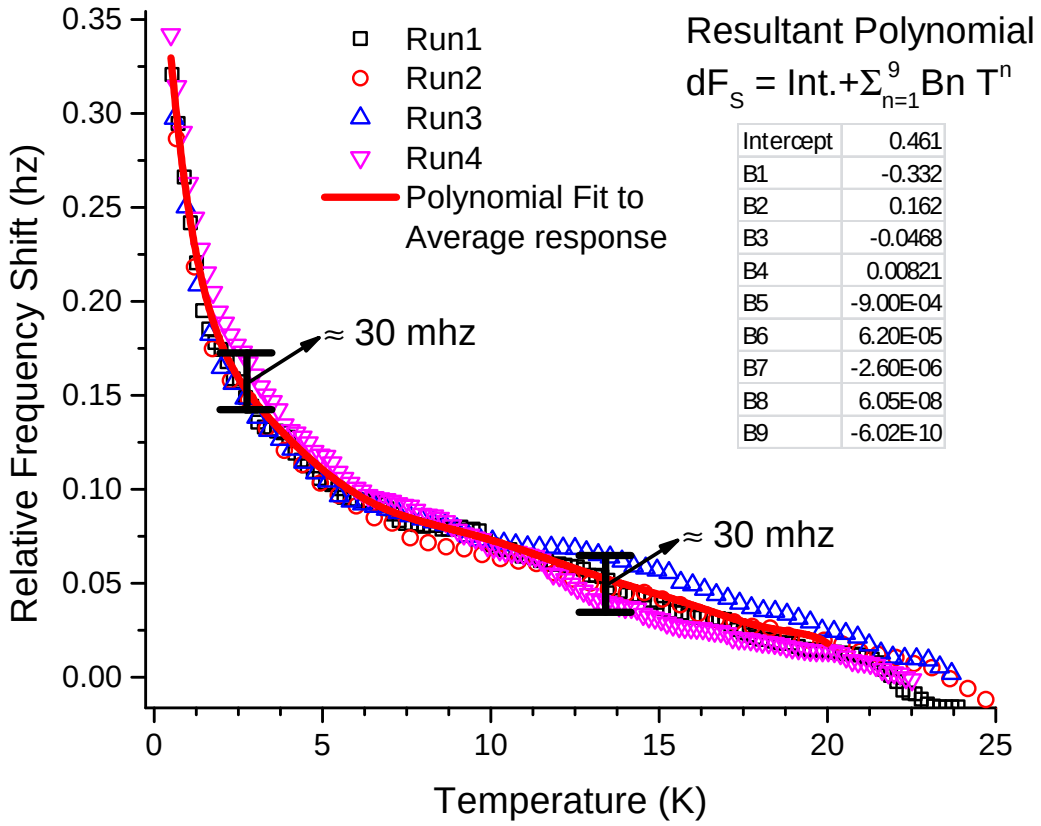

Figure 4.5: Curie-Weis like temperature dependence of the paramagnetic response of the Sapphire holder. Crystal field effects make the response somewhat more complicated than a simple $1/T$ model might predict.

mhz) on the final calculated sample penetration depth. Fortunately such error bars had minimal impact on the powerlaw fits to the low temperature data. Nor does the subtraction of the measured sapphire background leave any additional paramagnetic upturn in the low temperature penetration depth. This suggests that the columnar defects have produced no additional magnetically susceptible scattering centers in the crystals.

The low temperature behavior for both unirradiated samples, figures 4.6 and 4.7, is best described by an exponentially saturating curve that follows the BCS form of $\Delta\lambda(T) \propto \sqrt{\Delta/T}\exp^{-\Delta/T}$ with a value for the smaller gap of $\Delta_{min}/k_BT_C = 0.97$ for the unirradiated 36.8K sample and 0.99 for the higher T_C material. Interestingly the other moderately ir-

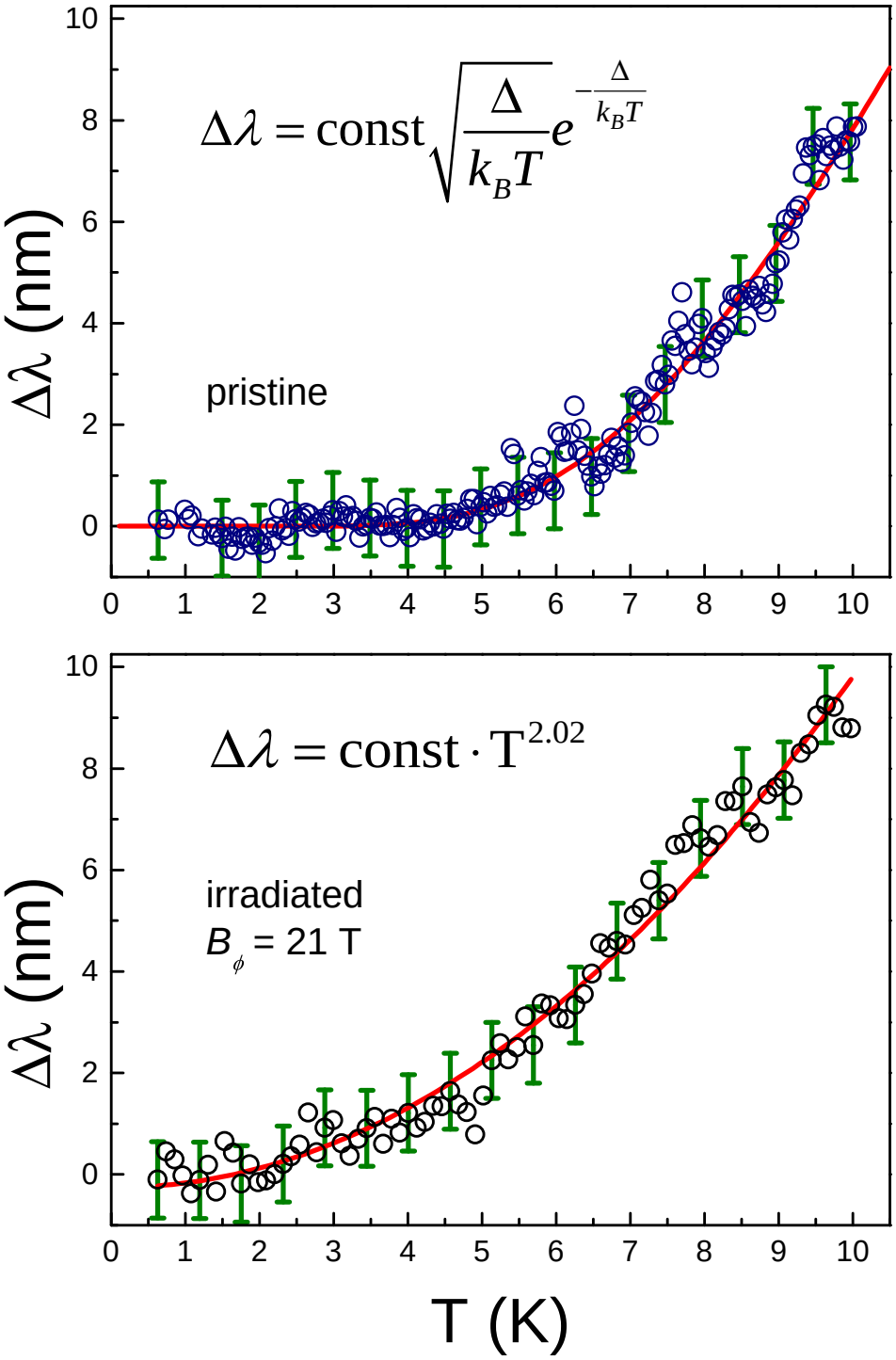

Figure 4.6: Change in penetration depth for second crystal group. (Upper) Data for unirradiated sample with BCS-like fit. (Lower) Sample with = 21 T matching field showing quadratic power law fit.

radiated samples show no change from the exponential saturation (figure 4.7) and can be fit to the BCS form for the penetration depth with gaps of $\Delta_{min}/k_BT_C = 0.99$ for the 2T sample and $\Delta_{min}/k_BT_C = 0.81$ for the 4T sample. These numbers are quite reasonable, as STM [57] and ellipsometry measurements [58] have reported gap values of $\Delta_{min}/k_BT_C = 1.1$ and reflect the general trend amoung most multigap superconductors that the smaller gap will have a value that is approximately half that of the BCS result $\Delta_{BCS}/k_BT_C = 1.76$ [42].

The transition temperatures of the crystals also remains more or less unaltered by irradiation, even up to the $B_\phi = 21T$ level where the tracks are on average spaced by only a few coherence lengths (figure 4.8). This is in sharp contrast with the nickel and cobalt doped samples irradiated in prior work where the transition temperature varied sharply ($\Delta T_C \approx$ 5K at a 2T matching field) with irradiation level [55].

The most profound result of these measurements is the evolution of the powerlaw to T^2 for the highest level of irradiation dosage 21T, which is displayed in figure 4.6. The penetration depth in that case is clearly different from the unirradiated crystal, in that it continues to vary with temperature down to temperatures of at least 400mK, which is approximately 1% of T_C. This continued low temperature variation makes it impossible to apply the BCS form to the penetration depth.

4.3 Analysis and Discussion:

The data sets plotted in Figures 4.6 and 4.8 each make persuasive points but appear to be potentially contradictory. The evolution of $\Delta\lambda(T) \propto \sqrt{\Delta/T}\exp^{-\Delta/T}$ toward $\Delta\lambda(T) \propto T^2$ is predicted for an s_{+-} order parameter. But an s_{+-} gap was also predicted to experience T_C reduction when interband scatters are added and yet none of the samples suffered any significant T_C drop even when dosed with substantial amounts of radiation.

The lack of a drop in T_C could be explained by the true gap symmetry being of the s_{++} form. Anderson's theorem, which holds that non-magnetic impurites cannot change the gap

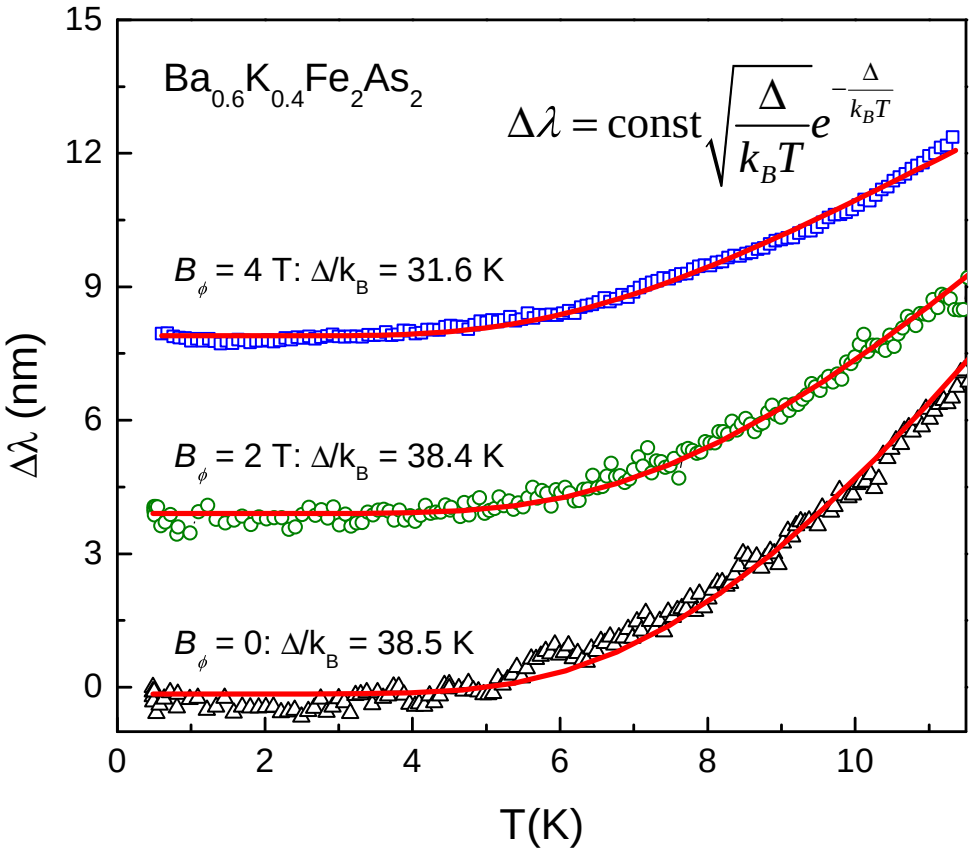

Figure 4.7: Change in penetration depth for 3 samples from first group (Tc = 39 K) for columnar defect densities of = 0 T, 2 T, 4 T. Fits to BCS temperature dependence are shown as solid curves. Data sets have been vertically offset for clarity.

value or the transition temperature, would then apply to a multiband s_{++} in just the same way as it applies to conventional superconductors. But is has been shown that even in the very dirty limit the London penetration depth should still follow an exponentially activated form meaning that a superconductor with an s_{++} gap could not cross over to having a T^2 powerlaw [42].

To reconcile these two seemingly contradictory points we must consider the nature multi-band scattering and its interactions with the gaps in somewhat more detail. Generalizations of Abrikoskov-Gorkov theory [59] show that in the limit of Born scattering, it is anisotropy

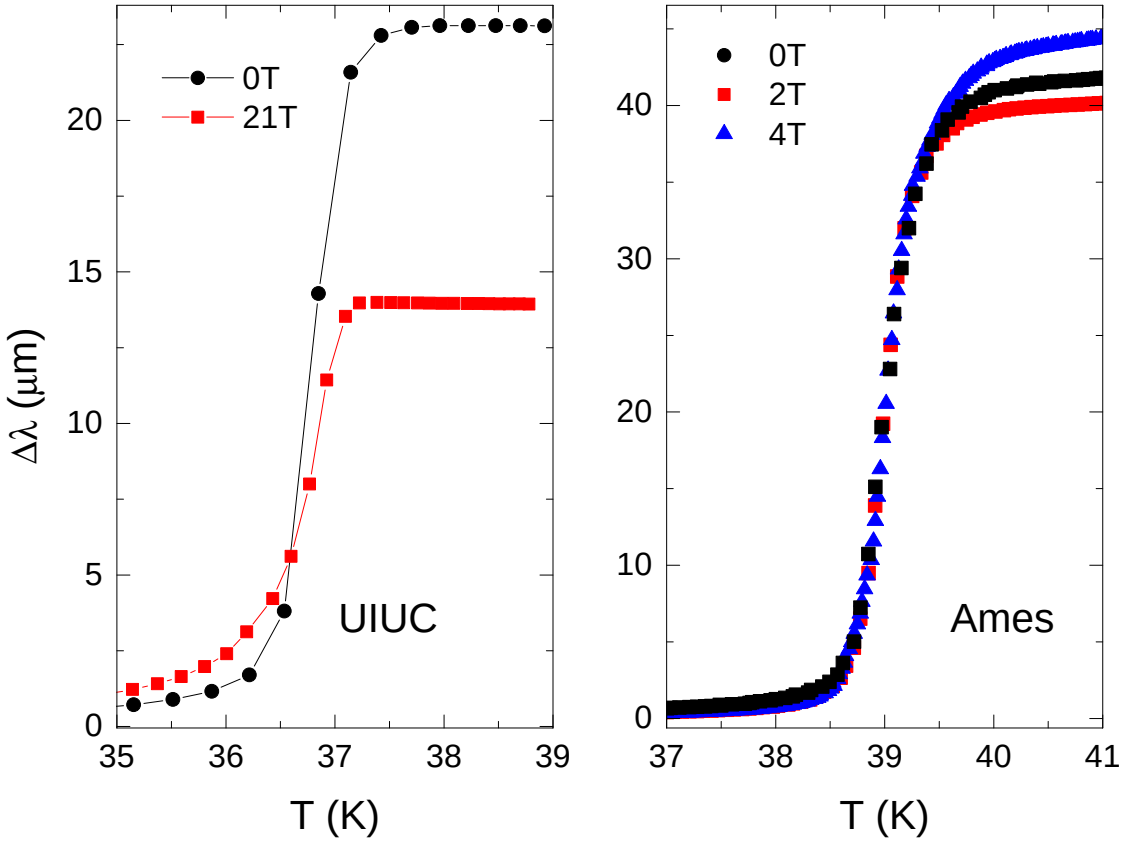

Figure 4.8: Change in penetration depth near T_C for both sample groups and different irradiation levels.

in the gap that permits non-magnetic scatters to reduce T_C [60–62]. Remarkably this fact is irrespective of whether or the gap is sign changing. The consequence of that result is that intraband scattering can only suppress T_C in materials with highly anisotropic Fermi surfaces like the electron doped cobalt based materials, but not in the much more isotropic hole doped potassium based materials.

The larger gap anisotropy in the electron doped materials has been observed in both thermal conductivity and penetration depth measurements [5, 63, 64]. Subsequent increases to interband scattering will drive $\Delta(T) \propto T^2$ for both isotropic and anistropic materials if the pairing is s_{+-}, regardless of its degree of isotropy [65]. It is of course also possible

that the additional interband scattering created by the introduction of columnar defects is in the pure unitary limit where it simply cannot suppress T_c. But this would require that the defects introduced by heavy-ion irradiation act very differently in hole doped materials compared to electron doped ones.

Though we lack a detailed microscopic understanding of the scattering produced by columnar defects it is still useful to consider our work in the context of other measurements and theoretical models. As was pointed out earlier, our work is similar to what was observed by Hashimoto et al [66] but without the possibility of inadvertent changes in the effective doping level dominating the measurement. Their earlier microwave results on unaltered K-122 crytals showed a similar powerlaw cross over from exponential to $\Delta\lambda \propto T^2$ that was correlated with increases in the simultaneously measured surface resistivity of their crystals. They also saw the T_C drop from 32.7 to 25K as their scattering rates (surface resistivity) increased. Unfortunately they were not able to distinguish between impurity induced increases to interband scattering and differences in effective doping because they were comparing different crystals.

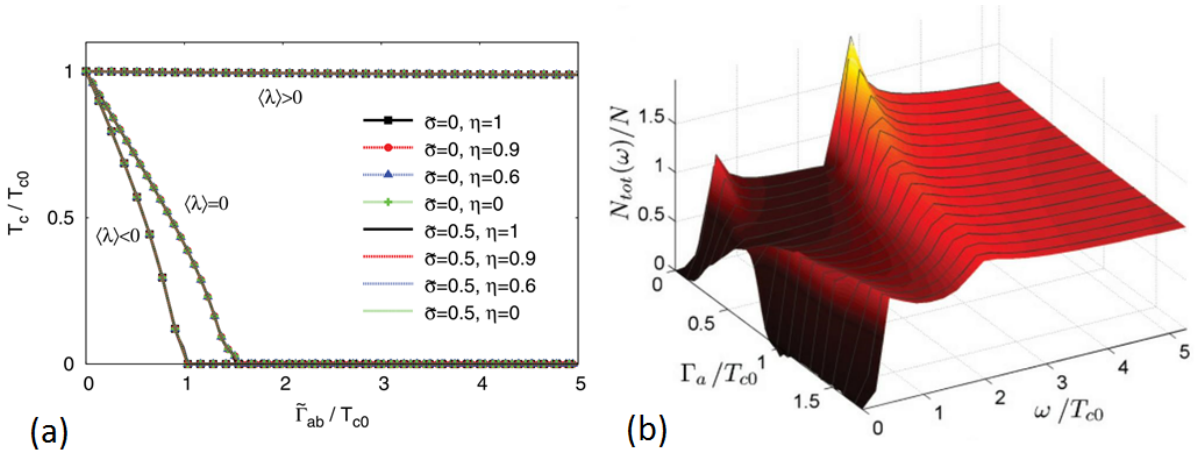

Figure 4.9: (a) Sensitivty of T_C to impurities. Γ_{ab} is the effective interband scattering rate. $\langle\lambda\rangle$ is the effective band coupling parameter. (b) Evolution of the gap structure with scattering in a $\langle\lambda\rangle > 0$ scenario [6].

Some recent theoretical work might be able to encompass both our result and the earlier microwave measurements on Potassium-122. The authors identify two different subtypes of

s_{+-} pairing, depending on the sign of the pairing interaction averaged over two bands (figure 4.9(a)) [6, 49]. If that averaged interaction comes out as repulsive it will cause the effective powerlaw to drop as well as drive the T_C to zero in a typical Abrikosov-Gorkov scenario [59]. This could have been the cause of behavior measured by Hashimoto.

If on the other hand the averaged interaction is attractive then scattering can actually tune from the fully gapped initial state through a state where the smallest gap crosses to zero which yields a powerlaw dependence in the penetration depth but does not lower the T_C. Columnar defects are in principle very different than chemical disorder and could be preferentially causing this very form of scattering. Startlingly, the theory predicts that further increases in the scattering rate will then actually lead the system into s_{++} pairing and restore an exponentially activated character to the penetration depth (figure 4.9(b)). Such a reentrant change in powerlaw character would alas, require a higher defect density than was available even at $B_\phi = 21T$.

With this issue in mind, a brief digression about the microscopic nature of the columnar defects produced by heavy ion bombardment is warranted. A matching field of 21T corresponds to average column separation of 10 nm. Prior plan view TEM work has shown that the columns are 3.7 nm in typical diameter, meaning that the superfluid density is likely confined to the 6 nm of undisturbed material left between columns. Given that the coherence length is somewhere between 2-3 nm, this means that at our highest defect level superconductivity is ostensibly contained entirely within regions comparable to the minimum size scale in which superconductivity could exist.

This potentially extreme localization is somewhat softened by results obtained from cross sectional TEM of the columnar defects in irradiated crystals. The columns were demonstrated to be not fully continuous along the c axis. Rather they defects form as something more like a a chain of "cigars on a string". It is also somewhat surprising that the actual number of defects as revealed by electron microscopy is actually much smaller than what would be expected for the administered dose of ions. It is thought that at high doses there

is a fairly high probability that ions hit close to the track of previous impacts, leading to highly non-uniform damage and local strain fields.

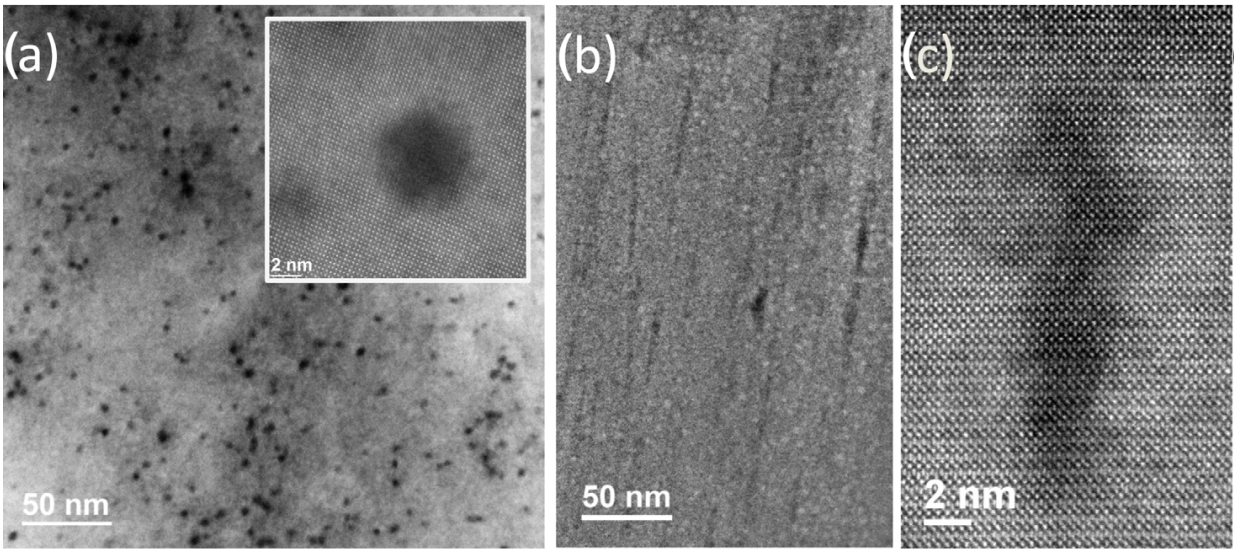

Figure 4.10: Images from plan view (a), cross-sectional (b), and atomic resolution cross-section (c) Transmission Electron Microscopy performed on heavy ion irradiated single crystals. The tracks appear as black amorphous areas that cover approximately %5 of the area in the plan view. They form as discontinuous streaks in the cross-sectional view [7].

Given the already extremely close spacing of defects at the 21T matching field it is natural to wonder if higher dosages generate effects beyond the simple increase in scattering that seems to be displayed in the 21T sample. Some limited data is available at such higher doses, which seems to suggest that superconductivity persists up to even $B_\phi = 50T$, though with a pronouncedly reduced and broadened T_C [7]. But such high doses are exceptionally hard to apply without causing severe thermal damage to the sample during application so other effects could be involved beyond simple changes in scattering.

The coexistence of spin density wave (SDW) ordering may also be an important variable. The SDW phase is known to coexist with superconductivity in both cobalt and potassium doped materials within some portion of each materials superconducting dome [11, 67–69]. Disorder has been calculated to surpress the SDW phase which will reduce competition possibly enhanace T_C [50]. This result when combined with the inherent uncertainty in the

local coexistance or non-coexistence of SDW ordering in the superconducting state, makes detailed analysis of T_C variation somewhat difficult.

Comparisons of $Ba_{0.6}K_{0.4}Fe_2As_2$ to MgB_2 are quite natural, given that both are only weakly aniostropic multiband superconductors with very similar T_Cs and two unequal energy gaps [70]. Chikumoto et al. irradiated MgB_2 samples with 5.8 GeV Pb ions and reported no change in T_C for matching elds up to B_ϕ= 4 T [71]. However, in contrast with Hashimoto et al's results on early potassium doped samples, no variation from exponential activation in the penetration depth has ever been seen for MgB_2. It has been suggested that the resiliancy of MgB_2's transition temperature is due to a pecularity of its band structure [72, 73]

4.4 Recommendations for future work:

The observation of reentrant powerlaw which changed from exponential to quadratic to exponential again would be very compelling. Reliably administering the incredibly high doses demanded by this prediction without horribly damaging the samples is a very interesting experimental question. Improvements of our microscopic understanding of defects and their interactions the complicated many-body state of the system is another challenging frontier. Extending these measurements to electron irradiation, which produces point defects rather than amorphous columnar tracks, could be of some interest.

Chapter 5

Doping Evolution of the Absolute Penetration Depth and Superfluid Density in $Ba(Fe_{1-x}Co_x)_2As_2$:

5.1 Introduction:

5.1.1 Competing Orders in Highly Correlated Materials:

Whether or not magnetism can coexist with superconductivity on a microscopic scale is one of the central questions in the study of highly correlated matter. The two orders should in principle have an antagonistic interaction, but measurements in systems such as high-T_C superconductors [74], heavy fermion materials [75–78], and organics superconductors [79] have discovered that they are in fact very closely coupled.

Such a relationship might be the key to understanding high temperature superconductivity. At the minimum it has inspired many publications [80–84]. However, many different materials have been shown to sidestep the question of coexistence by either through macroscopic separation, mesoscopic phase separation, or even intrinsic separation from each other because they occur in distinct electronic subsystems within the main branch of conduction electrons [85].

The question of true local coexistence between long range AFM order and superconductivity has not been definitively settled the iron pnictides [**?**, 86–90]. In some materials such as the '1111's it is clear that AFM ordering is completely surpressed well before superconductivity emerges [91]. There is reasonable evidence in the cobalt-122s that AFM ordering persists almost all of the way to optimal doping and does not separate from the local superconducting order [86]. But given the wide variety of previously discovered ways by which

highly correlated materials can avoid intimate contact between competing orders, studies of whether or not such phases can truly coexist are very well deserved.

5.1.2 Antiferromagnetic Ordering in $Ba(Fe_{1-x}Co_x)_2As_2$:

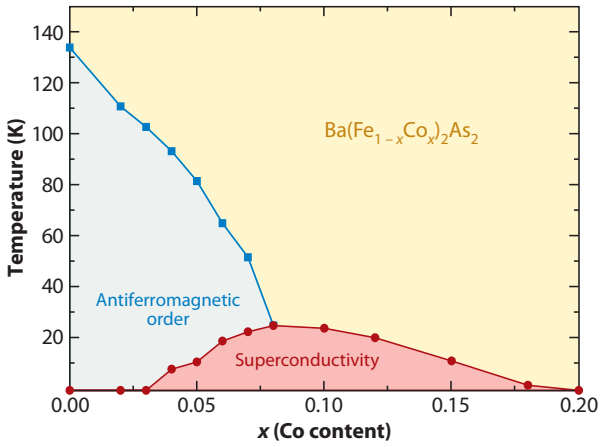

Figure 5.1: Phase Diagram for $Ba(Fe_{1-x}Co_x)_2As_2$ [1].

Dopants in $BaFe_2As_2$ destroy the low temperature spin density wave order in the parent compound. The effect of the spin density wave transition on the fermi surface can be understood by considering a band-folding model in the parent compound [9]. Above 140K the Fermi surface of $BaFe_2As_2$ can be modeled by one hole pocket centered at the Γ point and four electron pockets at the M points, as was described earlier (chapter 3). It should also be noted that the material is a reasonably well compensated metal, with equal volumes of electron and hole pockets.

Below the 140K transition temperature it experiences a structural and magnetic transition to an AFM SDW state with a unit cell that is rougly $\sqrt{2}$ larger and rotated by 45 degrees relative to the room temperature state (figure 5.2 a). This change in structure means that the electron band must be folded back to zone center(figure 5.2 b). The hole band and electron bands then cross and hybridize to form a gap at the Fermi level, which would make the material insulating, were the bands fully symmetric (figure 5.2 c).

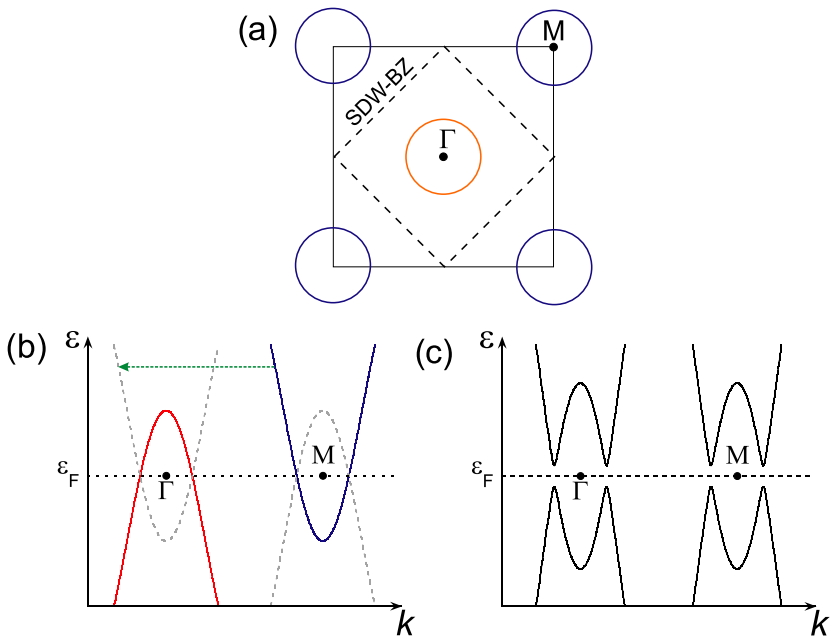

Figure 5.2: Fermi surface changes during the SDW transition as modelled by a band-folding argument. See the text for details [8, 9].

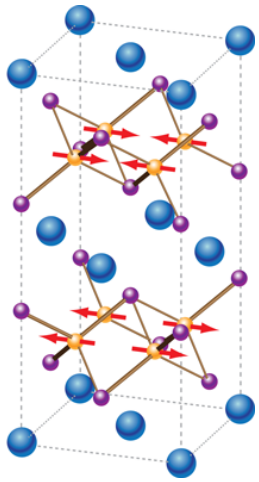

Figure 5.3: Spins on Iron atoms (yellow) in $BaFe_2As_2$ form a Spin Density Wave, also known as an intinerant antiferromagnet, below 140K. In contrast to a Mott Insulator, where spins lower their energy by becoming antiparallel to their neighbors, an SDW state involves an instablity in the Fermi surface [10].

Of course the bands do not have exactly the same in-plane shape and are not fully two dimensional, so small three dimensional Fermi pockets will remain, even in the hybridized state. Such residual hole pockets can be seen via ARPES and will be discussed in more detail

later in this chapter. The role of the cobalt atoms in bringing about the superconducting state is to neutralize the SDW ordering of the parent compound and effectively reverse the phase transition just described.

5.2 Experimental Methods:

5.2.1 Preliminary Sample Characterization:

The $Ba(Fe_{1-x}Co_x)_2As_2$ series samples used for these measurements were obtained from the group of Professor Paul Canfield at Iowa State/Ames Lab. Magneto-optical imaging at Ames established the uniformity of superconducting order down to the optical diffraction limit of approximately 1 μm.

Cobalt concentrations were determined by electron-probe x-ray microanalysis using wavelength dispersive spectroscopy (WDS). This was one check on the uncertainty of the cobalt concentration in each crystal, which was found to vary by as much as 0.0015 atomic percent (equivalent to 5% of the cobalt level in an underdoped crystal). Slight variations in concentration can have very pronounced effects on T_C when the effective sample doping is near either edge of the superconducting dome.

By this reasoning local in-homogeneities in the doping level should cause the transition region to be substantially broadened when measured with a bulk probe. Under such conditions, the total sample diamagnetism at any given temperature would be the sum of several different sample regions with different T_Cs. To avoid such effects, all the samples selected for measurement were first established to have comparably sized transition widths. Unfortunately, this meant the exclusion of samples with more than 10% cobalt doping because none of these highly doped samples were found to have widths as narrow as samples with lower doping levels.

5.2.2 Coating Procedure:

Deposition of a low T_C coating is necessary to extract $\lambda_L(0)$ data from the $\Delta\lambda(T)$ directly produced by conventional tunnel diode oscillator measurements, for reasons that were described earlier. The central requirement of the technique is that the film completely envelops the sample. The difference in screening between when the film is normal and when the film is superconducting will be related to the $\lambda_{sample}(T = 0)$. The technique was first demonstrated on several different cuprate superconductors [92].

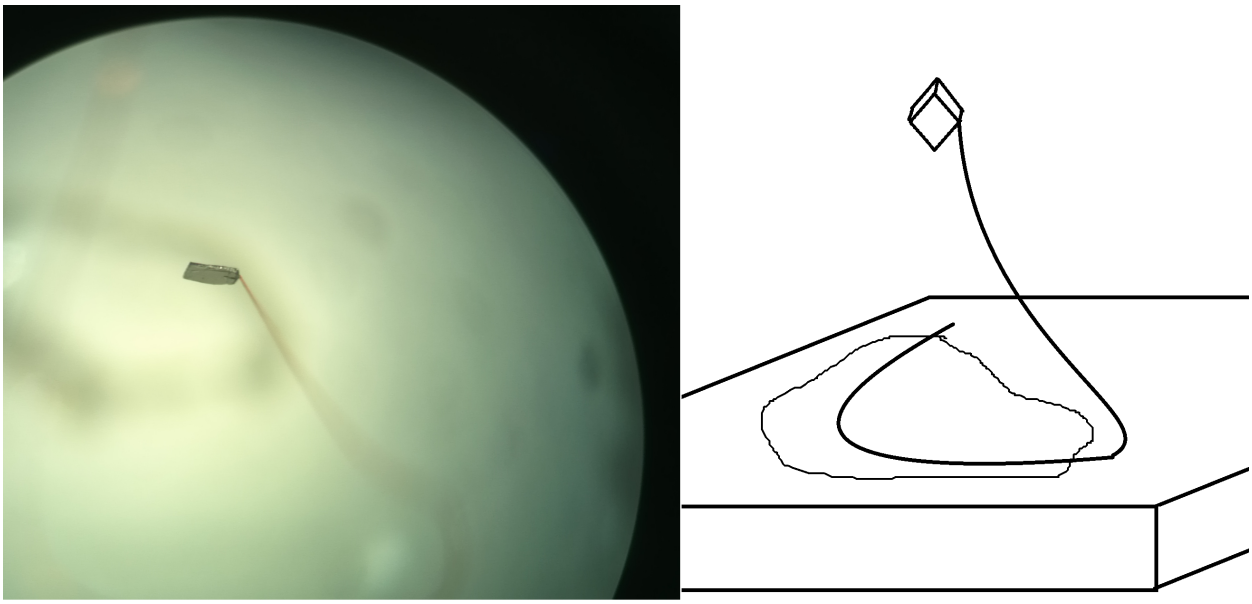

Figure 5.4: Left: Microscope photo of a sample suspended by a fine wire. Right: Schematic drawing for clarity.

Each sample was coated while it was suspended from a fine wire (figure 5.4) that was attached to the rotating stage of an argon atmosphere magnetron sputtering system. The formation of significant non-uniformities or occluded regions in the film was avoided by bonding the wire to only a portion of the narrowest edge of each sample. The relatively high background pressure of argon (5mT) and low residual oxygen level of the high vacuum sputtering system ensured that the film would be homogenous over several square centimeters and uniformly coat all surfaces.

5.2.3 Film Analysis with Focussed Ion Beam Microscopy:

The quality and uniformity of the coating was checked locally by Focused Ion Beam cross-sectioning. Focused Ion beam microscopy is a dual beam technique wherein a conventional SEM is used to image modifications pattered in the sample by a focussed Gallium ion beam. The Gallium ion beam is of sufficient energy and flux that it can controllably ion mill patterns into a sample with resolution comparable to the imaging capability of the SEM.

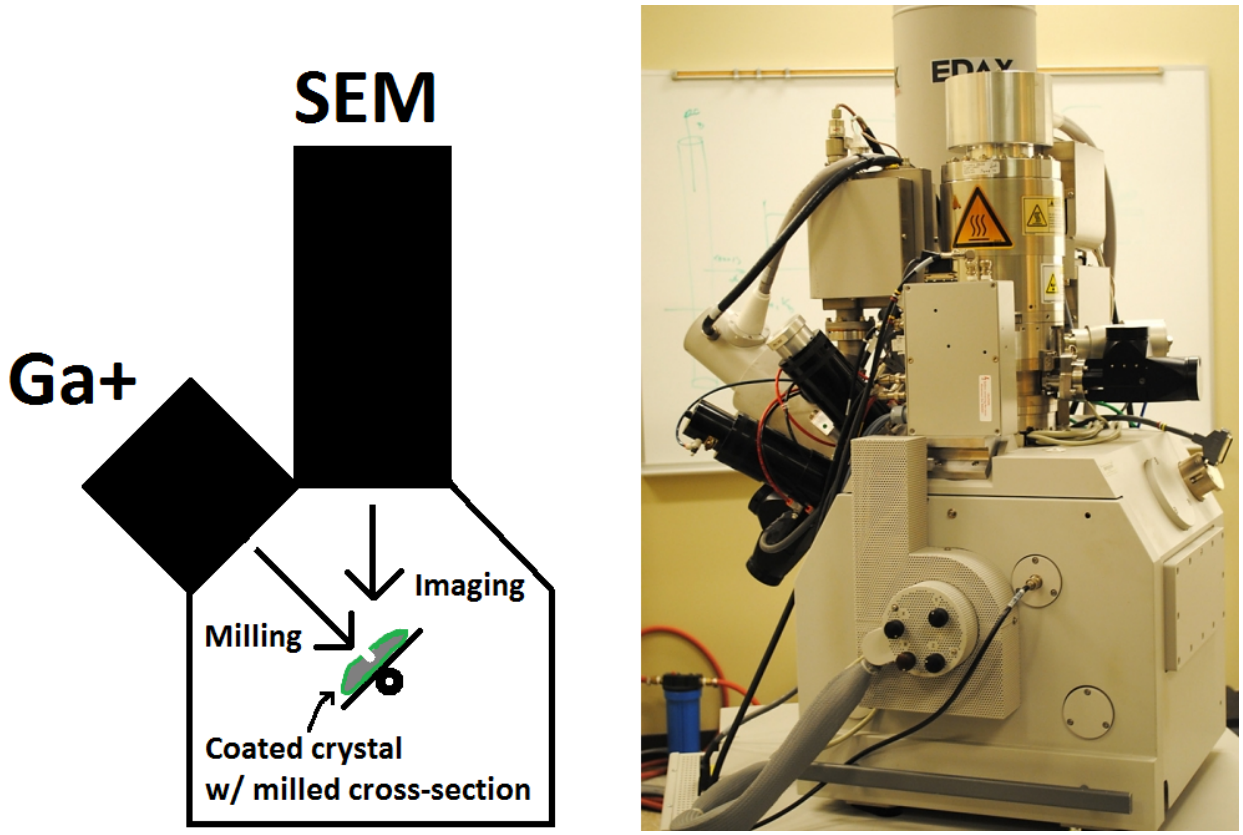

Figure 5.5: Left: Schematic of FIB cross-sectioning process. Right: Photograph of actual FIB instrument.

FIB is particularly suitable for measuring variations of the film thickness on a local scale across the potentially irregular surface of a crystal that is typically less than half a millimeter in any dimension. The coated crystal is mounted a stage with its c-axis is parallel to the beamline of the gallium source so that the focused ions can be used to mill a trench into the sample. The SEM is mounted at a skewed angle away from the axis of the gallium

beamline, so that it can image the sample from a roughly 45 degree angle (figure 5.5). Simple trigonometry then allows one to project out the c-axis thickness of the film. A typical cross section is pictured in figure 5.7. The degree to which the film conforms to irregularities in the sample shape and its uniformity across large distances can also be evaluated quite easily using this technique. Several such cross sections are presented in figure 5.6.

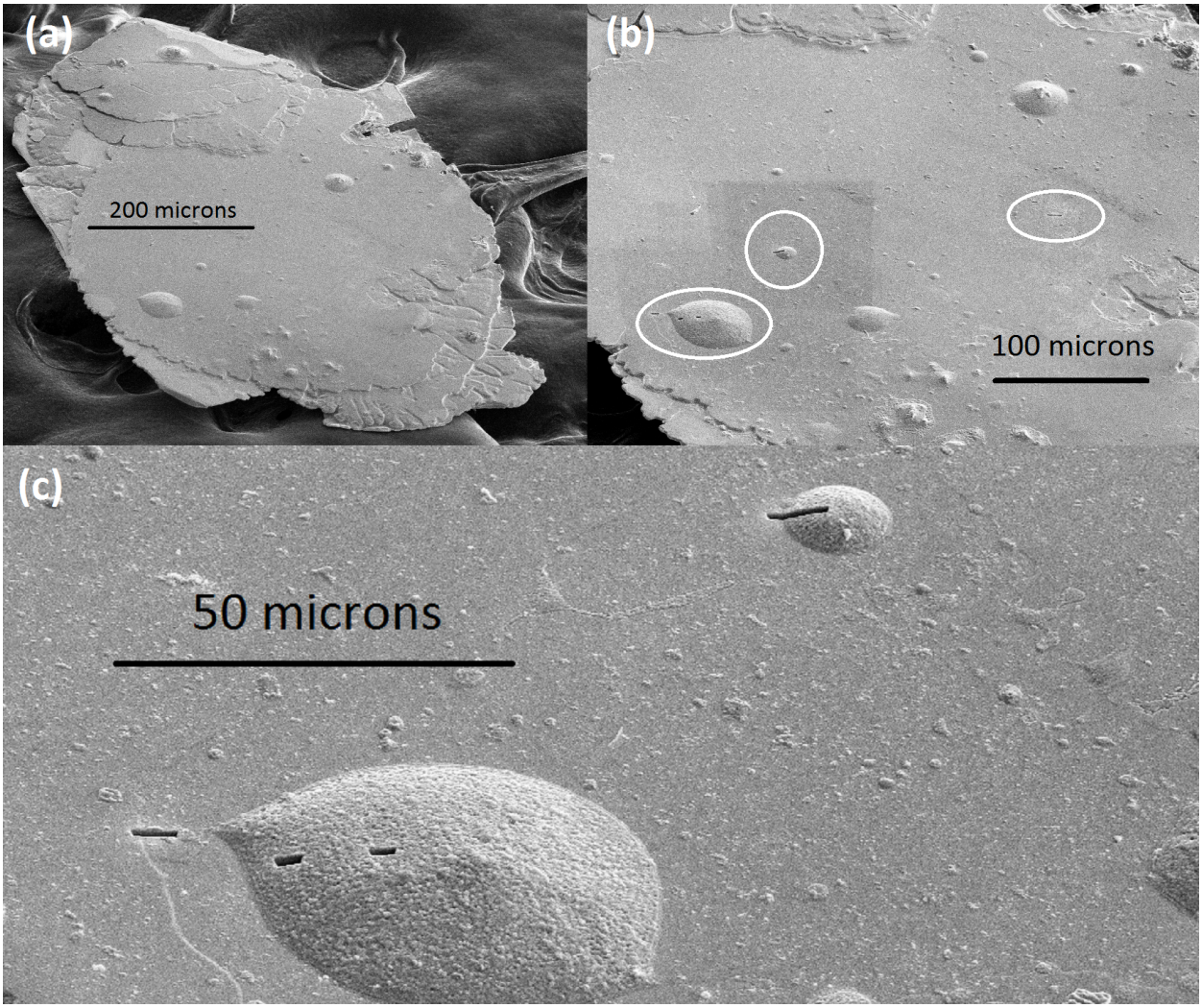

Figure 5.6: SEM images of a single crystal sample. (a) Overview of the sample from a tilted angle. (b) Blowup showing locations of different trenches across the sample (white circles) (c) Further zoom in on trenches. Cross-sectioning demonstrated that in this case the hemisphereical protusions visible in c were actually intrinsic to the crystal.

Beyond its capacity for micron scale localized measurements, the FIB is particularly useful in that it produces direct images of the film cross-section. Many other techniques

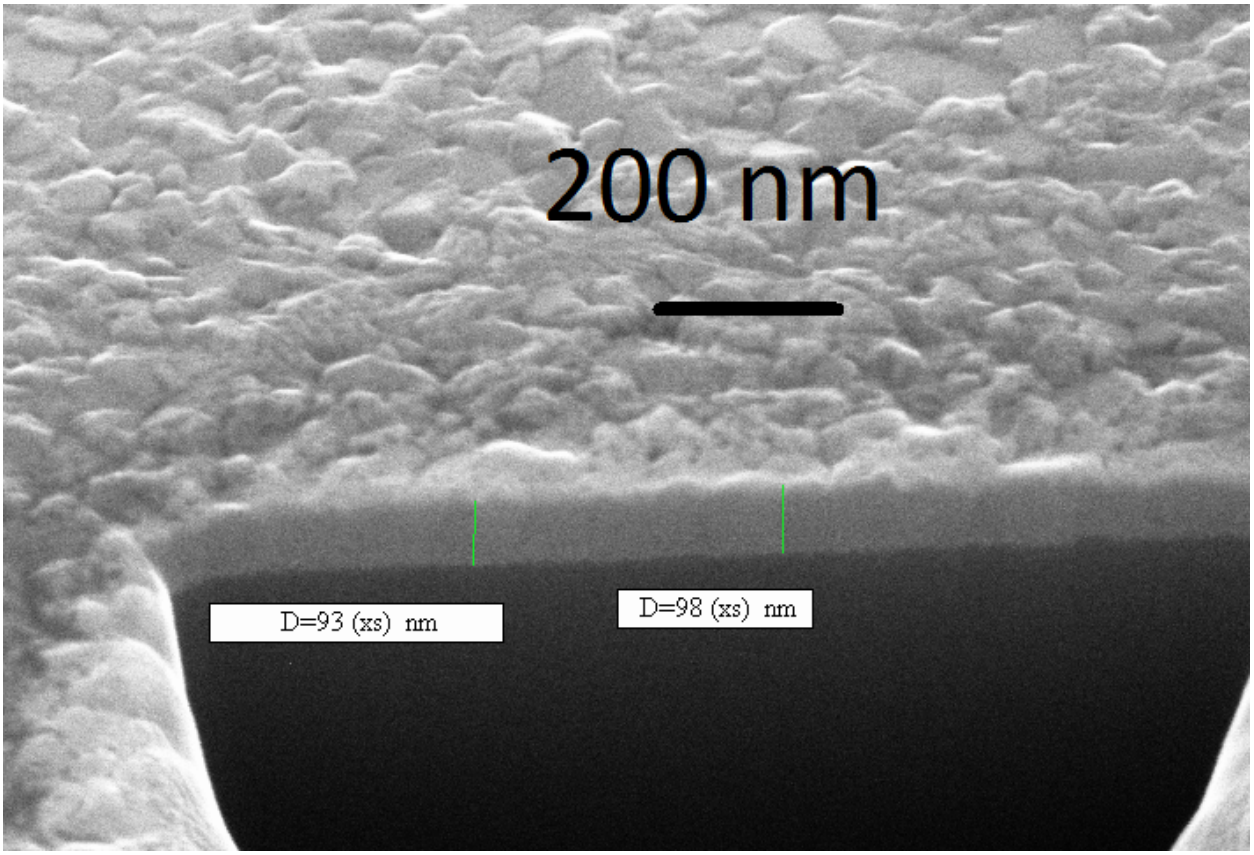

Figure 5.7: A typical trench cross section viewed from a 52 degree angle. Projected film thickness are labeled with an (xs).

deduce the film thickness out of fits to complicated models (ellipsometry), can be overly sensitive to surface roughness (x-ray reflectivity), or require extra care in sample preparation (AFM/TEM). But there can still be issues with drift and length scale calibration in the SEM, so it is worthwhile to test the trigonometrically projected film thickness against an appropriately sized length scale. Figure 5.8 displays a nominally 460 nm polystyrene microsphere that has been deposited from solution onto a piece of silicon sputter coated with aluminum. The measured sphere diameter of 450 nm as determined from the process outlined above corresponds very well with the manufacturers supplied dimensions and verifies that the dimensional calibration of the SEM is correct, even in the skewed geometry needed for accurate cross-sections.

The capacity of the FIB to evaluate film thickness even for very difficult geometries is

demonstrated in figure 5.9. A small piece of silicon was scribed into the form of a long strip, mounted so that it projected downward in the sputtering system just like a sample would, and coated under the same conditions as the samples. The sharp edges of the scribed silicon (inset in figure 5.9) were then cross-sectioned to test the sputtering system's capacity to conformally coat sharp edges. As is evident from the figure, the coating is excellent, even for very sharp corners.

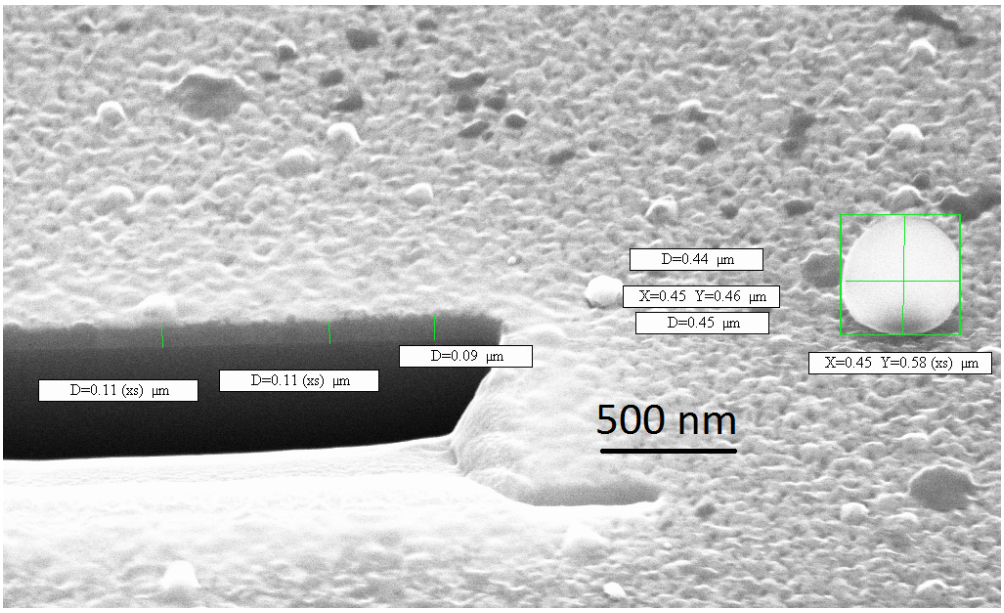

Figure 5.8: A cross-section in a film next to a polystyrene bead of 0.45 nm diameter.

5.3 Experimental Results:

Typical data for the$Ba(Fe_{1-x}Co_x)_2As_2$ crystals before and after coating in this work is displayed in figure 5.10. Above the transition temperature of the Aluminum coating, $T_C \approx 1.2K$, $\Delta\lambda_{ab}(T)$ is unchanged by the coating. Below the T_{C-Al} the coated crystal displays a sudden new drop in penetration depth. This additional screening factor is the key ruler that allows for calculation of the absolute penetration depth $\lambda_{ab}(0)$ in the coated crystal, according to the method described in chapter 2.

The striking result obtained from this method is that the $\lambda_{ab}(0)$ values determined by

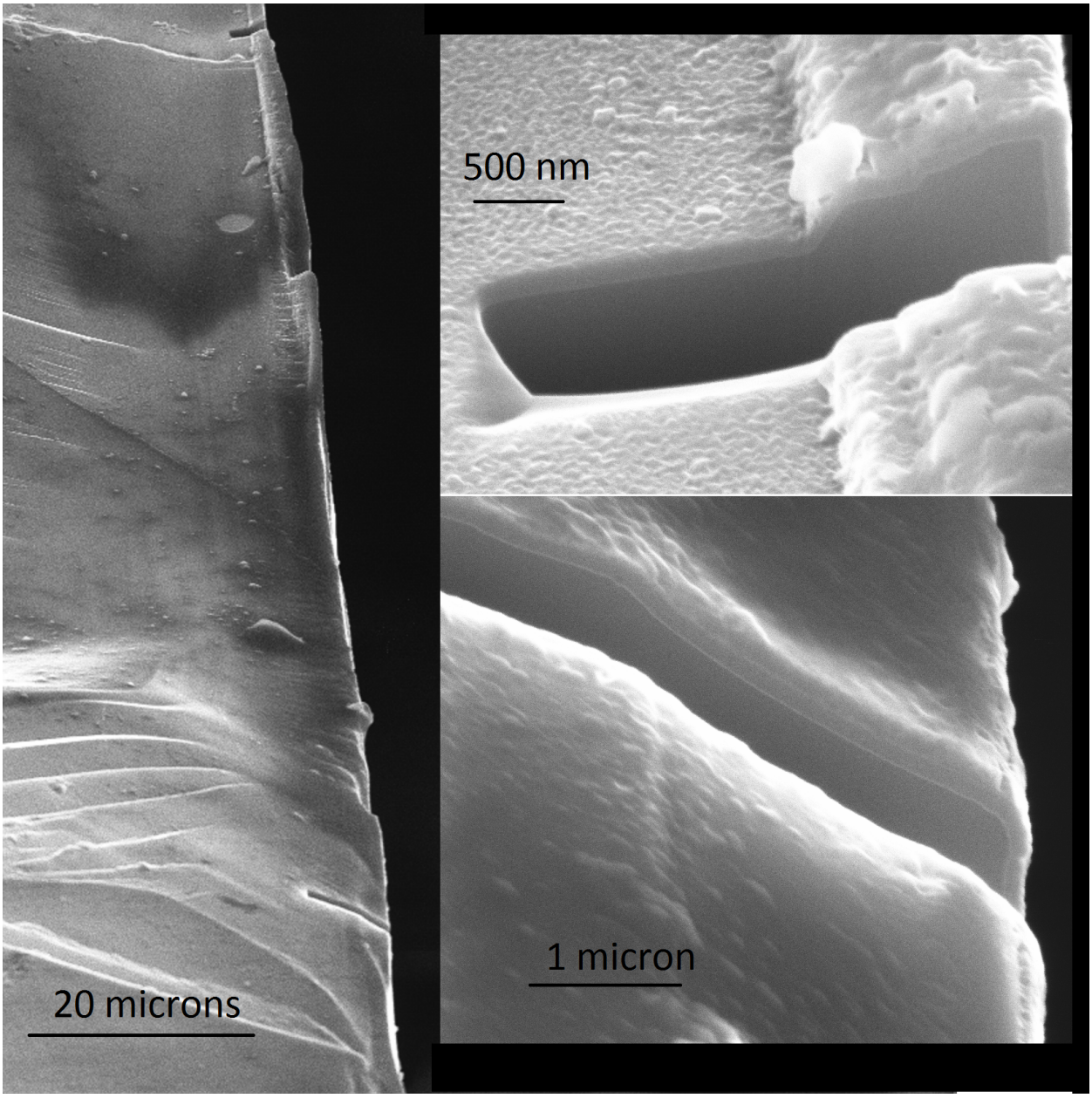

Figure 5.9: A scribed piece of silicon coated in the same way as the samples and cross-sectioned along the edges at two points near the top and the bottom of the frame (inset). This demonstartes the ability of sputtered films to conformly coat both slowly varying corners and very sharp edges.

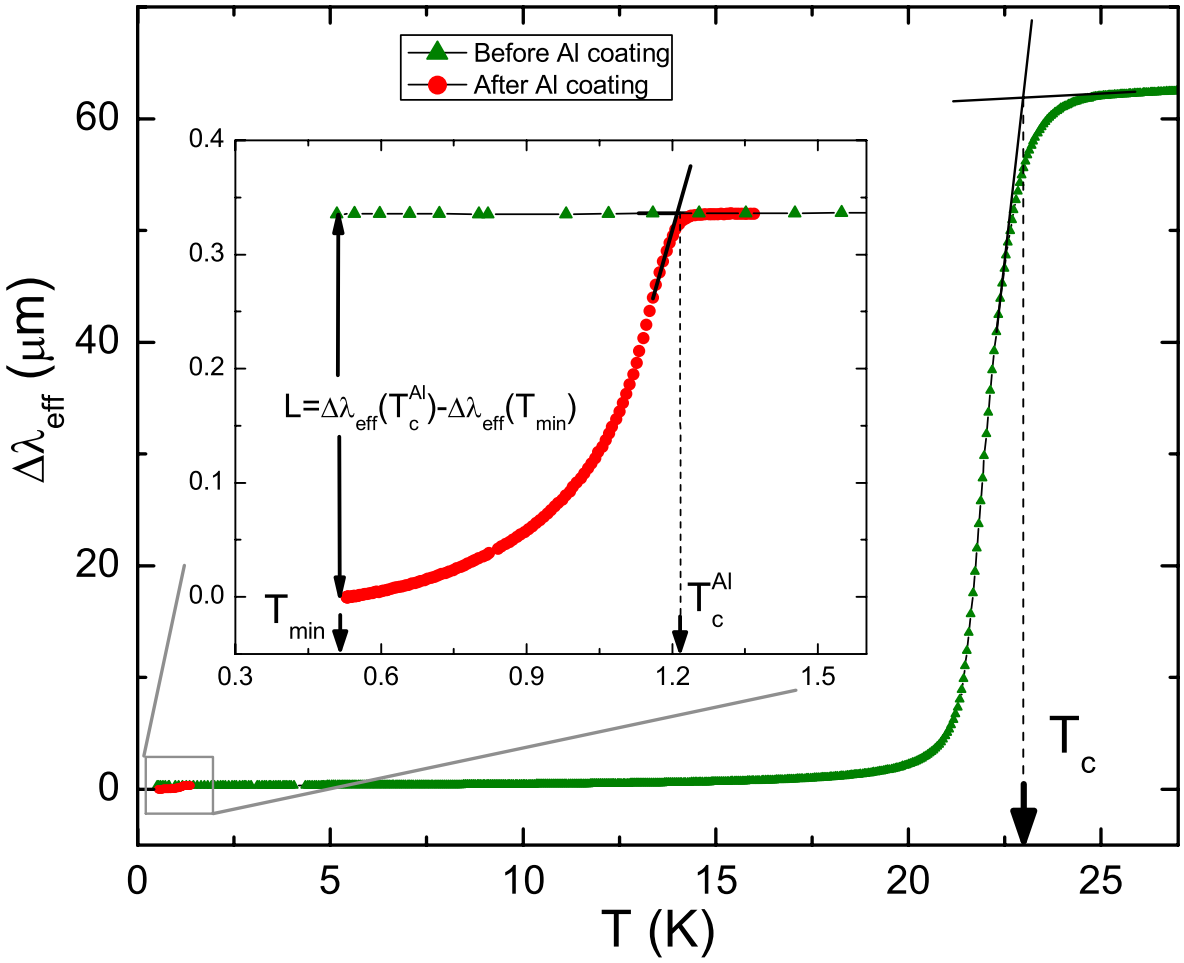

Figure 5.10: Full change in penetration depth [11] for an optimally doped $Ba(Fe_{0.93Co_{0.07})_2As_2}$ crystal before and after coating. Inset: Blow of low temperatre region with uncoated data (green triangles) and remeasured coated data (red circles). The overall shift when the aluminum becomes superconducting is used to calculated $\lambda_{ab}(0)$.

this technique rise by a factor of 2-3 as the cobalt concentration is lowered below the level that produces an optimal T_C. This data is shown in the top panel of figure 5.11 The lower panel displays the phase diagram for ease of comparison, as well as to highlight the region where superconductivity and antiferromagnetism might coexist. Error bars attached to each data point arise from the propagation of the expected uncertainties in film thickness, $t = 100 \pm 10nm$, and the zero temperature penetration depth of the aluminum $\lambda(0) = 50 \pm 10nm$. Other measurements of $\lambda_{ab}(0)$ available prior to the publication of this data are in the figure

as well. There is a general agreement between different measurements, though the spread is somewhat large.

The difference between our TDO measures of $\lambda(0)$ values is generally within the range expected from uncertainties in the film coating, though does exceed this expected statistical at certain doping levels (0.04). Whether this is caused by issues related to the aluminum layers that were applied to those crystals or by discrepancies in the quality of the samples is difficult to establish. Certainly the spread in T_C's evident in the underdoped crystals seems to suggest that sample issues are the likely culprit. The other possibility is of course that the errors find their source in the aluminum coating procedure.

5.4 Quality Control and Error analysis:

Certain obvious failure modes were discovered in samples excluded from figure 5.11 because defects there were apparent under SEM. For instance, the coating on one sample was missing in some regions (figure 5.13). This was probably due to residual organic contamination remaining on the sample surface during coating despite serious efforts to clean the sample surfaces prior to coating. Such contamination would act as a liftoff mask for a form of unintentional lithography. It would be coated uniformly during deposition but then wash away in the acetone bath used to dismount the sample from its support wire. The dissolution of the organic layer would carry away the aluminum that had previously covered it. It is uncertain whether that organic contamination was due to stray glue remaining from the wire bonding process or the consequence of thermal contact grease from prior measurements that was never quite removed.

In the limit where aluminum coating boundary value problem can be approximated as the simple difference between the penetration depth of the sample λ_{FBS} plus the film thickness t and the penetration of the film $\lambda_A l(0)$, it is clearly apparent that the answer for $\lambda_{FBS}(0)$ as estimed by the quantity L (see figure 5.10) by such a "patchy' sample be reduced in

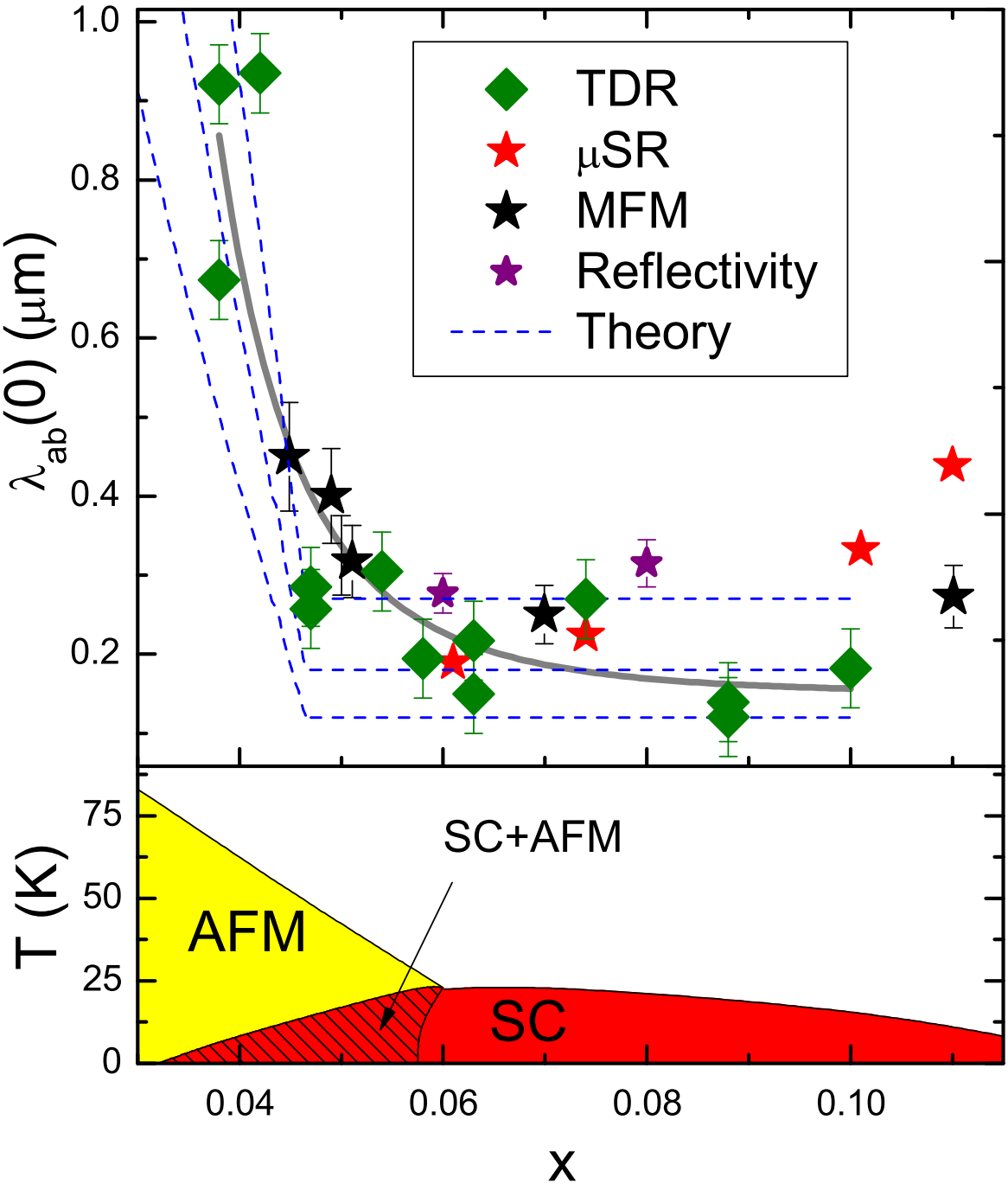

Figure 5.11: Top panel: $\lambda_{ab}(0)$ as a function of cobalt doping x [11]. The three blue dashed lines are theoretical curves that are discussed in the text. Also plotted are values for $\lambda_{ab}(0)$ obtained by different groups using different techniques. Additional $\lambda_{ab}(0)$ data taken by MFM and SSQM measurements [12] is plotted as black stars. Dashed lines represents fits to a model describing the effect of competition between the SC and SDW Phase (see text for details). Bottom panel: Nominal phase diagram for $Ba(Fe_{1-x}Co_x)_2As_2$.

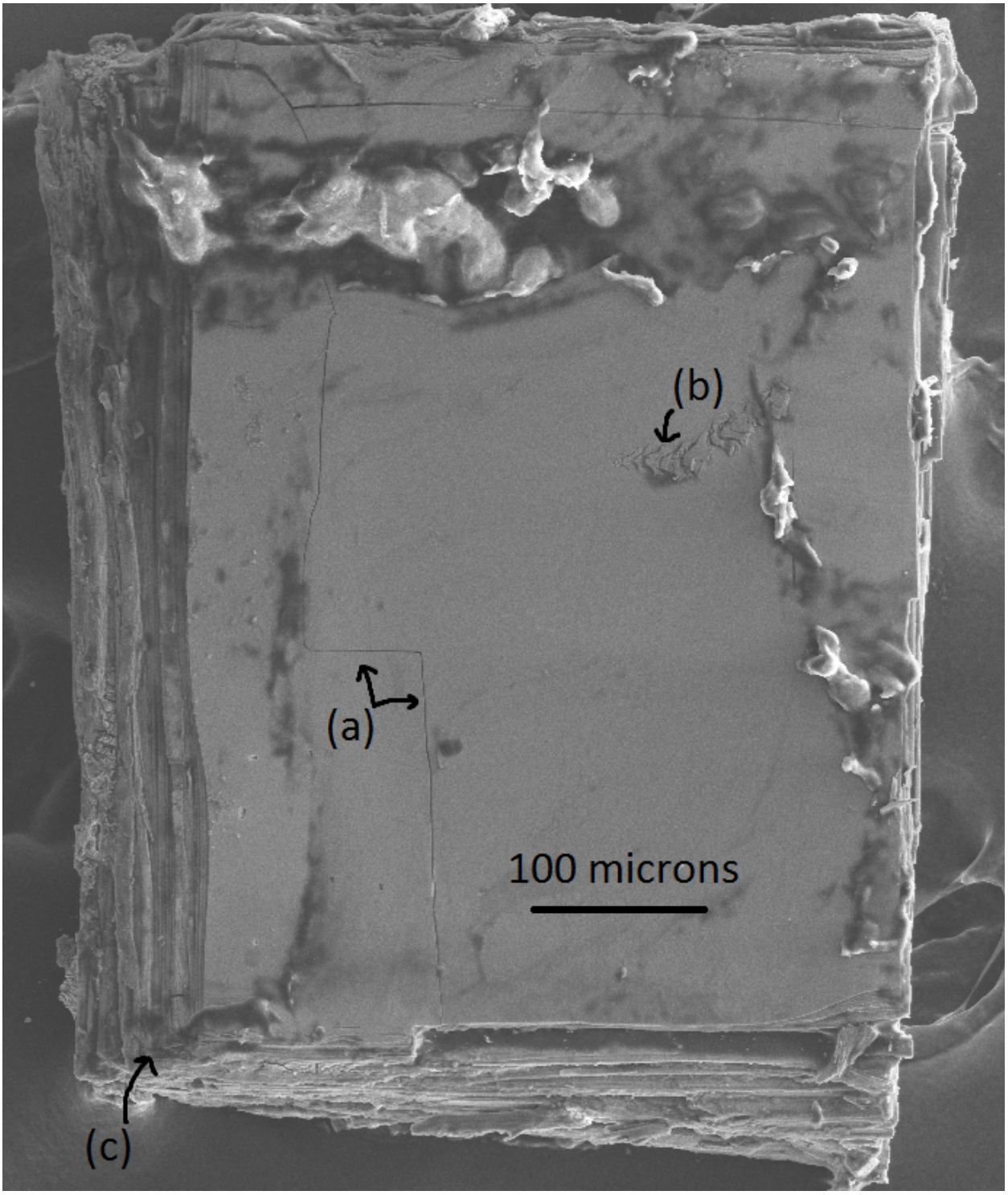

Figure 5.12: Top down SEM image of a typical cobalt doped crystal. (a) Long crack propogating through crystal. (b) Unusual surface features. (c) Bookended edges typical of the crystals studied. Bright areas are (electrically insulating) vacuum grease used for thermal contact during the second round of measurements following the coating process.

proportion to the area that is uncovered. This is because the total signal can be described as:

$$L = \lambda_{FBS}(0) + \tau - \lambda_{al}(0) = g_{sens.}(Area_{Sample})(\Delta F(T_C(AL) - \Delta F(T_C(AL)) \tag{5.1}$$

If the coated area does not equal the sample area, as in figure 5.13, $A_{Sample.}$ will be reduced

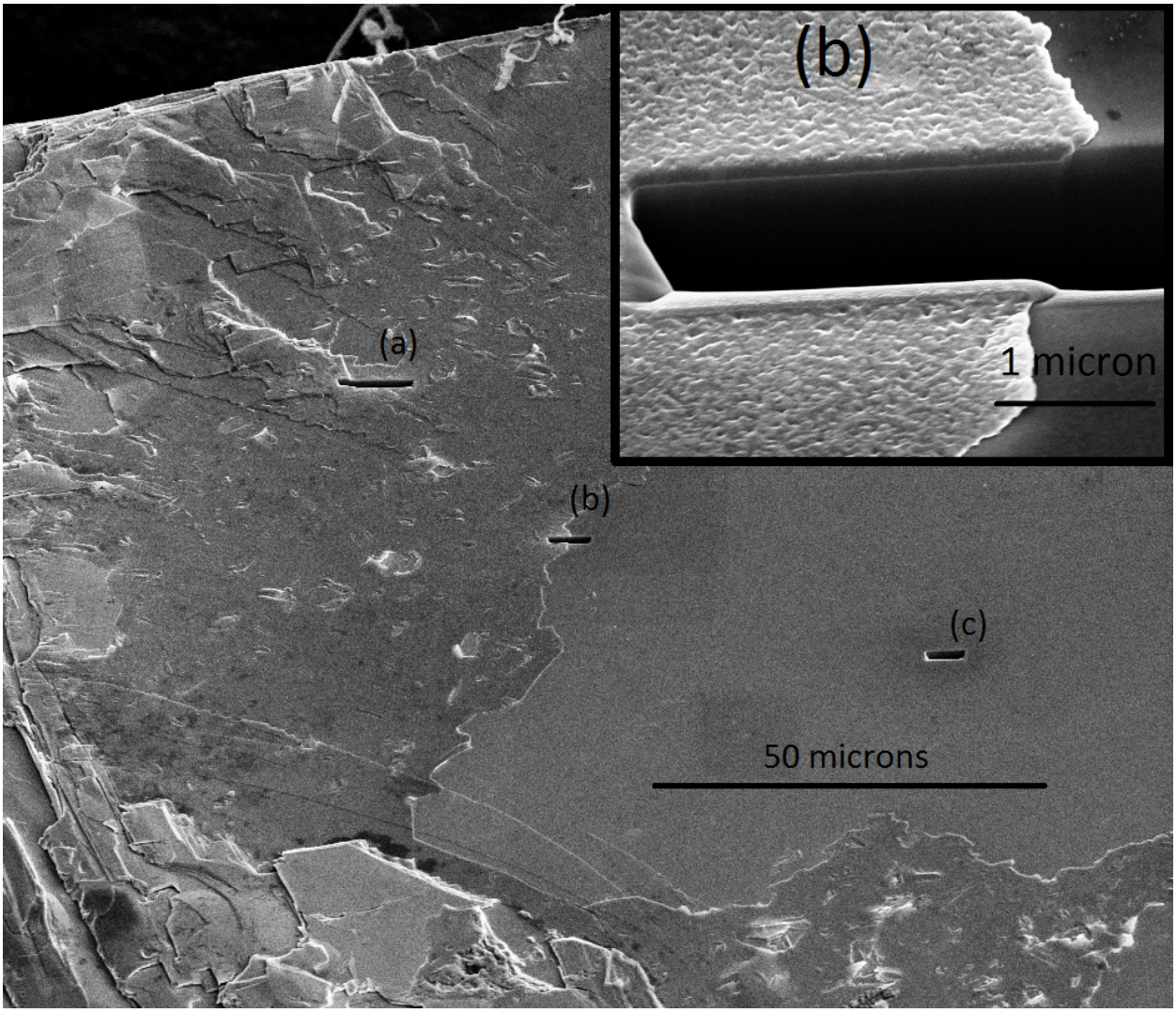

Figure 5.13: SEM image of a sample with an anomalously small $\lambda_{ab}(0)$ as determined by the film coating method. Whole patches of coated Aluminum were found to be missing. Three FIB cross-sections established this beyond a doubt. (a) Normally coated region. (b) Boundary of gap. (c) Uncoated region. Inset: blowup of gap region boundary.

and L will be too small. Conversely if the sample is mistakenly enveloped in an insulating

layer that remains coated during the overall measurement, then the $\lambda_{FBS}(0)$ will be much too large. This is because the effective film thickness, τ in the difference signal between when the sample does the screening and when the film does the screening, will effecively become larger. Given that τ is directly related to the final answer (in the limit where the B.V.P. can be simplified) and it is typically only 100nm, such an insulating layer does not have to be terribly thick to alter the overall result.

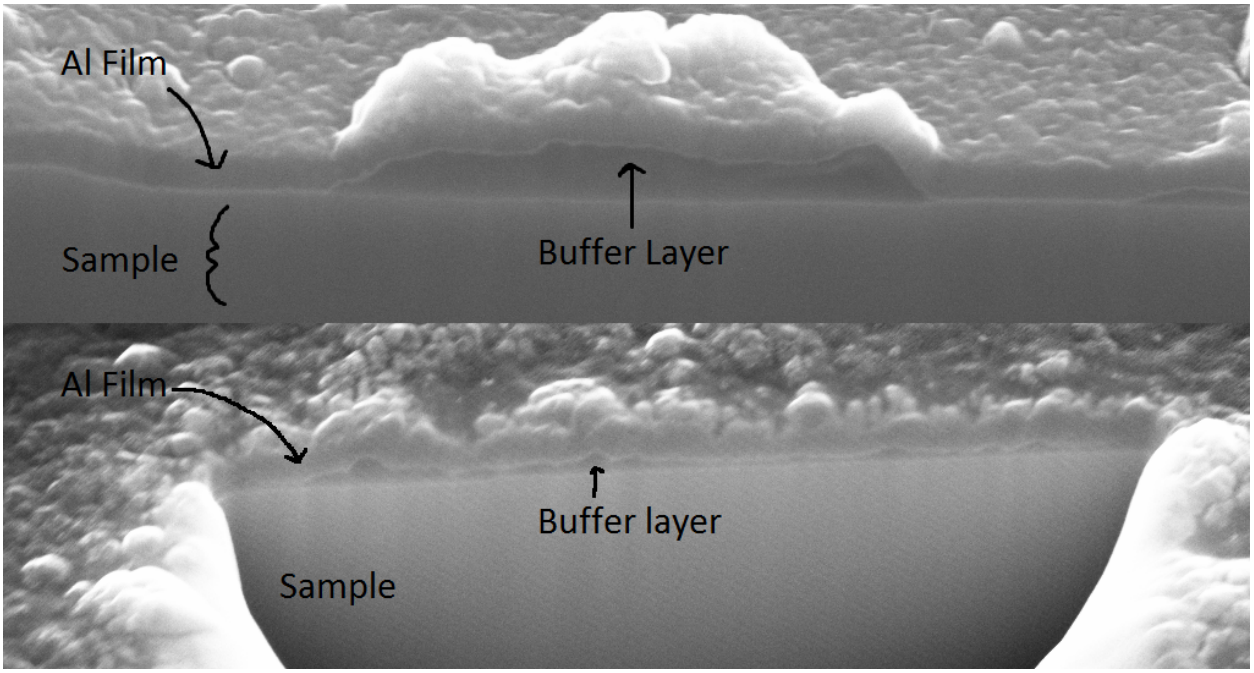

Figure 5.14: Two cross sections from a sample with an abnormally large penetration depth as reported by the film coating method. The irregular buffer layer in between the sample surface and the coated film is likely residual vacuum grease. Under high magnification it charged quite strongly and seemed to flow.

The hypothesis that such issues might be due to residual thermal contact grease was strengthened by cross sections of another excluded sample with a very large $\lambda_{ab}(0)$ (figure 5.14). Careful microscopy of this sample revealed both a thin "buffer" between the film and the crystal and hollow domes in the film itself. The likelihood that the highly viscosity glue used for wire bonding could spread and uniformly wet a crystal surface prior to mounting is low. It seems more likely that the weakly soluble silicon vacuum grease used in prior measurements was simply never fully washed away from some of the samples during the

extended cleaning process used before coating. Such problems have not recurred since Silicon grease was replaced by Apiezon-N, a hydrocarbon based (and therefore easily dissolved in organic solvents) high vacuum grease, for thermal contact. Another problem discovered in

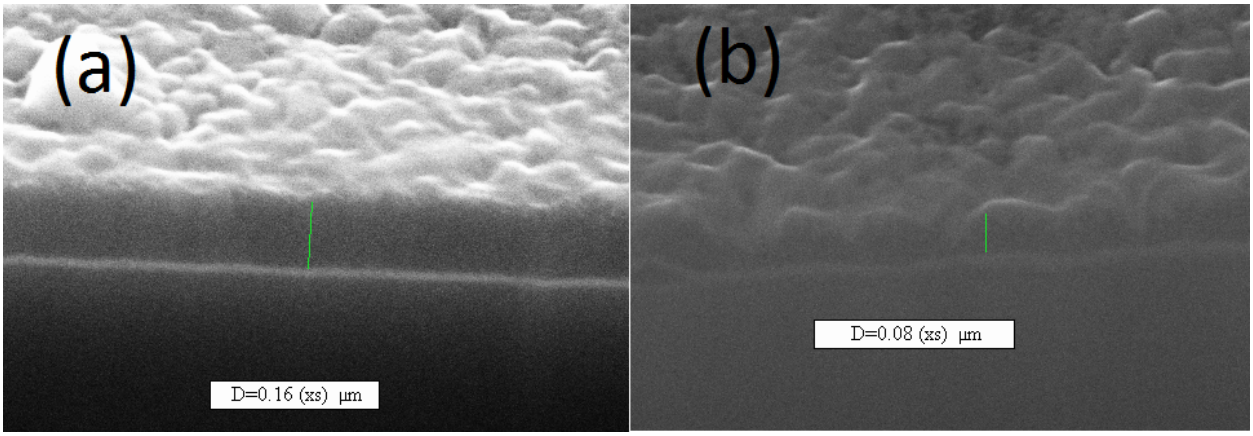

Figure 5.15: Opposite sides a and b of a sample with moderate devation in film thickness. Note the nearly factor of two difference in film coating.

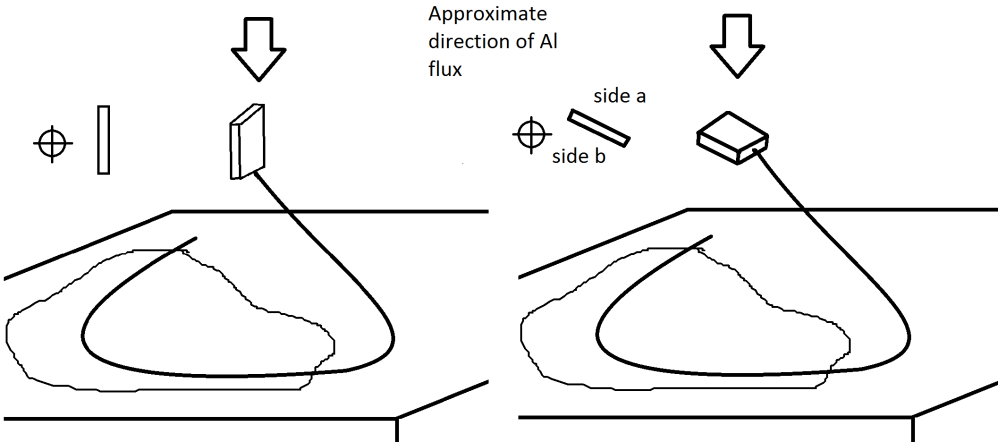

Figure 5.16: Left: A well mounted sample whose c-axis is roughly perpendicular to the principal direction of aluminum flux. Right: A poorly mounted sample where the c-axis is closer to parallel with the principal direction of Aluminum flux.

one of the coated samples was a discrepancy of the measured film thickness between opposite a-b surfaces of the thin plate-like sample (figure 5.15). This was attributed to the unbalanced way in which that crystal was mounted during coating (figure 5.16). While sputtering can generate particularly isotropic and uniform coatings even over irregular surfaces, as was

demonstrated in the previous section, it is not completely fool proof. It seems that the backside of the sample in this case received a substantially reduced aluminum flux.

Unfortunately, there is no clear way that such film issues can be identified without post measurement FIB cross-sectioning of each sample. Fortunately stricter tolerances for the maximum allowable deviation of a samples long axis from perpendicularity has prevented the recurrence of this issue.

5.5 Discussion:

The increase in $\lambda_{ab}(0)$ on the underdoped side (below $x \approx 0.047$), which is where data from many techniques such as NMR [29] suggest that intinerant antiferromagnetism and superconductivity coexist, implies that the Fermi surface has been reduced or partially gapped out. Because the carrier concentration n_s is proportional to $1/\lambda_{ab}^2(0)$, a large penetration depth implies that very few carriers are available to screen an external magnetic field. The carrier concentration, like most electrical properties, is simply a function of the avaiable Fermi surface, as was described in chapter 1.

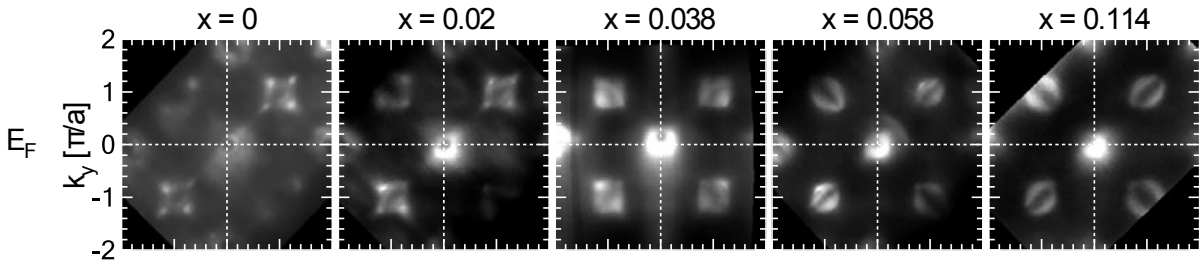

Figure 5.17: ARPES Fermi surface maps at 20K as the doping is varied from x = 0 (antiferromagnetic parent compound) to x = 0.114 (paramagnetic highly doped state) [13]. At this temperature superconductivty does not turn on until x = 0.058, at which point the last remnant of the petal shaped ordering in the parent compound vanishes.

There is evidence from ARPES measurements that the Fermi surface in $Ba(Fe_{1-x}Co_x)_2As_2$ undergoes severe changes as the cobalt doping is reduced (electrons are removed) [13]. What they observed was the replacment of the quasi-circular electron-like bands present at the M

points at high cobalt doping levels (x ¿ 0.058 in figure 5.17) with petal like hole-pockets as they passed below the critical cobalt level needed to sustain superconductivity (x ¡ 0.04 in figure 5.17). This restructuring of part of the Fermi surface and hence substantial reduction in carrier density for low dopings results in the spike in penetration depth we observed.

Fernandes and Schmalian demonstrated that the superfluid density in a magnetically ordered superconductor contains contributions from both the remaining Fermi surface after such reconstruction and the spin-density wave ordering (although the total SFD is still less after reconstructuion) [93]. They concluded that a superconductor where such competing orders coexisted would see an altered superfluid density (where Δ_{SC} is the superconducting gap and Δ_{AFM} is the antiferromagnetic gap):

$$\lambda^{-2} = \lambda_0^{-2} \frac{\Delta_{SC}^2}{\Delta_{AFM}^2 + \Delta_{SC}^2} \tag{5.2}$$

which can be restated as:

$$\lambda_{ab}^{SC+SDW}(0) = \lambda_{ab}^{SC}(0) \sqrt{1 + \frac{\Delta_{AFM}^2}{\Delta_{SC}^2}} \tag{5.3}$$

Interpolating between the gap in parent compound $\Delta_{AFM}(x = 0) \approx 60meV$ [9] and $\Delta_{AFM}(x = 0.05) = 0$, we can plot this expected boost in penetration depth as a function of composition. This is represented as three dashed lines in figure 5.11, where each different dashed line assumes a different $\lambda_{ab}^{SC}(0)$ value of either 120 nm, 180 nm, or 270 nm. It should be noted that this has ignored the variation of the gap value with doping, but that is actually consistent with data from MFM and SSM measurements, which saw the gap fluctuate by no more than 10% across the dome [12].

This theory does not take into account any of the physics in the overdoped region, so those dashed lines are kept horizontal. It should be noted that the fit was substantially improved by the assumption that AFM ordering came to an end at a slightly lower doping level, x = 0.05, rather than x = 0.06 as is conventionally assumed. But given the many simplifications

inherent in the model and the scatter in measured values, the level of agreement is quite good. In a related work the same authors (Fernandes and Schmalian) show that local coexistence cannot occur for a s_{++} pairing symmetry, but can for an s_{+-} one [94], so the agreement between their predictions and our data represents an indirect test of the pairing symmetry as well.

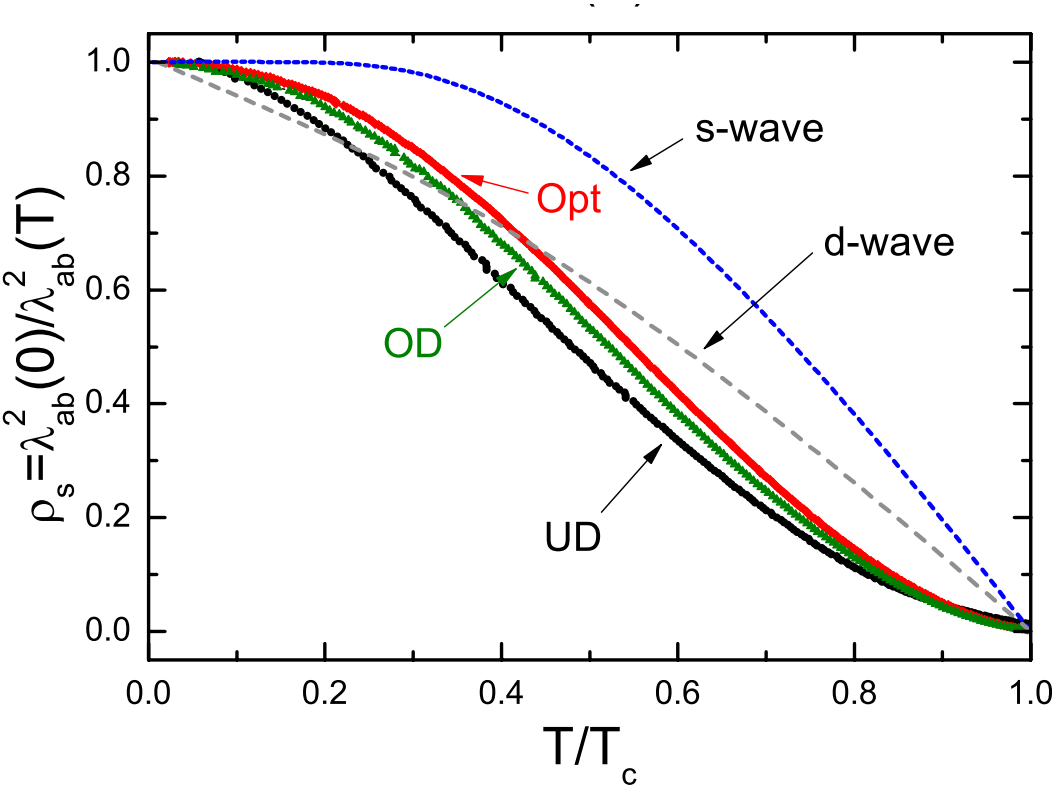

Figure 5.18: The normalized superfluid density, $\rho_s(T)$ for three different dopings Opt.: x = 0.074, OD: x = 0.102, UD: x = 0.038. The standard curves for s-wave and d-wave gaps are also shown [11].

Measurement of the $\lambda_{ab}(0)$ also allows us to calculate the normalized superfluid density versus temperature for a variety of different compositions (figure 5.18). Also shown in figure 5.18 are $\rho_s(T) = 1/(1 + \Delta\lambda(T)/\lambda_L(0))^2$ curves for a single band s-wave superconductor (dotted blue line) and a clean d-wave superconductor (dotted gray line). The superfluid densities for the different dopings plotted do not match well with either conventional s-wave superconductivity or d-wave superconductivity. An especially important feature present in

the data is the upward opening curvature of the superfluid density near T_C. This means that the superconducting gap evolves more slowly than it does for a single s-wave gap system, which implies two-gap superconductivity [95].

Also notable is that the superfluid density in the optimally doped sample is larger over the entire temperature range than that of both the underdoped and overdoped samples, though the difference is within the expected margin of error between the between the optimally doped sample and overdoped sample. That the superfluid density seems to veer more towards that of a conventional s-wave gap system at optimal doping (it becomes flatter at lower temperatures and loses some of its upward opening curvature at high temperatures) suggests that the imbalance between the gaps is reduced at the highest T_C and that deviations away from the optimal level produce higher levels of anisotropy. This is in keeping with the results of a variety of different measurements [5, 63, 96, 97].

5.6 Conclusion:

Given the gapping out of part of the Fermi surface in $Ba(Fe_{1-x}Co_x)_2As_2$ as the SDW AFM phase re-emerges below x = 0.047, it is perhaps not so surprising that our data displays the strong doping dependence that we observed. While it is true that those other measurements had established that there is no clear phase separation they did not actually guarantee that each separate order actually drew from the same pool shared of conduction electrons. This has never previously been observed in a superconductor before.

By demonstrating that as the antiferromagnetic order is suppressed, the superfluid carrier density increases until the maximal T_C, we lend weight to the argument that High T_C superconductivity is a sort of "Goldilocks" phenomenon [80], in that a system must have a balance between the strength of its interations and the degree of its itinerancy that is "just right". Strong interactions between the constituent fermions allow for considerable energy savings, but if they become too strong, they risk driving the system towards localization and

prevent the fermions from moving.

Our evidence that electrons involved in the superconducting state are sourced from the same resevoir as those used by the antiferromagnetic state also amounts to an indirect test of the pairing symmetry, provided that other measurements have of course ruled out d-wave ordering. This is a very exciting point, because there are very few methods that can discrimintate between multigap s_{++} ordering and unconvention s_{+-} ordering, especially in a disorder dominated system like the cobalt-122s.

Chapter 6

Quantum Criticality in $BaFe_2(As_{1-x}P_x)_2$:

6.1 Introduction:

Isovalent doping suppresses antiferromagnetism in the parent compound $BaFe_2As_2$ and brings on the superconducting state but does not change the population of electrons and holes, nor add significant scattering [14,23]. The action of the phosphorous dopant seems to be the simple compression of the Fe-As sublattice because Phosphorous atoms are slightly smaller than the arsenic atoms they replace. Similar effects have been seen by application of pressure to the parent compound.

The $BaFe_2(As_{1-x}P_x)_2$ phase diagram (figure 6.1) resembles that of the cobalt-122 materials and indeed reaches a comparable high transition temperature of 28 K at optimal doping. In contrast with the other 122 materials, phosphorous-122s were quickly established to have a nodal order parameter [98,99]. These similarities and differences make investigation of the phosphorous compounds very exciting.

6.1.1 Anomalous Normal State Properties of $BaFe_2(As_{1-x}P_x)_2$:

Transport measurements [14] on $BaFe_2(As_{1-x}P_x)_2$ crystals have established that the resistivity trends toward linear temperature dependence as the effective doping level decreases (figure 6.3 [14]). Similar effects have been seen in cobalt-122 single crystals, but the effects are substantially more difficult to interpret because those samples are not hole-electron compensated [100,101]. NMR measurements of the spin-lattice relaxation rate have shown that

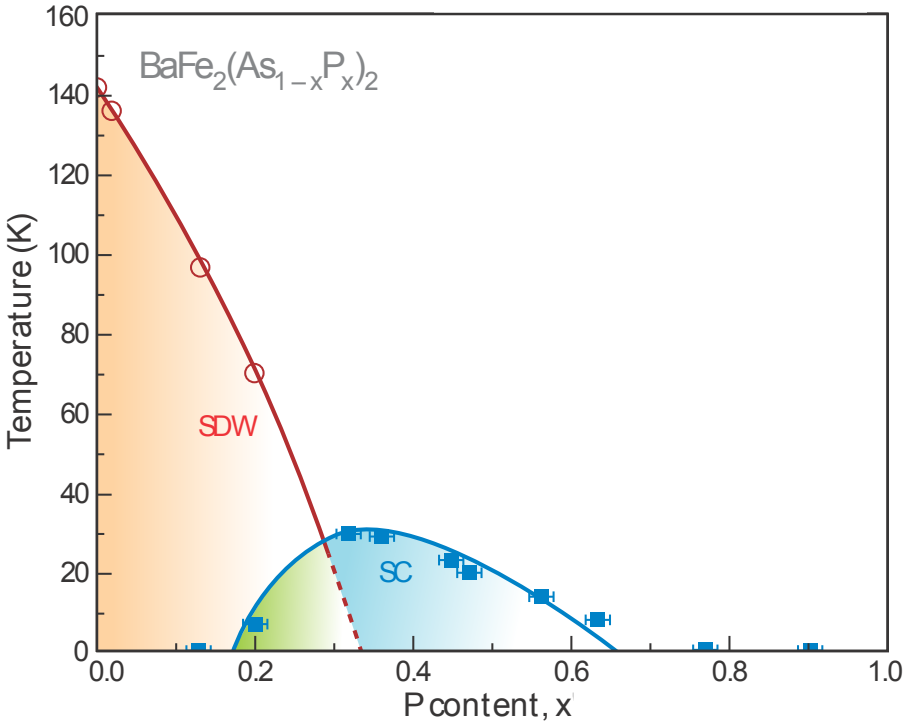

Figure 6.1: Phase diagram for $BaFe_2(As_{1-x}P_x)_2$ [1].

for high levels of phosphorous doping the Korringa relation $T_1TK^2 = constant$, where T_1 is the nuclear spin-lattice relaxation time and K is the Knight shift, remains true. But as the doping level is decreased substantial temperature dependence emerges, which has been attributed to the presence of dramatically enhanced AFM fluctuations since deviations from the Korringa law are usually caused by the presence of collective electron-electron interactions, like spin fluctuations (figure 6.3 [15]).

Measurements of the De Haas-van Alphen effect in phosphorous-122 crystals over a very large doping range confirmed that the doping process adds minimal chemical disorder to the host crystal, because only exceptionally clean materials will display such an effect [14]. Extraction of the Fermi surface from those oscillations demonstrated that the material remains a compensated metal over the full range of phosphorous doping. In fact the sizes of the electron and hole pockets simply shrink in a linear fashion as the phosphorous composition is reduced (figure 6.4). This is completely unexpected from what band theory models would

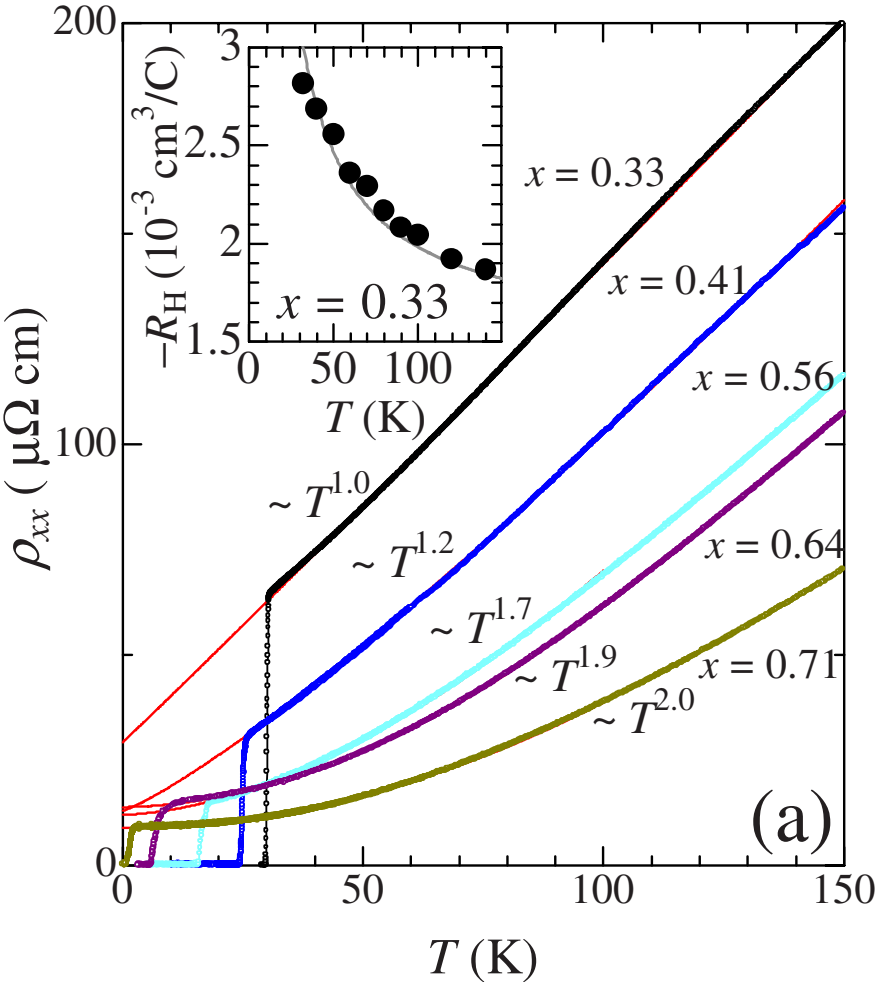

Figure 6.2: Normal-state $\rho_{xx}(T)$ for a variety of different dopings. As the phosphorous contet is reduced and the superconductor is tuned toward optimal doping the resistivity takes on a linear character. Such powerlaw analysis to the left of the dome peak is complicated by the emergence of SDW ordering at higher temperatures Inset: Effective powerlaw for normal-state resistivity as a function of doping [14].

predict and also contrasts sharply with the Fermi surface of the electron doped cobalt-122s which undergo a severe topological change as the doping level is changed (Chapter 3, [13]).

6.1.2 A Brief Primer on Quantum Criticality:

The substantial deviations of phosphorous-122 superconductors from the results predicted by Fermi liquid theory hint at something much greater, that there might in fact be a quantum

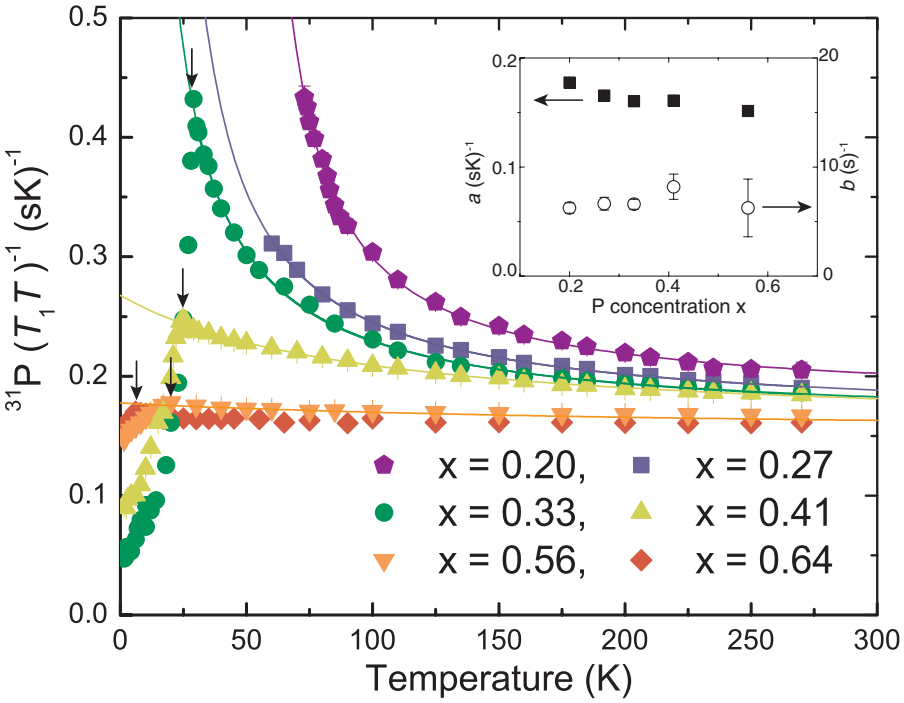

Figure 6.3: Temperature depedence of the spin lattice relaxation time for 31P nuclei for several different doping levels. Deviations from flattness represent violations of the Korringa law [15].

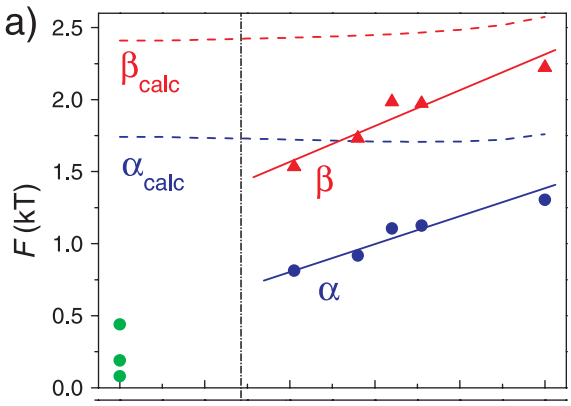

Figure 6.4: Average electron sheet frequencies obtained from quantum oscillations versus phosphorous doping level, x [14]. Doping seems to cause a only a linear variation in pocket size, which is totally contrary to what band theory would predict and indicative of the important role that many-body effects must play.

critical point (QCP) buried deep inside the superconducting dome as the consequence of a quantum phase transition (QPT) as the dopant concentration is varied [102]. Quantum criticality and quantum phase transitions are still very poorly understood, but are the focus

of many research efforts [16, 103].

Generically, a quantum phase transition is a qualitative change in the electronic ground state wavefunction of a many-body system in response to a smooth change in a coupling constant in its Hamiltonian. This transition takes place at zero temperature in the total absence of the thermal fluctuations that usually drive thermal phase transitions. Because it takes place at zero temperature, no change in entropy can occur between different phases and the process must be driven purely by quantum fluctuations associated with Heisenbergs uncertainty principle. By analogy with their more familiar thermal cousins, quantum phase transitions can be either abrupt first order process or continuous second order ones. There are significant disputes about the nature of first order transitions [104] and most references focus exclusively on the second order variety [105] so this brief commentary will not attempt to tack against that current.

In a second order process, the point of separation between the two phases is in fact a quantum critical point, where the ground state wave function will be a complicated superposition of an exponentially large number of wavefunctions describing the two separate quantum states on either side [16]. This is in fact a state of long range quantum entanglement the something like 10^{23} particles in a typical condensed matter system. This goes some distance toward explaining why our general level of insight in QPTs and QCPs is so minimal.

The problem becomes even more difficult when the effects of temperature are included; though it is widely believed that the effects of quantum criticality matter more at high temperature (up to some natural limit) than at low temperature. This paradoxical result is more palatable when one realizes that at low temperatures the time scale for thermal fluctuations increases dramatically while the quantum time scale (set by uncertainty principle fluctuations) remains unaffected. This separation in characteristic time scales means that the two different mechanism of fluctuations have little overlap and that the system can effectively be described by the ground state wavefunction. Well-defined quasiparticle excitations can

then be used to account for the thermal average of temperature dependent quantities.

As the temperature is increased however, the thermal time scale shortens and eventually becomes comparable to the time scale for quantum fluctuations. For itinerant electron systems in this region, their properties diverge remarkably from those expected of conventional Fermi liquids [2]. For instance in a two dimensional system the resistivity $\rho(T)$ goes from $T^2 \Rightarrow T$ and the normally temperature independent magnetic susceptibility χ and the electronic specific heat coefficient γ acquires strong temperature dependence and diverge as $T \Rightarrow 0$.

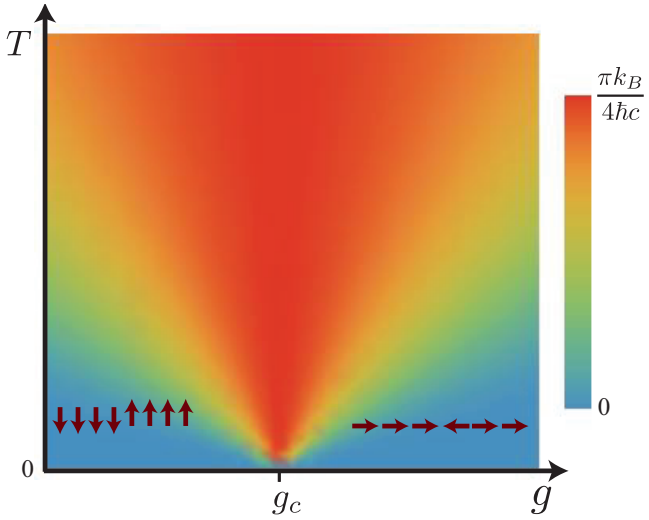

Figure 6.5: An exactly solvable Ising chain modelling quantum criticality in $CoNb_2O_6$. The effects of the QCP separating ferromagnetic configurations (left) from paramagnetic configurations (right) are seen to "funnel" up to very high temperatures [16].

This crossover in time scales yields a sort of funnel shaped region in the phase diagram rising up from zero temperature where the effects of the quantum phase transition are expected to most strongly felt (figure 6.5 [16]). Paradoxically, this thermal widening happens because thermal effects are stronger at larger T.

6.1.3 Quantum Criticality in Unconventional Superconductors:

The signature of quantum criticality seems to be written across the phase diagram of most unconventional superconductors. This same sort of crossover has also been seen in ruthenium oxides, organic metals, and heavy fermion systems [22, 106, 107]. Linear resistivity has also been seen in the Iron Pnictides and interpreted as a possible hint of a QCP, but this could arise from conventional Fermi liquid theory as the result of multiband effects and magnetic scattering [22].

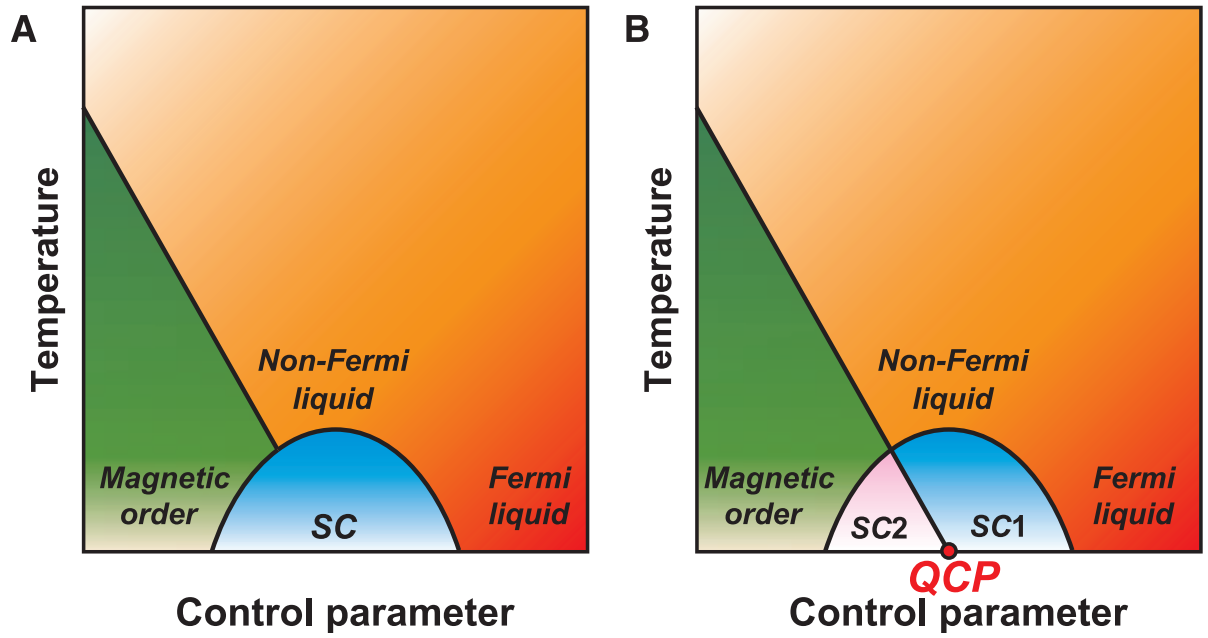

Figure 6.6: Two scenarios for the incorporation of a quantum critical point into a generic high temperature superconductor. In A superconductivity arises to screen the existence of a QCP. In B the quantum fluctuations from the critical point actually enhance superconductivity. It should be noted that some combination of the two scenarios can also be imagined [2].

If quantum critical points are so common in high temperature superconductivity, it is natural to ask why. There are two scenarios (figure 6.6) that are usually considered the most likely answers to that question [2]. In the first possibility, the extra quantum fluctuations add to the normal state throughout the funnel shaped region and boost the total energy of that state. A subsequent transition to a superconducting state as the temperature is lowered would gap out those excitations and lower the total free energy of the material. Because of

the energy boost from the fluctuations, such a transition temperature could then occur at a higher temperature than would otherwise be possible.

The second scenario posits that the quantum fluctuations in the critical region actually enhance the coupling process responsible for the Cooper pairing in the superconducting state and cause it turn on before it otherwise thermodynamically would. This is quite comparable to the T_C enhancement experienced by materials undergoing a structural transition that involves phonon softening [2]. The presence of a QCP would then imply that the superconducting state is actually split into two different types of superconductivity within the actual dome itself.

Distinguishing between those different possibilities requires measurements capable of tracking differences between the superconducting ground states of crystals with different dopings. Resistivity measurements cannot distinguish between different superconducting states without the application of large magnetic fields to suppress superconductivity (greater than 50T in the Iron Pncitides [2]). Such large fields have the potential to shift the position of the QCP or in fact induce a different form of quantum criticality [108]. Most of the signal in specific heat measurements occur near the transition temperature, so it may be rather insensitive to the location of the QCP, especially in high T_C materials where the zero temperature limit is rather far removed from this point [16].

The London penetration depth does track the properties of the superconducting state at low temperature and in zero field however. Recalling earlier chapters, $\lambda_L^{-2} = \mu_0 e_i^2 n_i / m_i^*$. Here n_i is the concentration of superconducting carriers in band i and m_i^* is their effective mass. While Leggett theorem [109] holds that the effective electron mass will not be affected by electron-electron interactions, some recent theoretical work has suggested that this result may be weakened for multiband systems [110].

The fortunate fact that quantum oscillations are possible in phosphorous-122‘s means that any changes in the carrier density n_i as function of doping can be tracked through their effect on the Fermi surface, provided of course that the quantities can be assumed to be

related. That it remains a compensated metal , with only slight linear-in-doping variations in both the hole and electron pocket sizes, mean that nothing severe can be happening to the super-current carrier density throughout the superconducting dome.

There is also a line of reasoning [111] that suggests that nodal superconductors may in fact make the symptoms of quantum criticality much more obvious. This consilience of properties in the phosphorous-122's: ultra clean samples that make quantum oscillations possible, nodal pairing interactions, and strong evidence for non-Fermi liquid behavior in the normal state, make it a natural test bed for the effects of quantum criticality.

6.2 Experimental Methods and Results:

6.2.1 Temperature Dependence of the Penetration Depth:

Measurements of the temperature dependent change in penetration depth $\Delta\lambda_{ab}(T)$ as a function of doping were performed using the tunnel diode oscillator technique as described in chapter 2. The work spanned three separate but functionally equivalent systems at UIUC, Ames and Kyoto University. The penetration depth of a sample measured at UIUC is plotted in figure 6.7. The low temperature behavior is displayed in figure 6.11.

The low temperature penetration depth for crystals of several different dopings spread across the superconducting dome are plotting figure 6.8. The powerlaw dependence of the low temperature penetration depth shows no significant change over the full range of doping spanned by the measurements. This quasi-linear powerlaw obtained for these measurements is quite consistent with all powerlaws obtained in earlier studies [98] and reflective of the nodal order parameter thought to be dominant in these materials. That the powerlaw does not vary over the full doping range suggests that the nodes must be located on the electron sheets of the fermi surface, given that earlier de Haas-van Alphen measurements have indicated that the hole pockets vary substantially with doping.

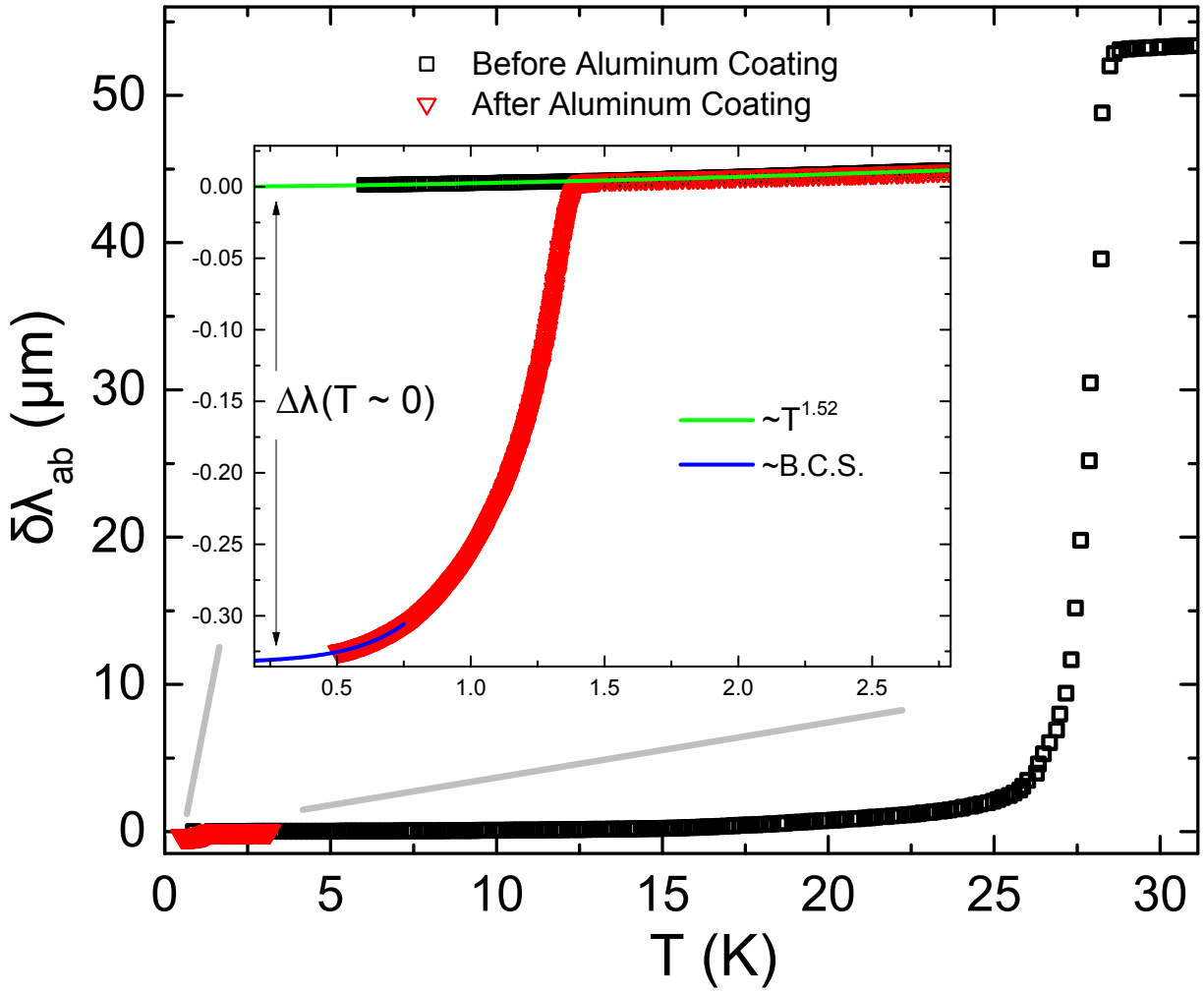

Figure 6.7: The temperature dependent penetration depth over the temperature range before (black squares) and after coating (red triangles). Inset: Blowup of the low temperature change in penetration depth and the superconducting transition in the thin aluminum film that was sputtered over the crystal. The extrapolated quantity $\Delta\lambda(T \Rightarrow 0)$ is used to calculate $\lambda_L(0)$.

6.2.2 Absolute Value of the Penetration Depth:

Measurements of the absolute penetration depth were performed using the aluminum coating method described in the previous chapter 5 and the analysis method from chapter 2. The lessons learned from the failure modes of the coating process on the cobalt-122 samples dramatically improved the yield rate of the coating process. In fact, only one sample was disqualified from the data set, because it detached from the mounting wire during the actual

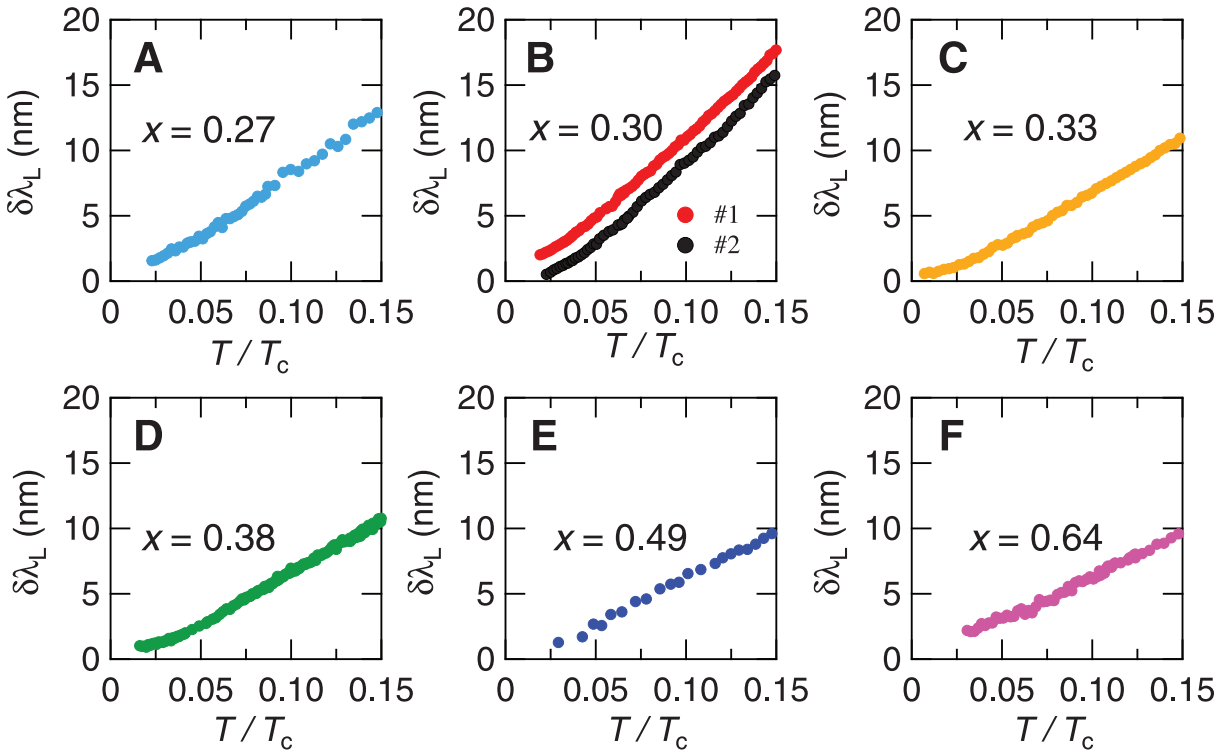

Figure 6.8: The low temperature portions of $\delta\lambda_{ab}(T)$ as a function of doping. No significant change in powerlaw was observed [17].

sputtering process.

Figure 6.10 displays the actual penetration depth measured as a function of the doping level for all of the measured doping values along with other measurements of the same quantity performed by collaborators at Kyoto University using a high frequency technique [17]. Their measurements function as a rather good cross check of the results from our aluminium coating process, because they utilize a very different cavity pertubation method. The high frequency of the cavity allows them to use the surface resistance $R_s = \sqrt{\mu_0\omega\rho_{dc}}$ as a ruler to measure the surface reactance ${}_s(T) = \mu_0\omega\lambda(T)$. The agreement between the results of their comparatively very different technique with our own tremendously strengthens our combined result.

The quasi-linear temperature variation observed in $\Delta\lambda(T)$ across all the measured doping levels (figure 6.8) can be used to extract another estimate of $\lambda_L(0)$. This is because in the

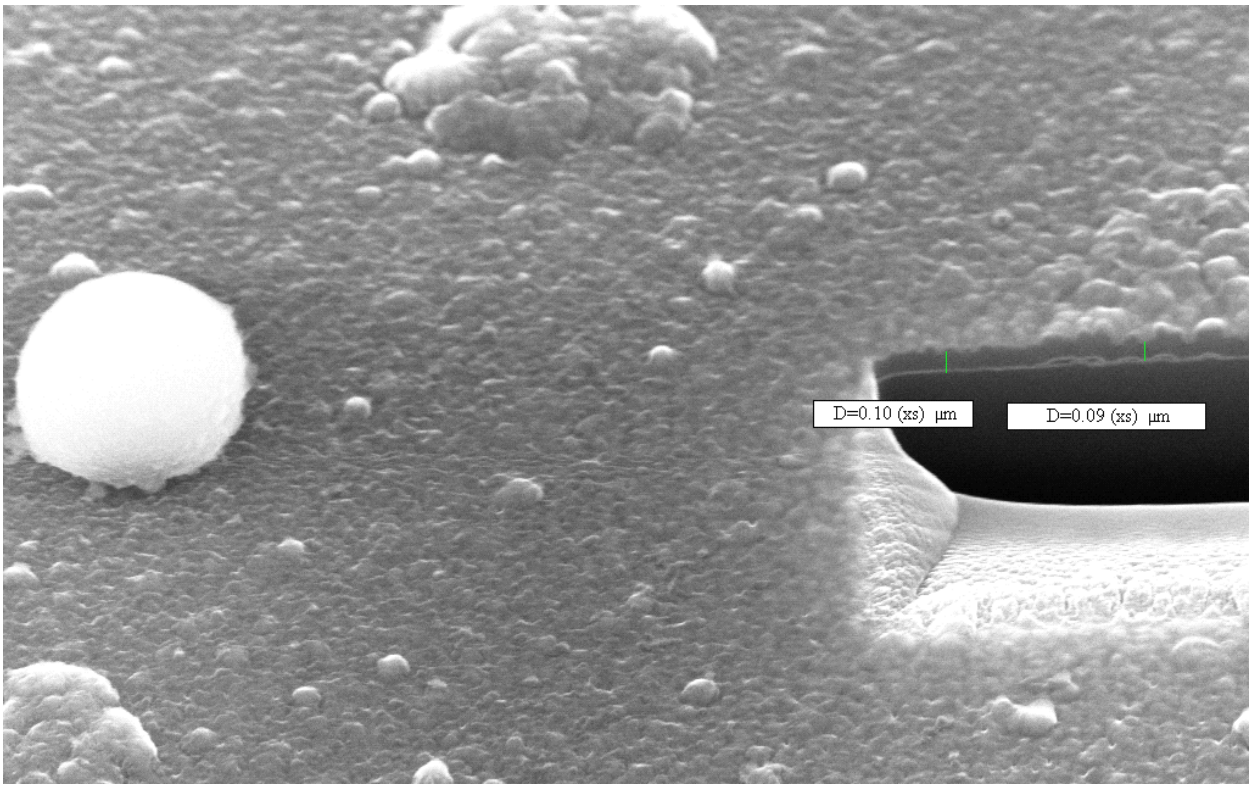

Figure 6.9: A FIB cross-section of one of the aluminum thin films deposited on the phosphorous-122 crystals. A latex sphere deposited from solution was used to double check SEM calibration (left of frame).

d-wave case it has been demonstrated that:

$$\frac{\delta\lambda_L(T)}{\lambda_L(0)} = \frac{ln(2)}{\Delta}k_BT \tag{6.1}$$

This means that the slope of $\delta\lambda_L(T)$ can be used to solve for $\lambda_L(T=0)$:

$$\frac{d}{dT}(\delta\lambda_L(T)) = \frac{ln(2)}{\Delta}k_BT\lambda_L(0) \tag{6.2}$$

This requires that some assumption be made about the magnitude of gap. Famously, in the s-wave case:

$$\frac{\Delta}{k_BT_C} = 1.76 \tag{6.3}$$

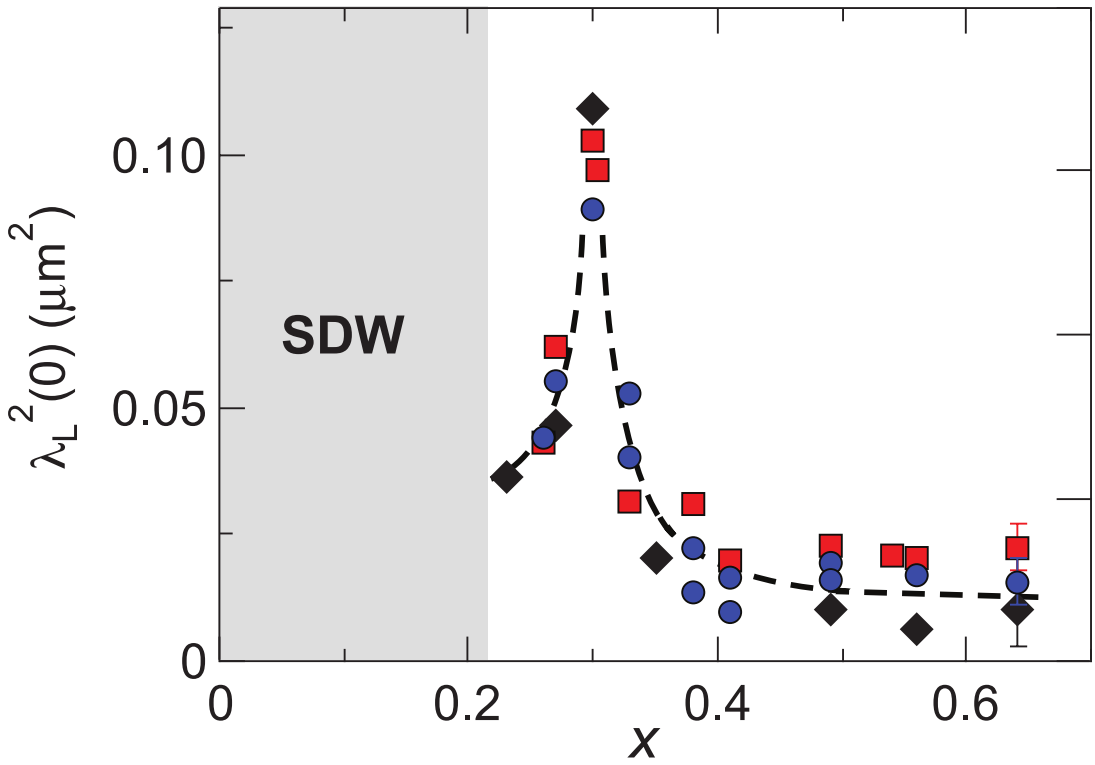

Figure 6.10: The absolute penetration depth squared $\lambda_L(0)^2$ as a function of doping x as measured using three different methods. Black Diamonds: TDR with aluminum coating. Red Squares: microwave cavity pertubation. Blue circles: low temperatue slope of $\delta\lambda(T)$ [17].

whereas in the d-wave case:

$$\frac{\Delta_{max}}{k_B T_C} = 2.14 \tag{6.4}$$

Together this would imply that:

$$\frac{1}{\lambda_L(T)^2} = (\frac{ln2}{nT_c}\frac{1}{\frac{d}{dT}(\delta\lambda_L(T))})^2 \tag{6.5}$$

The values obtained from this relationship are plotted in figure 6.10 as red squares and compare favorably with the results of both the aluminum coating results and those from microwave cavity results. In truth the relationship between low temperature slope and $\lambda_L(0)$ is substantially more complicated than what is portrayed in equation 6.5 and should involve substantially more detail about the local geometry of the near the nodes, the exact

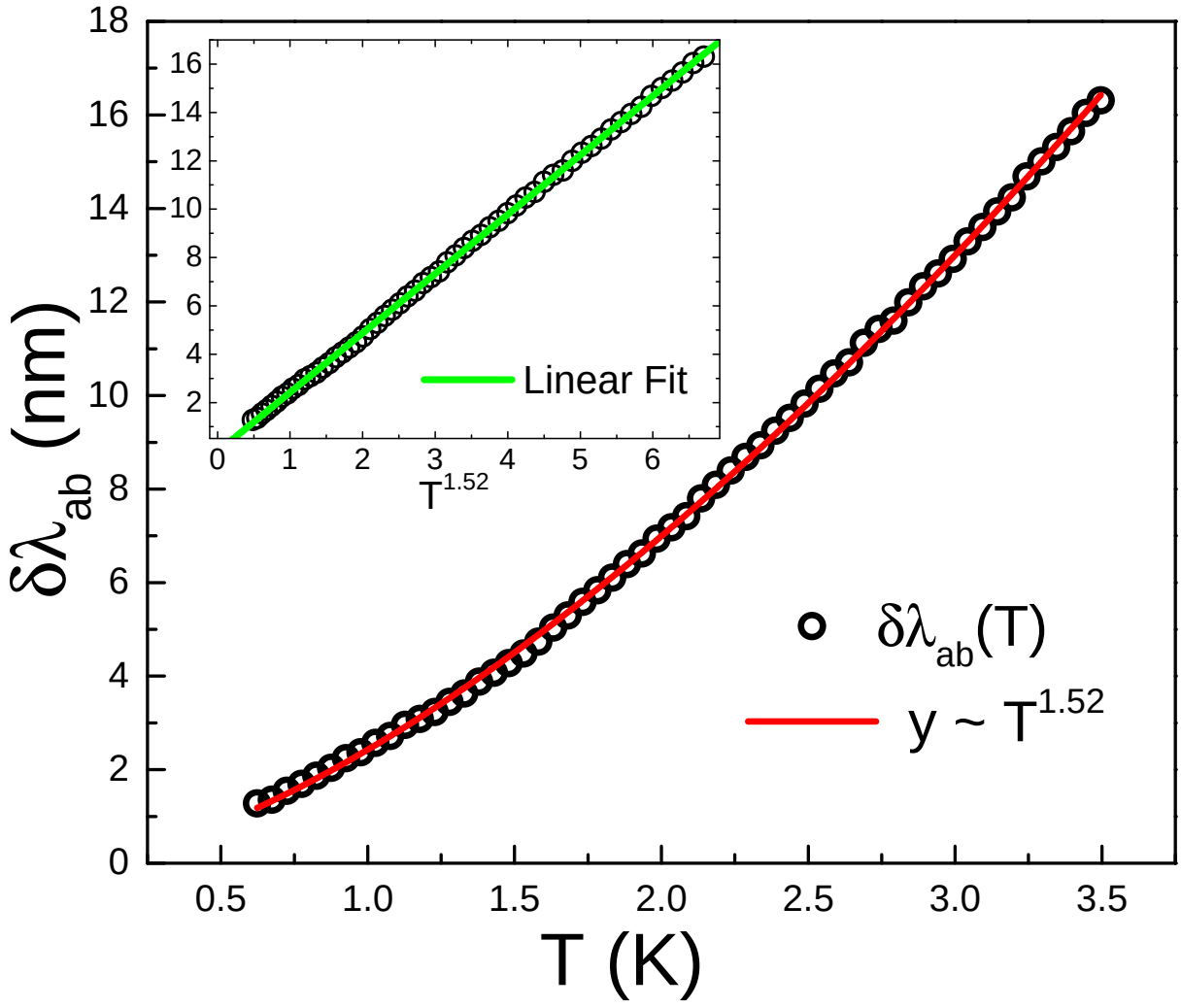

Figure 6.11: Black circles are the temperature dependent change in penetration depth below 10% of T_C for an optimally doped phosphorous-122 single crystal (x = 0.30). The red line is a powerlaw fit to the form αT^n. Inset: $\delta\lambda_{ab}(T)$ plotted versus $T^{1.52}$. The green line is a linear fit.

relationship between Δ and T_C, and other factors, but this simple model seems to succeed well enough. Certainly this would suggest that the nodal structure of the superconductor does not vary sharply with doping, even as it crosses the quantum critical point. Closer examination of the low temperature region (figure 6.11) also suggests that the data is not strictly linear and could be described by a combined T and T^2 state [47], or it could actually be trending to a $T^{1.5}$ at optimal doping [112].

6.3 Discussion:

The peak in penetration depth observed at optimal doping could be an artifact due to some kind of phase separation and lack decline in the superconducting volume fraction. Fortunately, no systematic effects suggestive of such a possibility were observed in either through the bulk susceptibility, heat capacity measurements, or through broadening of the resistive transition. This is point is strengthened by the remarkable agreement between three the rather different techniques used to determine $\lambda_L(0)$ by different groups in the collaboration.

It is also very interesting that the penetration depth seems to approach two different levels on either side of the peak at optimal doping. This is strongly suggestive that there is a phase transition in the superconducting state itself as the phosphorous level is varied. That the larger penetration phase occurs on the left side, where an SDW phase is thought to locally coexist with the superconducting state, just like in the cobalt-122s, is remarkable. This suggests that the two materials share the same physics if one posits that a peak in $\lambda_L(0)$ in cobalt crystals could be entirely smeared out by the strong scattering that predominates there.

The striking peak in $\lambda_L^2(0)$ at x =0.30 is most naturally attributable to the critical fluctuations related to the presence of a quantum critical point buried beneath the superconducting dome. That the superfluid density, $\rho_s \propto n_s/m^*$, is so minimized at this point means that either the carrier density has plummeted dramatically, or that the effective mass has risen. Quantum oscillations have shown that the carrier Fermi surfaces evolve smoothly and linearly with doping in phosphorous-122s unlike the Fermi surfaces in the cobalt-122s.

This leaves the possibility that Leggett theorem [109], which holds that multibody effects should not be able to renormalize the effective quasiparticle mass, is violated. More recent work has suggested that in multiband systems the assumptions used to protect the quasiparitlce mass from such renormalizations will actually break down and allow electron

correlation effects to hold sway [110]. It has also been suggested that the presences of nodes in the superconducting gap may be the primary location where quantum fluctuations can renormalize the effective Fermi velocity [112]. This model of nodal quantum criticality may be the source that the unusual $T^{3/2}$ powerlaw reported in the optimally doped phosphorous-122s (shown in figure 6.11), with the further implication that since the same powerlaw has been demonstrated in certain heavy fermion materials and organic superconductors, that they too might conceal quantum critical points within their phase diagrams.

6.4 Broader Implications for High-T_C Superconductivity and Conclusions:

That the highest transition temperature is obtained directly at the quantum critical point seems to suggest that quantum fluctuations actually cause superconductivity to happen at a higher temperature than it actually should. Had the role of the superconductivity been to "preserve modesty" and screen the existence of the QCP within the dome, we would expect to see no sharp variations of the penetration depth within the dome. The superfluid density seems to be reduced in the portion of the phase diagram where an SDW phase is widely believed to turn on, suggests that the QCP exists to separate the region of pure superconductivity on the right from the mixed state on the left where both phases compete for the same electrons [88].

It should also be noted that although many different high T_C materials exhibit the unusual normal state properties as the phosphorous-122's, no similar divergences in the susceptibility have ever been discovered in any of the iron pnictides [see last chapter], or in the heavy fermions [113], or in the cuprates [113, 114]. In fact in $Bi_2Sr_2CaCu_2O_{8+x}$ the superfluid density seems to reach a maximum at x = 0.2, meaning that $\lambda_L^2(0)$ reaches a minimum [113]. Some have the opinion that there actually be multiple quantum critical points within the superconducting dome of the cuprates, and that the whole situation might be vastly more

complicated [16].

References

[1] Hai-Hu Wen and Shiliang Li. Materials and novel superconductivity in iron pnictide superconductors. *Annu. Rev. Condens. Matter Phys.*, 2(1):121–140, 2011.

[2] T Shibauchi, A Carrington, and Y Matsuda. Quantum critical point lying beneath the superconducting dome in iron-pnictides. *arXiv preprint arXiv:1304.6387*, 2013.

[3] Andrey Chubukov. Pairing mechanism in fe-based superconductors. *Annu. Rev. Condens. Matter Phys.*, 3(1):57–92, 2012.

[4] Igor I Mazin. Superconductivity gets an iron boost. *Nature*, 464(7286):183–186, 2010.

[5] J.-Ph. Reid, M. A. Tanatar, X. G. Luo, H. Shakeripour, N. Doiron-Leyraud, N. Ni, S. L. Bud'ko, P. C. Canfield, R. Prozorov, and Louis Taillefer. Nodes in the gap structure of the iron arsenide superconductor $Ba(Fe_1\text{-}xCo_x)_2as_2$ from c-axis heat transport measurements. *Phys. Rev. B*, 82:064501, Aug 2010.

[6] D. V. Efremov, M. M. Korshunov, O. V. Dolgov, A. A. Golubov, and P. J. Hirschfeld. Disorder-induced transition between $s_\pm$ and s_{++} states in two-band superconductors. *Phys. Rev. B*, 84:180512, Nov 2011.

[7] L. Fang, Y. Jia, C. Chaparro, G. Sheet, H. Claus, M. A. Kirk, A. E. Koshelev, U. Welp, G. W. Crabtree, W. K. Kwok, S. Zhu, H. F. Hu, J. M. Zuo, H.-H. Wen, and B. Shen. High, magnetic field independent critical currents in (ba,k)fe[sub 2]as[sub 2] crystals. *Applied Physics Letters*, 101(1):012601, 2012.

[8] A Carrington. Quantum oscillation studies of the fermi surface of iron-pnictide superconductors. *Reports on Progress in Physics*, 74(12):124507, 2011.

[9] Takeshi Kondo, R. M. Fernandes, R. Khasanov, Chang Liu, A. D. Palczewski, Ni Ni, M. Shi, A. Bostwick, E. Rotenberg, J. Schmalian, S. L. Bud'ko, P. C. Canfield, and A. Kaminski. Unexpected fermi-surface nesting in the pnictide parent compounds $bafe_2as_2$ and $cafe_2as_2$ revealed by angle-resolved photoemission spectroscopy. *Phys. Rev. B*, 81:060507, Feb 2010.

[10] Michael R Norman et al. High-temperature superconductivity in the iron pnictides. *Physics*, 1:21, 2008.

[11] R. T. Gordon, H. Kim, N. Salovich, R. W. Giannetta, R. M. Fernandes, V. G. Kogan, T. Prozorov, S. L. Bud'ko, P. C. Canfield, M. A. Tanatar, and R. Prozorov. Doping evolution of the absolute value of the london penetration depth and superfluid density in single crystals of $Ba(Fe_1\text{-}xCo_x)_2as_2$. *Phys. Rev. B*, 82:054507, Aug 2010.

[12] Lan Luan, Thomas M. Lippman, Clifford W. Hicks, Julie A. Bert, Ophir M. Auslaender, Jiun-Haw Chu, James G. Analytis, Ian R. Fisher, and Kathryn A. Moler. Local measurement of the superfluid density in the pnictide superconductor $\mathrm{Ba(fe_{1-x}co_x)_2as_2}$ across the superconducting dome. *Phys. Rev. Lett.*, 106:067001, Feb 2011.

[13] Chang Liu, Takeshi Kondo, Rafael M Fernandes, Ari D Palczewski, Eun Deok Mun, Ni Ni, Alexander N Thaler, Aaron Bostwick, Eli Rotenberg, Jörg Schmalian, et al. Evidence for a lifshitz transition in electron-doped iron arsenic superconductors at the onset of superconductivity. *Nature Physics*, 6(6):419–423, 2010.

[14] H Shishido, AF Bangura, AI Coldea, S Tonegawa, K Hashimoto, S Kasahara, PMC Rourke, H Ikeda, T Terashima, R Settai, et al. Evolution of the fermi surface of bafe_ {2}(as_ {1-x} p_ {x}) _ {2} on entering the superconducting dome. *Physical review letters*, 104(5):057008, 2010.

[15] Y. Nakai, T. Iye, S. Kitagawa, K. Ishida, H. Ikeda, S. Kasahara, H. Shishido, T. Shibauchi, Y. Matsuda, and T. Terashima. Unconventional superconductivity and antiferromagnetic quantum critical behavior in the isovalent-doped $\mathrm{bafe_2(as_{1-x}p}_x)_2$. *Phys. Rev. Lett.*, 105:107003, Sep 2010.

[16] Subir Sachdev and Bernhard Keimer. Quantum criticality. *Physics Today*, 64:29, 2011.

[17] K Hashimoto, Kyuil Cho, T Shibauchi, S Kasahara, Y Mizukami, R Katsumata, Y Tsuruhara, T Terashima, H Ikeda, MA Tanatar, et al. A sharp peak of the zero-temperature penetration depth at optimal composition in bafe2 (as1–xpx) 2. *Science*, 336(6088):1554–1557, 2012.

[18] Yoichi Kamihara, Takumi Watanabe, Masahiro Hirano, and Hideo Hosono. Iron-based layered superconductor La[O1-xFx]FeAs (x=0.05-0.12) with T-c=26 K. *JOURNAL OF THE AMERICAN CHEMICAL SOCIETY*, 130(11):3296+, MAR 19 2008.

[19] GR Stewart. Superconductivity in iron compounds. *Reviews of Modern Physics*, 83(4):1589, 2011.

[20] Marianne Rotter, Marcus Tegel, and Dirk Johrendt. Superconductivity at 38 k in the iron arsenide (ba_ {1-x} k_ {x}) fe_ {2} as_ {2}. *Physical Review Letters*, 101(10):107006, 2008.

[21] Athena S Sefat, Rongying Jin, Michael A McGuire, Brian C Sales, David J Singh, and David Mandrus. Superconductivity at 22 k in co-doped bafe_ {2} as_ {2} crystals. *Physical review letters*, 101(11):117004, 2008.

[22] S Kasahara, T Shibauchi, K Hashimoto, K Ikada, S Tonegawa, R Okazaki, H Shishido, H Ikeda, H Takeya, K Hirata, et al. Evolution from non-fermi-to fermi-liquid transport via isovalent doping in bafe_ {2}(as_ {1- x} p_ {x}) _ {2} superconductors. *Physical Review B*, 81(18):184519, 2010.

[23] Cornelis J van der Beek, Marcin Konczykowski, Shigeru Kasahara, Takahito Terashima, Ryuji Okazaki, Takasada Shibauchi, and Yuji Matsuda. Quasiparticle scattering induced by charge doping of iron-pnictide superconductors probed by collective vortex pinning. *Physical review letters*, 105(26):267002, 2010.

[24] PJ Hirschfeld, MM Korshunov, and II Mazin. Gap symmetry and structure of fe-based superconductors. *Reports on Progress in Physics*, 74(12):124508, 2011.

[25] I. I. Mazin, D. J. Singh, M. D. Johannes, and M. H. Du. Unconventional superconductivity with a sign reversal in the order parameter of lafeaso$_{1-x}$f$_x$. *Phys. Rev. Lett.*, 101:057003, Jul 2008.

[26] II Mazin and J Schmalian. Pairing symmetry and pairing state in ferropnictides: Theoretical overview. *Physica C: Superconductivity*, 469(9):614–627, 2009.

[27] Hiroshi Kontani and Seiichiro Onari. Orbital-fluctuation-mediated superconductivity in iron pnictides: Analysis of the five-orbital hubbard-holstein model. *Phys. Rev. Lett.*, 104:157001, Apr 2010.

[28] Hiroshi Kontani, Tetsuro Saito, and Seiichiro Onari. Origin of orthorhombic transition, magnetic transition, and shear-modulus softening in iron pnictide superconductors: Analysis based on the orbital fluctuations theory. *Phys. Rev. B*, 84:024528, Jul 2011.

[29] M-H Julien, H Mayaffre, M Horvatić, C Berthier, XD Zhang, W Wu, GF Chen, NL Wang, and JL Luo. Homogeneous vs. inhomogeneous coexistence of magnetic order and superconductivity probed by nmr in co-and k-doped iron pnictides. *EPL (Europhysics Letters)*, 87(3):37001, 2009.

[30] Lillian Hoddeson, Gordon Baym, and Michael Eckert. The development of the quantum-mechanical electron theory of metals: 19281933. *Reviews of modern physics*, 59(1):287, 1987.

[31] D. Shoenberg. *Superconductvity*. Cambridge Monographs on Physics. Cambridge University Press, 1962.

[32] M. Tinkham. *Introduction to Superconductivity: Second Edition*. Dover Publications, Incorporated, 2012.

[33] DJ Scalapino. A common thread: The pairing interaction for unconventional superconductors. *Reviews of Modern Physics*, 84(4):1383, 2012.

[34] WN Hardy, DA Bonn, DC Morgan, Ruixing Liang, and Kuan Zhang. Precision measurements of the temperature dependence of λ in yba_ {2} cu_ {3} o_ {6.95}: Strong evidence for nodes in the gap function. *Physical Review Letters*, 70(25):3999, 1993.

[35] A. Carrington, F. Manzano, R. Prozorov, R. W. Giannetta, N. Kameda, and T. Tamegai. Evidence for surface andreev bound states in cuprate superconductors from penetration depth measurements. *Phys. Rev. Lett.*, 86:1074–1077, Feb 2001.

[36] R Prozorov, RW Giannetta, A Carrington, and FM Araujo-Moreira. Meissner-london state in superconductors of rectangular cross section in a perpendicular magnetic field. *Physical Review B*, 62(1):115, 2000.

[37] D Xu, SK Yip, and JA Sauls. Nonlinear meissner effect in unconventional superconductors. *Physical Review B*, 51(22):16233, 1995.

[38] Craig T Van Degrift. Tunnel diode oscillator for 0.001 ppm measurements at low temperatures. *Review of Scientific Instruments*, 46(5):599–607, 1975.

[39] Ruslan Prozorov and Russell W Giannetta. Magnetic penetration depth in unconventional superconductors. *Superconductor Science and Technology*, 19(8):R41, 2006.

[40] Kazuhiko Kuroki, Seiichiro Onari, Ryotaro Arita, Hidetomo Usui, Yukio Tanaka, Hiroshi Kontani, and Hideo Aoki. Unconventional pairing originating from the disconnected fermi surfaces of superconducting lafeaso$_{1-x}$f$_x$. *Phys. Rev. Lett.*, 101:087004, Aug 2008.

[41] P. J. Hirschfeld, M. M. Korshunov, and I. I. Mazin. Gap symmetry and structure of fe-based superconductors. *Reports on Progress in Physics*, 74(12):124508, 2011.

[42] R Prozorov and V G Kogan. London penetration depth in iron-based superconductors. *Reports on Progress in Physics*, 74(12):124505, 2011.

[43] Andrey Chubukov. Pairing mechanism in fe-based superconductors. *Annual Review of Condensed Matter Physics*, 3(1):57–92, 2012.

[44] J. Atkinson. Private communication.

[45] A. B. Vorontsov, M. G. Vavilov, and A. V. Chubukov. Superfluid density and penetration depth in the iron pnictides. *Phys. Rev. B*, 79:140507, Apr 2009.

[46] Yunkyu Bang. Superfluid density of the s-wave state for the iron-based superconductors. *EPL (Europhysics Letters)*, 86(4):47001, 2009.

[47] Peter J. Hirschfeld and Nigel Goldenfeld. Effect of strong scattering on the low-temperature penetration depth of a d -wave superconductor. *Phys. Rev. B*, 48:4219–4222, Aug 1993.

[48] Seiichiro Onari and Hiroshi Kontani. Violation of anderson's theorem for the sign-reversing s-wave state of iron-pnictide superconductors. *Phys. Rev. Lett.*, 103:177001, Oct 2009.

[49] Y. Wang, A. Kreisel, P. J. Hirschfeld, and V. Mishra. Using controlled disorder to distinguish $s_{\pm}$ and s_{++} gap structure in fe-based superconductors. *Phys. Rev. B*, 87:094504, Mar 2013.

[50] R. M. Fernandes, M. G. Vavilov, and A. V. Chubukov. Enhancement of T_c by disorder in underdoped iron pnictide superconductors. *Phys. Rev. B*, 85:140512, Apr 2012.

[51] J.-Ph. Reid, M. A. Tanatar, A. Juneau-Fecteau, R. T. Gordon, S. René de Cotret, N. Doiron-Leyraud, T. Saito, H. Fukazawa, Y. Kohori, K. Kihou, C. H. Lee, A. Iyo, H. Eisaki, R. Prozorov, and Louis Taillefer. Universal heat conduction in the iron arsenide superconductor $\mathrm{kfe_2as_2}$: Evidence of a d-wave state. *Phys. Rev. Lett.*, 109:087001, Aug 2012.

[52] K. Hashimoto, A. Serafin, S. Tonegawa, R. Katsumata, R. Okazaki, T. Saito, H. Fukazawa, Y. Kohori, K. Kihou, C. H. Lee, A. Iyo, H. Eisaki, H. Ikeda, Y. Matsuda, A. Carrington, and T. Shibauchi. Evidence for superconducting gap nodes in the zone-centered hole bands of kfe_2as_2 from magnetic penetration-depth measurements. *Phys. Rev. B*, 82:014526, Jul 2010.

[53] J-Ph Reid, A Juneau-Fecteau, R T Gordon, S Ren de Cotret, N Doiron-Leyraud, X G Luo, H Shakeripour, J Chang, M A Tanatar, H Kim, R Prozorov, T Saito, H Fukazawa, Y Kohori, K Kihou, C H Lee, A Iyo, H Eisaki, B Shen, H-H Wen, and Louis Taillefer. From d-wave to s-wave pairing in the iron-pnictide superconductor (ba,k)fe 2 as 2. *Superconductor Science and Technology*, 25(8):084013, 2012.

[54] Y. Nakajima, Y. Tsuchiya, T. Taen, T. Tamegai, S. Okayasu, and M. Sasase. Enhancement of critical current density in co-doped $bafe_2as_2$ with columnar defects introduced by heavy-ion irradiation. *Phys. Rev. B*, 80:012510, Jul 2009.

[55] H. Kim, R. T. Gordon, M. A. Tanatar, J. Hua, U. Welp, W. K. Kwok, N. Ni, S. L. Bud'ko, P. C. Canfield, A. B. Vorontsov, and R. Prozorov. London penetration depth in $Ba(Fe_1\text{-}xT_x)_2as_2$ ($t = Co,\ Ni$) superconductors irradiated with heavy ions. *Phys. Rev. B*, 82:060518, Aug 2010.

[56] Marianne Rotter, Marcus Tegel, and Dirk Johrendt. Superconductivity at 38 k in the iron arsenide $\mathrm{(ba_{1-x}k_x)fe_2as_2}$. *Phys. Rev. Lett.*, 101:107006, Sep 2008.

[57] Lei Shan, Yong-Lei Wang, Jing Gong, Bing Shen, Yan Huang, Huan Yang, Cong Ren, and Hai-Hu Wen. Evidence of multiple nodeless energy gaps in superconducting $\mathrm{ba_{0.6}k_{0.4}fe_2as_2}$ single crystals from scanning tunneling spectroscopy. *Phys. Rev. B*, 83:060510, Feb 2011.

[58] A. Charnukha, O. V. Dolgov, A. A. Golubov, Y. Matiks, D. L. Sun, C. T. Lin, B. Keimer, and A. V. Boris. Eliashberg approach to infrared anomalies induced by the superconducting state of $\mathrm{ba_{0.68}k_{0.32}fe_2as_2}$ single crystals. *Phys. Rev. B*, 84:174511, Nov 2011.

[59] A. A. Abrikosov and L. P. Gor'kov. *[Sov. Phys. JETP*, 12:1243, Sep 1961.

[60] V. G. Kogan. Pair breaking in iron pnictides. *Phys. Rev. B*, 80:214532, Dec 2009.

[61] A. A. Golubov and I. I. Mazin. Effect of magnetic and nonmagnetic impurities on highly anisotropic superconductivity. *Phys. Rev. B*, 55:15146–15152, Jun 1997.

[62] L.A. Openov. Combined effect of nonmagnetic and magnetic scatterers on the critical temperatures of superconductors with different anisotropies of the gap. *Journal of Experimental and Theoretical Physics Letters*, 66(10):661–667, 1997.

[63] M. A. Tanatar, J.-Ph. Reid, H. Shakeripour, X. G. Luo, N. Doiron-Leyraud, N. Ni, S. L. Bud'ko, P. C. Canfield, R. Prozorov, and Louis Taillefer. Doping dependence of heat transport in the iron-arsenide superconductor $\mathrm{Ba(fe_{1-x}co_x)_2as_2}$: From isotropic to a strongly k-dependent gap structure. *Phys. Rev. Lett.*, 104:067002, Feb 2010.

[64] C. Martin, H. Kim, R. T. Gordon, N. Ni, V. G. Kogan, S. L. Bud'ko, P. C. Canfield, M. A. Tanatar, and R. Prozorov. Evidence from anisotropic penetration depth for a three-dimensional nodal superconducting gap in single-crystalline $Ba(Fe_1\text{-}xNi_x)_2as_2$. *Phys. Rev. B*, 81:060505, Feb 2010.

[65] P. J. Hirschfeld. Private communication.

[66] K. Hashimoto, T. Shibauchi, S. Kasahara, K. Ikada, S. Tonegawa, T. Kato, R. Okazaki, C. J. van der Beek, M. Konczykowski, H. Takeya, K. Hirata, T. Terashima, and Y. Matsuda. Microwave surface-impedance measurements of the magnetic penetration depth in single crystal $\mathrm{ba_{1-x}\mathbf{k}_xfe_2as_2}$ superconductors: Evidence for a disorder-dependent superfluid density. *Phys. Rev. Lett.*, 102:207001, May 2009.

[67] H. Chen, Y. Ren, Y. Qiu, Wei Bao, R. H. Liu, G. Wu, T. Wu, Y. L. Xie, X. F. Wang, Q. Huang, and X. H. Chen. Coexistence of the spin-density wave and superconductivity in ba 1?x k x fe 2 as 2. *EPL (Europhysics Letters)*, 85(1):17006, 2009.

[68] Hideto Fukazawa, Takehiro Yamazaki, Kenji Kondo, Yoh Kohori, Nao Takeshita, Parasharam M. Shirage, Kunihiro Kihou, Kiichi Miyazawa, Hijiri Kito, Hiroshi Eisaki, and Akira Iyo. ^{75}as nmr study of hole-doped superconductor $\mathrm{ba_{1-x}k_xfe_2as_2}$ ($t_c \simeq 38\,\mathrm{k}$). *Journal of the Physical Society of Japan*, 78(3):033704, 2009.

[69] S. Avci, O. Chmaissem, D. Y. Chung, S. Rosenkranz, E. A. Goremychkin, J. P. Castellan, I. S. Todorov, J. A. Schlueter, H. Claus, A. Daoud-Aladine, D. D. Khalyavin, M. G. Kanatzidis, and R. Osborn. Phase diagram of $\mathrm{ba_1\text{-}xk_xfe_2as_2}$. *Phys. Rev. B*, 85:184507, May 2012.

[70] J. D. Fletcher, A. Carrington, O. J. Taylor, S. M. Kazakov, and J. Karpinski. Temperature-dependent anisotropy of the penetration depth and coherence length of $\mathrm{mgb_2}$. *Phys. Rev. Lett.*, 95:097005, Aug 2005.

[71] Noriko Chikumoto, Ayako Yamamoto, Marcin Konczykowski, and Masato Murakami. Magnetization behavior of mgb2 and the effect of high energy heavy-ion irradiation. *Physica C: Superconductivity*, 378381, Part 1(0):466 – 469, 2002.

[72] I. I. Mazin, O. K. Andersen, O. Jepsen, O. V. Dolgov, J. Kortus, A. A. Golubov, A. B. Kuz'menko, and D. van der Marel. Superconductivity in mgb_2: Clean or dirty? *Phys. Rev. Lett.*, 89:107002, Aug 2002.

[73] I.I. Mazin and V.P. Antropov. Electronic structure, electronphonon coupling, and multiband effects in mgb2. *Physica C: Superconductivity*, 385(12):49 – 65, 2003.

[74] RI Miller, RF Kiefl, JH Brewer, FD Callaghan, JE Sonier, R Liang, DA Bonn, and W Hardy. Coexistence of magnetism and superconductivity in ultraclean underdoped yba_ {2} cu_ {3} o_ {6.37}. *Physical Review B*, 73(14):144509, 2006.

[75] D. H. Ryan, J. M. Cadogan, C. Ritter, F. Canepa, A. Palenzona, and M. Putti. Coexistence of long-ranged magnetic order and superconductivity in the pnictide superconductor $smfeaso_1$-xf_x ($x = 0,\ 0.15$). *Phys. Rev. B*, 80:220503, Dec 2009.

[76] T. Park, F. Ronning, H. Q. Yuan, M. B. Salamon, R. Movshovich, J. L. Sarrao, and J. D. Thompson. Hidden magnetism and quantum criticality in the heavy fermion superconductor $CeRhIn_5$. , 440:65–68, March 2006.

[77] Shinji Kawasaki, Takeshi MIto, Yu Kawasaki, Hisashi Kotegawa, G-q Zheng, Yoshio Kitaoka, Hiroaki Shishido, Shingo Araki, Rikio Settai, and Yoshichika Onuki. New superconducting and magnetic phases emerge on the magnetic criticality in cein3. *Journal of the Physical Society of Japan*, 73:1647, 2004.

[78] S Kawasaki, T Mito, Y Kawasaki, G-q Zheng, Y Kitaoka, D Aoki, Y Haga, and Y Ōnuki. Gapless magnetic and quasiparticle excitations due to the coexistence of antiferromagnetism and superconductivity in cerhin_ {5}: A study of^ {115} in nqr under pressure. *Physical review letters*, 91(13):137001, 2003.

[79] T. Olheiser. Unpublished.

[80] DN Basov and Andrey V Chubukov. Manifesto for a higher tc. *Nature Physics*, 7(4):272–276, 2011.

[81] Jan Zaanen, Sudip Chakravarty, T Senthil, Philip Anderson, Patrick Lee, Jörg Schmalian, Masatoshi Imada, David Pines, Mohit Randeria, Chandra Varma, et al. Towards a complete theory of high tc. *Nature Physics*, 2(3):138–143, 2006.

[82] Sudip Chakravarty, RB Laughlin, Dirk K Morr, and Chetan Nayak. Hidden order in the cuprates. *Physical Review B*, 63(9):094503, 2001.

[83] Graham Collins. An iron key to high-temperature superconductivity? *Scientific American Magazine*, 301(2):62–69, 2009.

[84] Steven A Kivelson, Dung-Hai Lee, Eduardo Fradkin, and Vadim Oganesyan. Competing order in the mixed state of high-temperature superconductors. *Physical Review B*, 66(14):144516, 2002.

[85] Peter Thalmeier and Gertrud Zwicknagl. Unconventional superconductivity and magnetism in lanthanide and actinide intermetallic compounds. *Handbook on the physics and chemistry of rare earths*, 34:135–287, 2004.

[86] D. K. Pratt, W. Tian, A. Kreyssig, J. L. Zarestky, S. Nandi, N. Ni, S. L. Bud'ko, P. C. Canfield, A. I. Goldman, and R. J. McQueeney. Coexistence of competing antiferromagnetic and superconducting phases in the underdoped $Ba(fe_{0.953}co_{0.047})_2as_2$ compound using x-ray and neutron scattering techniques. *Phys. Rev. Lett.*, 103:087001, Aug 2009.

[87] Miaoyin Wang, Huiqian Luo, Meng Wang, Songxue Chi, Jose A Rodriguez-Rivera, Deepak Singh, Sung Chang, Jeffrey W Lynn, and Pengcheng Dai. Magnetic field effect on static antiferromagnetic order and spin excitations in the underdoped iron arsenide superconductor bafe_ {1.92} ni_ {0.08} as_ {2}. *Physical Review B*, 83(9):094516, 2011.

[88] Tetsuya Iye, Yusuke Nakai, Shunsaku Kitagawa, Kenji Ishida, Shigeru Kasahara, Takasada Shibauchi, Yuji Matsuda, and Takahito Terashima. Gradual suppression of antiferromagnetism in bafe_ {2}(as_ {1- x} p_ {x}) _ {2}: Zero-temperature evidence for a quantum critical point. *Physical Review B*, 85(18):184505, 2012.

[89] Tetsuya Iye, Yusuke Nakai, Shunsaku Kitagawa, Kenji Ishida, Shigeru Kasahara, Takasada Shibauchi, Yuji Matsuda, and Takahito Terashima. Microscopic evidence of direct coupling between magnetic and superconducting order parameters in bafe _2(as _{$1-x$} p _x) _2. *arXiv preprint arXiv:1111.7075*, 2011.

[90] Pengcheng Dai, Jiangping Hu, and Elbio Dagotto. Magnetism and its microscopic origin in iron-based high-temperature superconductors. *Nature Physics*, 8(10):709–718, 2012.

[91] G. R. Stewart. Superconductivity in iron compounds. *Rev. Mod. Phys.*, 83:1589–1652, Dec 2011.

[92] R Prozorov, RW Giannetta, A Carrington, P Fournier, RL Greene, P Guptasarma, DG Hinks, and AR Banks. Measurements of the absolute value of the penetration depth in high-¡ equation¿ t¡ sub¿ c¡/sub¿¡/equation¿ superconductors using a low-¡ equation¿ t¡ sub¿ c¡/sub¿¡/equation¿ superconductive coating. *Applied Physics Letters*, 77(25):4202–4204, 2000.

[93] Rafael M. Fernandes and Jörg Schmalian. Transfer of optical spectral weight in magnetically ordered superconductors. *Phys. Rev. B*, 82:014520, Jul 2010.

[94] Rafael M. Fernandes, Daniel K. Pratt, Wei Tian, Jerel Zarestky, Andreas Kreyssig, Shibabrata Nandi, Min Gyu Kim, Alex Thaler, Ni Ni, Paul C. Canfield, Robert J. McQueeney, Jörg Schmalian, and Alan I. Goldman. Unconventional pairing in the iron arsenide superconductors. *Phys. Rev. B*, 81:140501, Apr 2010.

[95] Ruslan Prozorov and Vladimir G Kogan. London penetration depth in iron-based superconductors. *Reports on Progress in Physics*, 74(12):124505, 2011.

[96] Sergey L. Bud'ko, Ni Ni, and Paul C. Canfield. Jump in specific heat at the superconducting transition temperature in $Ba(Fe_1\text{-}xCo_x)_2as_2$ and $Ba(Fe_1\text{-}xNi_x)_2as_2$ single crystals. *Phys. Rev. B*, 79:220516, Jun 2009.

[97] K. Gofryk, A. S. Sefat, M. A. McGuire, B. C. Sales, D. Mandrus, J. D. Thompson, E. D. Bauer, and F. Ronning. Doping-dependent specific heat study of the superconducting gap in $Ba(Fe_1\text{-}xCo_x)_2as_2$. *Phys. Rev. B*, 81:184518, May 2010.

[98] K Hashimoto, M Yamashita, S Kasahara, Y Senshu, N Nakata, S Tonegawa, K Ikada, A Serafin, A Carrington, T Terashima, et al. Line nodes in the energy gap of superconducting bafe_ {2}(as_ {1- x} p_ {x}) _ {2} single crystals as seen via penetration depth and thermal conductivity. *Physical Review B*, 81(22):220501, 2010.

[99] M Yamashita, Y Senshu, T Shibauchi, S Kasahara, K Hashimoto, D Watanabe, H Ikeda, T Terashima, I Vekhter, AB Vorontsov, et al. Nodal gap structure of superconducting bafe_ {2}(as_ {1- x} p_ {x}) _ {2} from angle-resolved thermal conductivity in a magnetic field. *Physical Review B*, 84(6):060507, 2011.

[100] Lei Fang, Huiqian Luo, Peng Cheng, Zhaosheng Wang, Ying Jia, Gang Mu, Bing Shen, II Mazin, Lei Shan, Cong Ren, et al. Roles of multiband effects and electron-hole asymmetry in the superconductivity and normal-state properties of ba (fe_ {1- x} co_ {x}) _ {2} as_ {2}. *Physical Review B*, 80(14):140508, 2009.

[101] F Rullier-Albenque, D Colson, A Forget, and H Alloul. Hall effect and resistivity study of the magnetic transition, carrier content, and fermi-liquid behavior in ba (fe_ {1-x} co_ {x}) _ {2} as_ {2}. *Physical review letters*, 103(5):057001, 2009.

[102] Jianhui Dai, Qimiao Si, Jian-Xin Zhu, and Elihu Abrahams. Iron pnictides as a new setting for quantum criticality. *Proceedings of the National Academy of Sciences*, 106(11):4118–4121, 2009.

[103] SL Sondhi, SM Girvin, JP Carini, and D Shahar. Continuous quantum phase transitions. *Reviews of Modern Physics*, 69(1):315, 1997.

[104] C Pfleiderer. Why first order quantum phase transitions are interesting. *Journal of Physics: Condensed Matter*, 17(11):S987, 2005.

[105] Subir Sachdev. *Quantum phase transitions*. Wiley Online Library, 2007.

[106] SA Grigera, RS Perry, AJ Schofield, M Chiao, SR Julian, GG Lonzarich, SI Ikeda, Y Maeno, AJ Millis, and AP Mackenzie. Magnetic field-tuned quantum criticality in the metallic ruthenate sr3ru2o7. *Science*, 294(5541):329–332, 2001.

[107] Nicolas Doiron-Leyraud, Pascale Auban-Senzier, Samuel René de Cotret, Claude Bourbonnais, Denis Jérome, Klaus Bechgaard, and Louis Taillefer. Correlation between linear resistivity and t_ {c} in the bechgaard salts and the pnictide superconductor ba (fe_ {1- x} co_ {x}) _ {2} as_ {2}. *Physical Review B*, 80(21):214531, 2009.

[108] Sung-Sik Lee. Low-energy effective theory of fermi surface coupled with u(1) gauge field in $2+1$ dimensions. *Phys. Rev. B*, 80:165102, Oct 2009.

[109] AJ Leggett. Theory of a superfluid fermi liquid. i. general formalism and static properties. *Physical Review*, 140(6A):A1869, 1965.

[110] A Levchenko, MG Vavilov, M Khodas, and AV Chubukov. Enhancement of the london penetration depth in pnictides at the onset of spin-density-wave order under superconducting dome. *Physical review letters*, 110(17):177003, 2013.

[111] Takuya Nomoto and Hiroaki Ikeda. Effect of magnetic criticality and fermi-surface topology on the magnetic penetration depth. *arXiv preprint arXiv:1305.4427*, 2013.

[112] Kenichiro Hashimoto, Yuta Mizukami, Ryo Katsumata, Hiroaki Shishido, Minoru Yamashita, Hiroaki Ikeda, Yuji Matsuda, John A Schlueter, Jonathan D Fletcher, Antony Carrington, et al. Anomalous superfluid density in quantum critical superconductors. *Proceedings of the National Academy of Sciences*, 110(9):3293–3297, 2013.

[113] JL Tallon, JW Loram, JR Cooper, Christos Panagopoulos, and Christian Bernhard. Superfluid density in cuprate high-t_ {c} superconductors: A new paradigm. *Physical Review B*, 68(18):180501, 2003.

[114] Subir Sachdev. Where is the quantum critical point in the cuprate superconductors? *physica status solidi (b)*, 247(3):537–543, 2010.